Master's thesis

NTNU
Norwegian University of Science and Technology
Faculty of Engineering
Department of Civil and Environmental Engineering

Sigrid Helene Strand

ASSESSING THE MEASUREMENT QUALITY OF UAV-BORNE LASER SCANNING IN STEEP AND SNOW-COVERED AREAS

Master's thesis in Engineering & ICT, Geomatics
Supervisor: Prof. Dr. Hongchao Fan
Co-supervisor: Dr. Trond Arve Haakonsen & Helgeir Dahle
June 2023

NTNU
Norwegian University of
Science and Technology

Sigrid Helene Strand

ASSESSING THE MEASUREMENT QUALITY OF UAV-BORNE LASER SCANNING IN STEEP AND SNOW-COVERED AREAS

Master's thesis in Engineering & ICT, Geomatics
Supervisor: Prof. Dr. Hongchao Fan
Co-supervisor: Dr. Trond Arve Haakonsen & Helgeir Dahle
June 2023

Norwegian University of Science and Technology
Faculty of Engineering
Department of Civil and Environmental Engineering

NTNU
Norwegian University of
Science and Technology

Preface

The study represent my Master's Thesis and completion of the Master's degree in *Engineering & ICT* within the field of *Geomatics* at the Norwegian University of Science & Technology (NTNU) in Trondheim. The Thesis is an individual project conducted during the Spring 2023 and accounts for 30 credits.

The Thesis's topic is formed in collaboration with the Norwegian Public Road Administration (NPRA) and the research project for Geo-hazard Survey From Air (GEOSFAIR) funded by NPRA and the Research Council of Norway. The research investigates the use of unmanned aerial systems (UAS) for the purpose of avalanche monitoring and risk of avalanche threatening the Norwegian public roads.

I am grateful for the opportunity to further expand my deep interest in spatial data and remote sensing. My motivations for working on cutting-edge technology within the field of Geomatics flourished through this unique opportunity to support natural demanding challenges we see happening in front of us.

I want to express my greatest appreciation to my supervisors Prof. Dr. Hongchao Fan at NTNU, and Dr. Trond Arve Haakonsen and Halgeir Dahle at NPRA, for making this Thesis possible. Your guidance and competence have enriched me and my work on a academic level to further support research in the field of laser scanning. Furthermore, I want to highlight the support I got to carry out the experiments when I needed it the most.

Additionally, I want to give a special thank to my partner for encouraging and believing in my work throughout this semester. With you, this period of my life have been filled with countless days of joy, inspirations and comfort.

Trondheim, 11th of June 2023

.....

Sigrid Helene Strand

Abstract

Avalanche monitoring in the Norwegian mountains has great potential for preventing catastrophes, such as avalanches affecting public roads, and for informing hikers about dangerous paths. Using an unmanned aerial vehicle (UAV) borne laser scanner to collect point clouds in real-time for snow depth change detection can potentially be used to monitor avalanche risks. The remaining issue is to determine the quality of the point cloud data in steep and snow-covered areas. This thesis suggests a protocol for assessing the quality of the point cloud data and investigates the impact of key flight parameters, speed and altitude above ground level, on measurement accuracy.

Roof models are utilised as control planes to emulate steep areas and for easy extraction of collected point for further error analysis. The real-time positions of the control planes are derived and a plane is constructed to be compared with the collection of points above and below the roof models. The distances of the points to the control planes are used to investigate the median and median absolute deviation. Further, the absolute distance is used to find the arithmetic mean, standard deviation and root mean square error of the distances. Lastly, inliers and plane equations are constructed from the UAV-collected point clouds using random sample consensus (RANSAC) segmentation for comparison with the dimensions of the roof model. The angle, volume and mid-point difference is calculated between the two plane equations from the boundaries of the bounding boxes. These parameters provide key insight into reliability of the point cloud data.

The comparison reveals tangible position data and the impacts of flight speed and altitude on accuracy. Although varied flight speed shows no notable change in the error measures, the amount of points collected is significantly effected by both speed and altitude. Notably, point coverage is concentrated near the top of the roof models. As a result, the model volume calculated from the RANSAC-constructed plane that most closely matches the volume under the roof model is only 50% of the expectation: 0.030 m instead of 0.060 m. The RANSAC-derived plane equations are compared with the roof model planes. The investigations of the inliers shows more points are collected above the roof model planes than under. The standard deviations of the inliers are between 0.011 m and 0.023 m, and the root mean square error is between 0.060 m and 0.019 m. The investigations reveal clear indications of UAVs reliability for monitoring steep and snow-covered areas, without support from reference points to correct the positions.

Sammendrag

Overvåkning av snøskred i de norske fjellene har stort potensial for å forebygge katastrofer, som for eksempel snøskred over offentlige veier, og for å informere skiløpere om farlige løyper. Bruk av en ubemannet flyvende enhet (UAV) med en laserskanner kan samle inn punkter i sanntid. Disse kan brukes for å oppdage endringer i snødybde som potensielt kan brukes til å overvåke snøskredrisiko. Et gjenværende problem er å bestemme kvaliteten til punktskydataene i bratte og snødekte områder. Denne oppgaven foreslår en metode for å vurdere kvaliteten på punktskydataene og undersøker påvirkningen av flyparametere, hastighet og høyde over bakkenivå, på målenøyaktigheten.

Takmodeller brukes som kontrollplan for å etterligne bratte områder og for å enkelt kunne finne ønskede punkter for ytterligere feilanalyse. Sanntidsposisjonene til kontrollplanene er målt og to plan er konstruert for å sammenligne punktene over og under takmodellene. Avstandene fra punktene til kontrollplanene brukes til å undersøke medianen og absolutt avvik i forhold til medianen. Videre brukes den absolutte avstanden til å finne det aritmetiske gjennomsnittet, standardavviket og kvadratisk gjennomsnittlig feil. Til slutt konstrueres planlikninger fra UAV-samlede punkter, som ligger i nærheten av dette planet. Dette gjøres ved hjelp av segmentering med *random sample consensus* (RANSAC) og de konstruerte planene sammenlignes med takmodellene. Vinkelen, volumet og midtpunktforskjellen beregnes mellom de to planlikningene fra grenseverdiene til avgrensningsboksene. Disse parameterne gir nøkkelinnsikt i påliteligheten til punktskydataene.

Sammenligningen avslører håndgripelige posisjonsdata og de påvirkningene varierende flyhastighet og høyde har på nøyaktigheten. Selv om varierende flyhastighet ikke viser noen signifikant endring mellom nøyaktighetsmålingene, påvirkes antall samlede punkter betydelig av både hastighet og høyde. Det er observert at målte punkter er konsentrert nær toppen av takmodellene. Som et resultat av dette er volumet beregnet fra de RANSAC-konstruerte planene, betydelig lavere enn takmodellvolumet. Den konstruerte takmodellen fra RANSAC som samsvarer mest med volumet under takmodellen er bare 50% av forventningen: 0,030 m i stedet for 0,060 m. Undersøkelsene av inneliggende punkter viser at flere punkter samles over takmodellplanene enn under. Standardavviket til inneliggende punkter ligger mellom 0,011 m og 0,023 m, og den kvadratisk gjennomsnittlige feilen mellom 0,060 m og 0,019 m. Undersøkelsene avslører klare indikasjoner på pålitelighet ved bruk av UAV for overvåking av bratte og snødekte områder, uten støtte fra referansepunkter for å korrigere posisjonene.

Contents

List of Figures

List of Tables

Nomenclature

3D Three-dimensional

ALS Airborne Laser Scanning

BBox Bounding Box

C2C Cloud to Cloud

DEM Digital Elevation Model

DoD DEM of Difference

DSM Digital Surface Model

DTM Digital Terrain Model

EUREF89 European Terrestrial Reference System 1989

GEOSFAIR Geohazard Survey from Air

GNSS Global Navigation Satellite Systems

IMU Internal Measuring Unit

LCP LiDAR Control Plane

LiDAR Light Detection and Ranging

MAD Median Absolute Deviation

NDH National Elevation Model

NMA The Norwegian Mapping Authority

NN2000 Normal Null 2000

NPRA The Norwegian Public Road Administration

PPK Post-Processed Kinematics

RANSAC Random Sample Consensus

RGB Red Green Blue

RMS Root Mean Square

RMSE Root Mean Square Error

RTK Real-Time Kinematic

SfM Structure from Motion

SOTA State-of-the-art

TLS Terrestrial Laser Scanner

UAS Unmanned Aerial System

UAV Unmanned Aerial Vehicle

VRS Virtual Reference Station

Chapter 1

Introduction

In this first chapter, the problem and motivation behind the project of quality measurement of steep and snow-covered areas are introduced. The objectives of the thesis are presented and the main approach of solving the problem is illustrated. Further, the outline of the following chapters are described.

1.1 Background

Every year, there are avalanches throughout the Norwegian mountains and the results of these natural disasters can be catastrophic. In these steep areas, it can be extremely dangerous and knowing safe paths is difficult. Being able to monitor areas with a higher risk of avalanche and directly sending risk alerts to humans in the area is greatly beneficial and could prevent missing people and possibly fatalities. By monitoring the change of snow depth and movements in these specific dangerous areas, the risk can be determined in real time and alerts of possible avalanches can be sent directly.

An unmanned aerial vehicle (UAV) can be used for collecting information and data in challenging terrain such as the Norwegian mountains. A commonly used Global Navigation Satellite Systems (GNSS) positioning system for UAVs is real-time kinematic positioning (RTK). RTK enables real-time positioning of a steep area that can directly be used as a real-time monitoring of change. The UAV can be equipped with several sensors, such as Red Green Blue (RGB) cameras and thermal imaging, but for this project a Light Detection and Ranging (LiDAR) sensor mounted on the UAV is used to collect points from the snow surface. The collected point clouds can reveal heights and structures of the surface. By collecting this data in separate time segments the change of snow height and structure may be revealed. Further, the risk of avalanche in the area can be assessed from the results.

The Norwegian Public Road Administration (NPRA) , are monitoring risk of avalanche over

roads. Strynefjellet is a mountain in Norway that has a high risk of avalanche with a possible range affecting Norwegian public roads. It has been heavily monitored during the winter seasons by the NPRA. As part of the project Geohazard survey from air (GEOSFAIR), funded by the NPRA and the Research Council of Norway, the investigation of using unmanned aerial systems (UAS) or drones for the purpose of avalanche monitoring have been tested. By using a laser scanner, data is collected in the form of a point cloud representing the structure of the snow surfaces.

The remaining bottlenecks in using UAV-borne laser scanners for this purpose are protocols for assessing the quality of the data and knowing the possible limitations of use for the purpose of avalanche monitoring. The method for measuring the quality in challenging terrain and steep areas can be complex when a ground control point is needed. Measuring the accuracy of the collected data is extremely important for knowing to what extent you can rely on the results from the data acquisition. Using real-time data as a quick response indicator of snow change can be necessary in emergency and time-dependent scenarios, but using the data without any processing can be dangerous if the quality of the data does not fulfill the quality requirements for such use cases. Therefore, it is important to know the accuracy that can be expected and UAV parameters that can affect the result's quality. Only then would using a UAV with a LiDAR sensor for the purpose of avalanche monitoring would be appropriate.

1.2 Objectives

Based on the motivation and background of this project, the main objectives are formed. The remaining challenges of monitoring the avalanche in the Norwegian mountains with a UAV are not knowing the quality of the collected data and how it is affected by the parameters of speed and altitude above ground level (height) on steep and snowy terrain. The project therefore defines three main research question.

1. How can the quality of the point cloud be assessed for steep areas?
2. Do the UAV parameters of speed and height effect the accuracy?
3. What is the accuracy in steep and snow-covered areas?

When investigating these research questions, the main hypothesis is that UAV-borne LiDAR with RTK GNSS can be used to accurately monitor steep and snow-covered areas. This hypothesis is supported by two complementary sub-hypotheses. One sets the boundaries for applicability of the overarching hypothesis by quantifying the effect of speed and height of a UAV on data acquisition accuracy. It is proposed that increasing speed and height beyond a certain threshold will result in data quality that is no longer suitable for accurate detection of snow-covered slopes. In tandem, it is hypothesised that a reliable protocol for accuracy

assessment can be developed for steep areas. This protocol is expected to reveal quality of point cloud data acquisition and support assessment consistency.

The objectives of this thesis are

1. To develop a reliable protocol for assessing the quality of point clouds for steep areas
2. To quantify the impact of speed and height on the accuracy of point acquisition
3. To determine the feasibility of using the protocol, within boundaries defined by the impact of speed and height, for accurate detection of steep and snow-covered areas

1.3 Approach

The approach is defined by the three main objectives in this thesis. The following approach is needed for developing a relevant method.

- Achieve in-depth knowledge of general quality assessments of UAV and UAV-borne LiDAR for slope and depth detection
- Investigate possible parameters that can affect the collected point cloud and it's accuracy
- Extract valuable takeaways from previous GEOSFAIR work regarding steep areas and snow-coverage impacts

Further, the gained knowledge is used to construct a method for investigating the main objectives.

- Construct a design of experiment for detecting steep areas with a UAV-borne LiDAR
- Develop a method for analysing and comparing the point cloud data from various parameters

Lastly, after the design elements and analysis have been identified and tested, the solutions need to be evaluated with the purpose of accomplishing the main objectives.

- Analyse the chosen design elements of detecting steep areas
- Evaluate the results of the parameters
- Investigate if the method reveals any accuracy concerns as it relates to slopes and snow coverage

1.4 Outline

The remainder of the thesis report is structured into the following chapters: *Theoretical Background & Literature Review*, *Steep Measurement & Design of Experiment*, *Experimental Results & Analysis*, *Discussion* and *Conclusions*. Lastly, the *Appendices* are presented.

In **chapter 2**, the theoretical background and related work for this project are presented. The relevant fundamental principals with the main focus on monitoring via UAV-borne LiDAR are described. Further, the state-of-the-art (SOTA) algorithm Random Sample Consensus (RANSAC) for constructing a plane is defined in this chapter, complimented by the related literature for assessing the quality of UAV-borne LiDAR with RTK GNSS.

In **chapter 3**, the methodology of quality assessment for steep and snow-covered areas is presented. The steep area measuring method with a LiDAR control plane is introduced, followed by the design of the experiment and the data analysis.

In **chapter 4**, the results from the experiments and analysis are presented. First, the experimental parameters and solutions of the initial calculations are given. Then, the experimental results of the point cloud and the error measures are presented, including a visualised analysis of the collected point clouds. Lastly, the estimations of plane fitting with RANSAC inliers and error measures of inliers are presented.

In **chapter 5**, the discussion of the design elements of the experiment, experimental conditions and results are presented. The results are compared to related work and the accuracy investigated for steep and snow-covered areas.

In **chapter 6**, the conclusions of the thesis and summations of the work are presented. Additionally, four recommendations on future work are described.

In the **Bibliography**, all references that are used for this thesis are listed.

In **Appendix A**, the results of the measured positions of control planes are listed.

In **Appendix B**, the baseline calculated points of the position of the control planes are given.

In **Appendix C**, the visualisations of control planes and results of collected point clouds for the experiments are illustrated.

Chapter 2

Theoretical Background & Literature Review

In this chapter, the theoretical background and literature review related to UAV-borne laser scanning approaches and accuracy measurements are presented. The fundamental principals of UAVs for monitoring, laser scanning and general RTK positioning are described.

2.1 Fundamental Principals

2.1.1 Unmanned Aerial Vehicle for Monitoring Nature Hazards

A UAV, also known as a drone, is an important and affordable tool used among rescue teams, mountain search and for assistance in challenging terrain [1]. They allow investigation in absence of a human pilot and are managed by onboard and controller equipment. In some cases the UAVs can be autonomous [2, 3]. UAVs are also commonly used for surveillance and mapping by using GNSS positioning.

The unmanned aircraft is often made from lightweight materials to increase precise maneuverability and positioning. A variety of sensors are used on the UAVs. Sensors, such as, RGB camera, laser scanner or thermal imaging, can be used to collect desirable data from flights [4].

The advantages of the UAVs in the above-mentioned use cases are collection of data in areas with dangerous terrain and difficult access. They can be cost-effective and time-efficient when being used for time critical episodes such as during natural disasters. Research on the accuracy of UAV equipped with LiDAR are showing high quality of data with centimetre accuracy [5]. Another advantage is the flexibility of using a sensor suitable for each purpose of flight.

Some disadvantages of using a UAV are the privacy concerns and issues regarding regulations. Another important factor is ethical usage of a UAV and the responsibility that follows actions to minimize the impact on the society and environment [6].

Before an experiment with a UAV, planning of flight is essential in order to achieve desired results. The important factors in planning the flight include:

- Area of flight
- Number of flight paths & direction
- Signals & targets for data acquisition
- Sensor(s) for data collection
- Weather & terrain conditions

The flight planning stage begins by determining the area of flight. The area can be defined by the landscape or objects for investigation, length and area of coverage. The flying paths and route commonly has an overlap to increase the accuracy of mapping and processing data protocols. The direction of flight can be changing according to the planned flight paths. Target points can be used to specify specific points on ground for further investigation and accuracy processing. The sensor or sensors are chosen for the specific task and desired data. The weather conditions can play an important role on the accuracy of the results and needs to be evaluated before flight. Lastly, the terrain and landscape conditions may affect the chosen flight path and further impact the above-mentioned factors [7, 8].

2.1.2 UAV-Borne Light Detection & Ranging

LiDAR is a remote sensing technique that can be used on a UAV for surveillance and mapping of urban areas, infrastructure and terrain. The technology is based on a laser that illuminate surfaces and uses photodiode to register the backscatter radiation. Typically for a Airborne Laser Scanner (ALS) short laser pulses with the size of 4-10 ns and frequency of 50-200kHz are emitted [9]. The positioning of each light beam and rotation of the sensor are recorded along the UAV flight path typically with a GNSS RTK receiver and an Internal Measuring Unit (IMU) [10]. The sensors' position, orientation, beam deflection and range are converted into a three-dimensional (3D) point cloud. The points in the point cloud represent the laser pulses reflected from the surface [9].

The accuracy of LiDAR varies based on different sensors and UAV models. Depending on the usage of the point cloud after scanning, a ground-based LiDAR, also called a Terrestrial Laser Scanner (TLS) can be used and receive a higher accuracy than a UAV-borne LiDAR. A TLS has a high expected accuracy, and can deliver data on millimetre-level scanning. However; the TLS lacks in efficiency compared to the UAV-borne LiDAR which can process more data in

less time and access difficult terrain. The accuracy expected when processing the point cloud data is +/- 5 cm, which in many use cases can be tolerated. The LiDAR sensor Zenmuse L1 is a sensor from DJI. It is capable of delivering a survey-grade accuracy of 5 cm and an absolute accuracy of 10 cm from the altitude of 50 m according to the DJI specifications. It supports three returns per laser shot and has a 3-axis stabilised gimbal [11, 12].

The ranging accuracy is an important parameter for defining how close the measured distance between the UAV and the target point is to the actual distance [13]. The system accuracy is another key parameter which can be used to assess the quality of the measurement. The accuracy of the scanning target can be described by the error of the 3D position, the displacement error and the error of the rotational angle of the scanning targets [12].

A commonly used alternative to LiDAR technology is photogrammetry. While photogrammetry technology is based on imaging techniques and data captured by RGB cameras, the LiDAR technology enables measurements of detecting structure of landscapes. The LiDAR can be used to capture the shape of the underlying terrain through vegetation [14, 15]. The sensor is also not dependent on daylight because it uses emitted light and can work in all lighting conditions.

2.1.3 Point Cloud Data

Point cloud data is a widely used data format for 3D visualisation. Each point has an X-, Y- and Z-coordinate in 3D space and the points usually belongs to a larger dataset of points. [16]. A point cloud can be produced as output from a laser scanner and represent an exact 3D replica of the scanned environment. In addition to the coordinates of each point in the point cloud, colour values can be collected with most laser scanners, where colour information of an object are given each point. Another attribute collected is intensity which represents the amount of light energy reflected from an object during measurement. The reflected light energy can be used to create a colour representation in the point cloud data where darker colours represent the return of less light energy and the lighter colours have returned more light energy [17–19]. The reflectivity of the target surface is collected and represented as reflectance values in the point cloud. The scale is given by the reflected laser power to the incoming laser power related to the physical properties of the surface measured. In other words, the reflectivity is related to the properties of the surface and the light an object reflects determined by the colour, texture and roughness [20, 21].

When a UAV-borne LiDAR measuring sensor is chosen for a specific surface for detection, a suitable value for the point density should be considered. The point density is defined as points per unit squared area, where the standard unit is points per metres squared (pts/m^2). The density is an important factor to consider when measuring an object that requires a certain amount of point coverage. The speed and altitude of a UAV-borne LiDAR can affect

the amount of points on one specific object and therefore also needs to be considered [22, 23]. Each UAV-borne LiDAR sensor is also specified by the parameter of number of points per second (pts/s) captured. The LiDAR sensor Zenmuse L1 have a point rate of 240,000 pts/s on single return and 480,000 pts/s on multiple return [24]. This parameter is also important for determining the level of detail in a captured area [25].

Point cloud data can be used for several purposes such as monitoring and detecting changes that can cause a nature hazard, plant growth tracking or other environmental changes [26–29]. The general approach of using point cloud data for the aforementioned purposes consists of five steps. The first step is to collect the point cloud data with a LiDAR sensor. Then, the data is pre-processed where approaches such as noise filtering and removal of outlier techniques are important. These techniques can typically be filtering, segmentation or registration. The third step is to extract and collect the data that are relevant for the purpose of the monitoring. Next step is to use a model for classifying points into the specific monitoring topics and lastly use the model for a real time detection for new data. Achieving highly accurate results for the aforementioned purposes is dependent on the accuracy of the point cloud data collected [30].

2.1.4 Real-Time Kinematics Positioning

RTK is a relative positioning technique that employs two or more receivers constantly tracking the satellites. This type of method is beneficial for methods that require positions in real-time, have an unobstructed line of sight and the desired measuring area involves a larger amount of unknown points. The system consists of a base station, RTK rover and satellites. The base station's measurements and coordinates are transmitted and communicated to the rover. The rover combines the transmitted data and process the GNSS measurements collected at the base station and the rover receiver. The rover's coordinates are returned in a given reference system.

For this positioning technique, there is no post-processing required and the position accuracy of the method given in Root Mean Square (RMS) is in the general order of 2 cm to 5 cm. The results can be improved by staying the same position of a measurement for about 30 seconds. Other possible errors can be caused by the delay or latency of the communication between the receiver and base. This communication latency can be caused by the tasks of formatting, packetising, transmitting and decoding the data in the base station [31]. A variant of RTK is a network-RTK where the correction data comes from a virtual reference station (VRS) . The correction data is calculated from a network of known stations and transmitted to the satellite receiver from a central control station. Both private companies and the Norwegian Mapping Aunthority (NMA) offer real-time services based on network-RTK [32, 33].

Requirements of real-time measurement based on the Norwegian standards:

1. At least one control point (known point) within a satisfactory quality needs to be registered before and after measurements

2. During measurements known points should be visited. If there are no other points available nearby, is it possible to control previous documented objects of good quality and that has a solid defined structure. The deviations needs to be documented

3. When changing a reference system, at least one defined object from previous surveying needs to be measured again for a control. The deviations need to be documented

RTK Positioning on UAV

GNSS RTK is a preferred positioning technology for UAVs. The combination is a feasible and appropriately accurate solution for various mapping projects where the real-time location is known during the flight. A post-processed kinematics (PPK) method records raw GNSS data during flight and subsequently post-processes the differential correction data from the VRS data. This method is an alternative to the RTK method and is an important method when real-time corrections are not available. This method can give more flexibility on area of flight for surveying [33, 34].

Parameters Impacting Accuracy

The quality of the measurements is dependent on atmospheric and local conditions. The accuracy assessment also needs to consider the quality and setup for the equipment used. NMA provides a checklist of conditions that can improve the setup for the RTK rover antenna to receive satellite signals [35]:

- Investigate conditions causing the satellites signals to be reflected before they reach the antenna

- Check the GNSS receiver's ability to eliminate reflected signals

- The atmospheric interference with the system can impact the accuracy. For example, ionospheric activity could be one parameter for inaccuracy

- The geometry and position of satellites can impact the results from the receiver. The availability of satellites is also an important factor

- Check the GNSS receiver's ability to calculate positions

2.2 RANSAC Method for Plane Fitting

RANSAC is a iterative method used for estimating a mathematical model from data sets containing outliers. The method is used to identify outliers and inliers. It can also estimate a best fitted plane model with the identified inliers. Algorithms for line modelling from point cloud data have been studied by researchers for several years [36–38]. Among these, the RANSAC algorithm has shown many advantages such as simple application and low computation.

The SOTA RANSAC algorithms are operating in a hypothesize-and-verify framework. This approach involves randomly selecting a minimal subset of the point cloud data and estimating model parameters from the chosen subset. The model is compared against the complete point cloud dataset and the consistency of the points with the estimated plane fitted model is derived. The framework is repeated until it is a lower probability of finding a better model based on a predefined threshold (often between 1% and 5%) [39]. The general steps of a RANSAC algorithm for finding a plane based on a point cloud is illustrated in Figure 2.1.

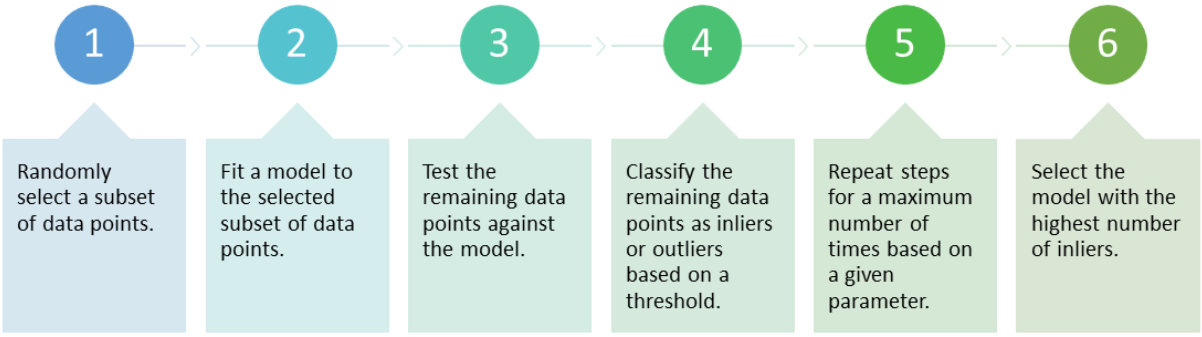

Figure 2.1: The steps of RANSAC algorithm for plane fitting

There are several ways to implement RANSAC in Python. The libraries pandas, matplotlib, random, math, pyransac3d and open3d can be used for implementation based on point cloud data [40, 41]. The libraries also identify a bounding box (BBox) consisting of the inliers [42]. The BBox makes it possible to investigate the size and centre of the inliers from the RANSAC algorithm that can be used in further analysis [43].

2.3 Assessing Quality of UAV With RTK & LiDAR

In this section related work regarding quality assessments of UAVs is presented.

2.3.1 LiDAR Control Plane

For studies on UAV LiDAR, a LiDAR Control Plane (LCP) can be used to identify points in the point cloud. The LCPs are shaped as a roof model with two roof-like oriented surfaces. The inclination is 45°, where the vertical and horizontal components can be analysed for accuracy assessment. They can be placed on a tripod or other objects on ground during flights. After the flight, the points collected on the LCP are recognizable in the point cloud data [44].

Accuracy Investigation With LCP

An accuracy investigation of UAV LiDAR georeferencing by using LCPs is conducted by [44] for the purpose of collecting a point cloud with millimetre accuracy. The UAV flights are conducted at a speed of 4 m/s with an altitude of 53 m above ground level. These parameters give a pulse density of 300 to 400 points per m^2. The LCPs are 40 cm × 80 cm with an inclination of 45°. The accuracy values from the point to plane calculated in this project is based on the point cloud data collected on five LCPs. The measurements consist of:

- Arithmetic mean
- Standard deviation
- Median
- Median Absolute Deviation
- Root Mean Square Error (RMSE)

The results are compared to accuracy measurements calculated via photogrammetry. The small amount of signalized points on the LCP result difficulties of validation of the accuracy. However, the results combined with the photogrammetric method produce promising results. The accuracy of the LiDAR point cloud without the combination of the photogrammetric method gives the results of maximum distance from point to plane of 4.70 cm and minimum distance of -2.80 cm. The arithmetic mean of the distances is 3.40 cm and the median 1.05 cm. The standard deviation of the distances gives the result 3.42 cm and the Median Absolute Deviation (MAD) results is 4.97 cm. The result of the RMSE is 3.56 cm [44].

2.3.2 Height & Speed Parameters

When assessing quality of UAV flight, various parameters can have a potential impact on the accuracy. The number of points collected per square metre from a UAV LiDAR is effected by the speed and height as described in subsection 2.1.3.

Based on an assessment of the steering precision of a UAV with an RTK receiver with a photogrammetric application, the study by [45] investigates how speed effects the cross track

error. The method of the study consists of speeds of 10 km/h, 20 km/h and 30 km/h under good meteorological conditions. The error is measured as the distance between the UAV's position and the flight profile. This is calculated transversely to the course and is adopted as the accuracy measure of the steering of the UAV along a flight profile. The results of the study show that the flight speed does not effect the accuracy measure of a UAV with a photogrammetric application [45]. However, the speed effect on the UAV LiDAR is not studied.

2.3.3 Detection of Slope & Depth

There have been several studies on detecting landslide movements or snow depth with UAV-borne LiDAR data. One study from Southern Italy by [46] uses UAV and LiDAR technology for monitoring landslide movements in high risk and large rain-triggered areas. Pre- and post-event LiDAR and UAV Digital Elevation Models (DEM) together with UAV mosaics are used to categorize the the morphological features, measure the horizontal displacement and detect the elevation change between the different landslide bodies. The use of LiDAR Digital Terrain Models (DTM) and UAV-derived digital surface models (DSMs) combined with LiDAR and field-based data acquisitions shows a high effectiveness for evaluating the the landslide bodies [46].

Detection of snow depth in the Swiss Alps based on UAV-borne LiDAR is studied by [47]. Different LiDAR workflows are analysed and compared, and snow depth algorithms are used on point and grid level. The methods used are DEM of Difference (DoD) which subtracts two DEMs to create a new one (snow-on and snow-off) and Cloud to Cloud (C2C) distance algorithm that finds the difference between the snow-on and snow-off classified points. The results of the mapping proves the UAV-LiDAR possibility to be used for snow mapping in both flat and steep forests. Although, the steep forest gives more challenges in the 3D registration, ground classification and the point-to-point snow depth calculations. The RMSE between the snow probe and the LiDAR-derived snow depth is calculated in 74 locations. The results of this calculation in five transects is between 5-19 cm in all methods. The results of the absolute and relative snow depth values validated from the LiDAR-derived snow depth grids and in-situ measured snow show an RMSE of 4-16 cm in the steep areas. This is the result before an offset is implemented to reduce the RMSE. The methods works efficiently, but struggles with the lower point density areas in the steep forest [47].

The NPRA have evaluated the usability of LiDAR sensors on a UAV/UAS for avalanche monitoring. The study analyzes the accuracy and usability for avalanche hazard assessment by collecting data from seven vendor's flights with UAV-borne LiDAR sensors. The data acquisition is carried out at Trollstigen in Norway and slopes are investigated. The results of the point cloud data coverage compared to the National Elevation Model (NDH) , shows a significant variance amongst the seven vendor tests. Only one of the vendors is able to achieve good agreement with the NDH line. The test shows that the point clouds seem to be usable

reproducing geometry on metre- to centimetre-level, but the point densities and point precision are insufficient for evaluation regarding rock mass quality. The point cloud accuracy is compared to the point cloud from the NDH from NMA. The NDH has a lack of coverage in the steepest part of the wall, but the comparison is based on an absolute accuracy of each cloud. The C2C distance is calculated between the seven point clouds and the results from three of the vendors show points collected above the NDH point cloud. The results from these three vendors aligned the most. In summary, the study concludes that the level of precision and accuracy is good enough to be used for monitoring snow pack and avalanche risk. The RMSE is below 10 cm and the LiDAR data can be used to detect snow depth and volume, but the signs of systematic errors indicate room for improvement. The data acquisition can be improved by carefully collecting the positioning of ground control points and choosing a point density suitable for the study [48].

Further studies from the NPRA and SINTEF in the research group GEOSFAIR shows a test by SINTEF with UAV-borne LiDAR (DJI M300 Zenmuse L1) investigating various flight speeds to detect the morphology along the steeper slopes ($20-22°$). The altitude of the flight perpendicular to the slope is at the lowest 1.5 m and highest 4,5 m and the flight speed is between 1-0.5 m/s. The results give accurate snow height and information about the terrain. The conclusion is that a flight altitude of 2 m and 3 m is the most suitable parameters. The NPRA did a similar test with the same model of UAV-borne LiDAR, but with the flight speed 7 m/s and 60 m altitude above ground level. The result of the data acquisition show points collected above the actual snow surface. These are considered as noise from reflections from air-suspended snowflakes. The RMSE calculated from two separate study areas divided in seven flights show variation between 0.052 m and 0.155 m. The arithmetic mean error varies for the same flights between 0.154 and 0.047 [49].

2.3.4 Method of Quality Assessments of UAV

Assessing UAV-borne LiDAR Precision

A method for testing the precision of the affordable UAV-borne LiDAR DJI Zenmuse L1 Scanner mounted on a DJI Matrice 300 UAV is investigated by [10]. The test uses georeferenced targets covered with high-reflectivity foil to easily extract the points from the point cloud. The centre is determined for the calculation of systematic shift of the point cloud. The shift is corrected and compared with a dense Structure from Motion (SfM) point cloud. The results show 3.5 cm accuracy in all directions after the removal of georeferencing error which is better than the manufacturer-declared values of 10/5 cm horizontal/vertical. The RMSE of the original cloud compared to checkpoints without transformations is 0.036 m, 0.025 m and 0.029 m in all direction of the three flights (two with 50 m altitude and one with 70 m, respectively). The study also concludes with the evaluation of the colour information containing a relatively high systematic shift of approximately 0.2m [10].

Assessing Accuracy of RTK on UAV

In the study by [50], the position accuracy of RTK GNSS on a DJI Matrice 600 Pro is investigated. The manufacture-declared positional accuracy of the UAV is 2 to 3 cm, but actual accuracy of the drone RTK for positioning images and usability for the purpose of mapping without the additional ground control points is being investigated. The RTK positioning data is used to directly georeference and evaluate the data. The altitude of the UAV is 40 m above ground and is evaluated against ground control points. The planemetric accuracy of the direct georeferencing of the photogrammetric product ranged between 30 cm and 60 cm. The result of the analysis show a time delay of up to 0.28 seconds at a speed of 4 m/s from the UAV RTK and until the camera mounted on the UAV acquires an image. The results of this time delay is affecting the direct georeferencing accuracy by an offset value of 1.12 m. After series of flight experiments, the time delays decreases with time delay adjustments and a decimetre accuracy is obtained with the method [50].

Chapter 3

Steep Measurement & Design of Experiment

In this section the methodology of assessing the quality of steep and snow-covered areas by using a UAV-borne LiDAR sensor is described and the purpose of using roof models as signals is explained.

The methodology consist of the following parts:

- The steep measurement method
- The design of experiment
- The data analysis

3.1 Steep Measurement

The task of this project is to investigate the accuracy of using an UAV-borne LiDAR in steep and snow-covered areas. To be able to detect the quality of the point cloud collected from a UAV-borne LiDAR, signals can be used to emulate a steep area. By using a roof model as LCPs, with an angle simulating a slope, points can be collected on each side of the roof. This enables the possibility to measure quality of the point clouds and is additionally highly visible in the point cloud for extraction.

Five LCPs are constructed with the same dimensions. Their position is measured with a RTK GNSS receiver. The points collected on each LCP can be compared to each other. The accuracy of point clouds collected on the roof slopes can be used to identify the accuracy in steep areas.

3.2 Design of Experiment

The design of the experiment based on using LCPs as signals is outlined below. Important design factors described are the flight parameters, area of flight, flight path, chosen signals, post quality check, weather and terrain conditions.

3.2.1 Flight Parameters

The flight parameters, speed and height, can be used in the UAV flight experiment to investigate how the quality of the data acquisition is affected. When flying over steep and snow terrain, these parameters may vary, therefore the impact on quality must be assessed.

The experiment is conducted in several sessions consisting of various flight speed and altitude conditions. All sessions follow the same flight path. The flight speeds are 3 m/s, 5 m/s, 8 m/s and 10 m/s. The altitudes are 40 m and 80 m above ground level. The first session is repeated with the same conditions in the last session to control for external changes in the experiment. This is shown in Table 3.1. These flight sessions are established based on the investigation of the impact of speed and height on the accuracy of point acquisition in subsection 2.3.2.

Table 3.1: Sessions of UAV flight in experiment

Session	S1	S2	S3	S4	S5	S6	S7	S8	S9
Speed [m/s]	5	3	8	3	8	5	10	10	5
Altitude [m]	40	40	40	80	80	80	80	40	40

3.2.2 Area of Flight

The place chosen for flight needs to be accessible by car and close to a known point in the Norwegian trigonometric network. For the sake of safety and uninterrupted sessions, the place also needs to be at an unused field or similar area. Places like public parks, pedestrian walk paths and such are not suitable places for the experiment. Using an area where NTNU is the landowner is a great advantage to the authorisation of the flight. The area of flight needs to have a suitable size for the wanted coverage of path.

3.2.3 Flight Path

The UAV flight patterns need to be planned before the experiment. The UAV also needs to be calibrated before and after each session. An example of a flight path is shown without any overlaps and on a straight line only in Figure 3.1.

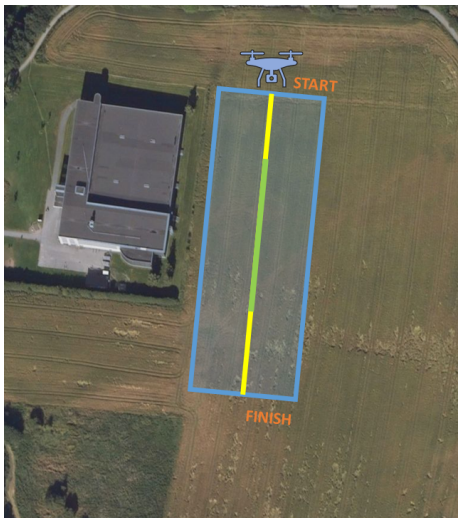

Figure 3.1: Visualisation of flight path for calibration and further experiments

Depending on the experiment and variables of interest, the flight path can be customised. However, it should be noted that increased directional changes and overlaps significantly increase the complexity of the quality assessment.

3.2.4 Principals of Arrangement of Roof Models

The first part of the experiment is to assess field and environmental conditions. If the conditions are as expected tripods can placed out at the chosen place of experiment. It is important to place them deep enough into the snow to prevent them from moving during the experiment. The movement can be caused by the snow melting or wind. Four tripods are arranged as seen in Figure 3.2 and the fifth is placed in the direct centre. All of the tripods needs to be levelled.

After measuring the positions of tripods for each roof model with a RTK GNSS rover, roof models are attached to the tripods. The design of an arrangement of the LCPs is illustrated in Figure 3.2. Roof models are aligned in pairs, with the pairs being parallel to each other. From a bird's eye view a direct baseline is given between the roof ridges, such that LCP 1 and LCP 2 are aligned and LCP 3 and LCP 4 are aligned. The fifth roof ridge is directed at a 45° angle towards the middle of the third roof ridge. Different arrangements can be selected. However, this arrangement is used to define the experimental approach in this chapter going forward.

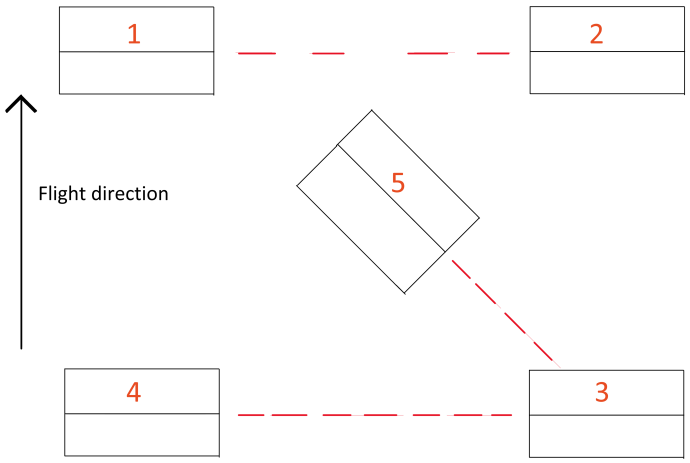

Figure 3.2: Arrangement of roof models where the four first roof ridges are directed the same way and the fifth is directed with a 45° angle towards the middle of roof model three

3.2.5 Post Quality Check

After all flight sessions are complete, the roof model' positions needs to be checked for inaccuracies. The LCPs are dismounted from the tripods and an RTK rover is placed on top. The positions are measured two more times in each tripod to reveal any changes during the experiment. The last part of the experiment is to measure a control point. This is done to evaluate and investigate the accuracy of the RTK rover used to retrieve the positions of the LCPs, as mentioned in point two for requirements of real-time measurement based on the Norwegian standards in subsection 2.1.4.

3.2.6 Weather & Terrain Conditions

It is beneficial if the flight and position experiments are carried out during daylight in a single day to enable comparison of sessions under similar environmental conditions. The chosen area for the experiment needs to be covered with snow for better comparison with a snow surface area in the Norwegian mountains. Because the comparison between the parameters, speed and height needs to be evaluated with the same condition, it cannot be actively snowing for first part of the sessions. Temperature below zero degrees and low illumination is preferable to decrease the chance of signals movement when they are placed on top of snow via tripods. The terrain should be as neutral as possible to minimize its impact on results and the chosen area should not be conducted in the Norwegian mountains. This is to enable a quality assessment with known ground control points in areas without any safety risks for the experimenters.

3.3 Data Analysis

The analysis of the data collected from the experiment is divided into two separate methods, position of LCP form RTK GNSS and point cloud from UAV. The positions collected from the LCPs are validated and used to calculate the true points and true plane equation that is compared to the point clouds collected from the UAV flights with the LiDAR sensor. The analysis of the point clouds needs to be visually validated and extracted from each LCP. Further, measurements of the extracted points in left and right are calculated and compared to the RANSAC estimated inliers. The same error measurements are done for the inliers and a RANSAC plane equation is constructed and compared to the parameters of the true plane equation. The workflow for the respective methods of the data analyses is given in Figure 3.3.

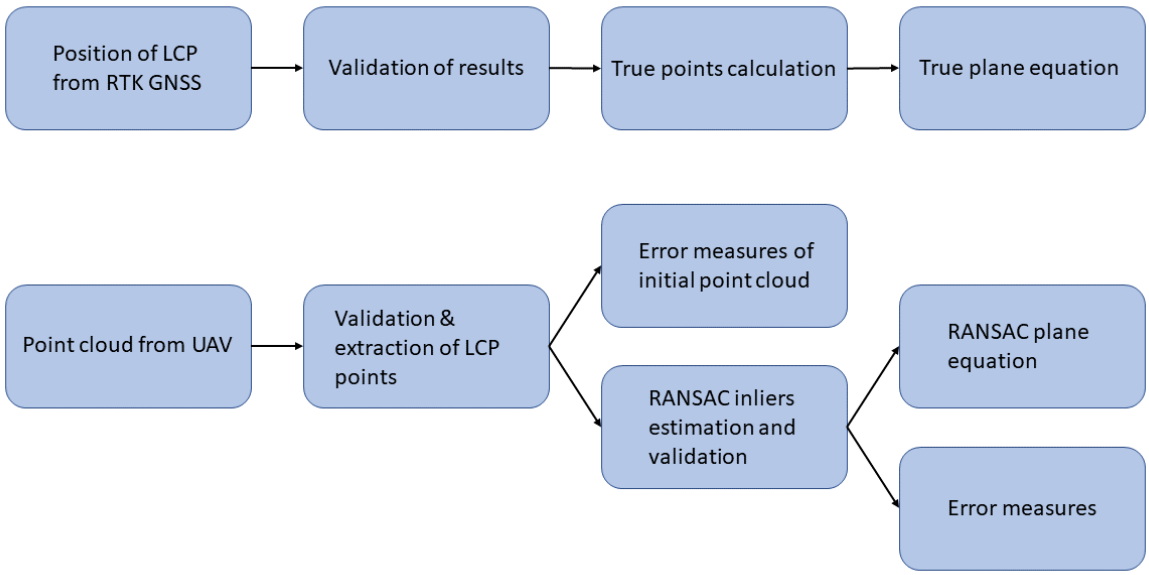

Figure 3.3: The workflow of the designed data analysis of the collected points from the data acquisition

3.3.1 Positions of LCPs

Each position of the LCPs is calculated by the RTK rover during the experiment (before and after the flight sessions). They are calculated four times before and two times after the flights. The results' accuracy is calculated and investigated before being used as true points.

Each point defining the boundaries of the roof models and mid points are given Figure 3.4. The points are named as shown in Figure 3.4 accordingly to the direction of the baseline in Figure 3.2. These name conventions are kept for the calculations of all LCPs with respective number of LCP as first number.

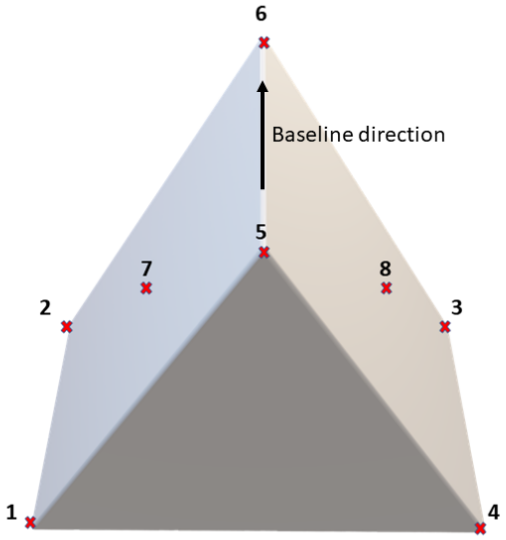

Figure 3.4: True points relatively to the baseline direction

The following procedure is done to find the points measured with the RTK GNSS rover and true points of the roof model.

1. Position of the top is found by adding the distance from the tripod, given in the RTK GNSS rover file, to the to of the roof model
2. Orthogonal measurements are done to derive true points by using the results from the tripod position measurement
3. The abscissa and ordinate is calculated for each points
4. The height difference of the top point on roof model and height of the points in each bottom corner is subtracted from the height of the top point of the roof model. Then the heights of point 1,2,3 and 4 are found
5. The same is done for the middle points 7 and 8, but with half the distance

3.3.2 Construction of True Plane

When constructing a true plane based on the points collected from a RTK GNSS rover that will be compared to the point cloud, the plane equation is found.

1. The point number 1 (p1), point number 2 (p2) and point number 6 (p6) for all five LCPs are imported
2. Two vectors from p1, p2 and p6 are created
3. The cross product between the two vectors are calculated to find the normal vector

from the equation $v \times w = (v_2 w_3 - v_3 w_2, v_3 w_1 - v_1 w_3, v_1 w_2 - v_2 w_1)$, where v is the vector $v = (v_1, v_2, v_3)$ and vector $w = (w_1, w_2, w_3)$ is given in $\mathbb{R}^3$. This gives the parameters [a,b,c]

4. The last parameter of the equation is found via the dot product of the normal vector and p6 from the equation $v \cdot w = v_1 w_1 + v_2 w_2 + v_3 w_3$, where v is the vector $v = (v_1, v_2, v_3)$ and vector $w = (w_1, w_2, w_3)$ is given in $\mathbb{R}^3$
5. The coefficients *a, b, c,* and constant *d* is found for the plane equation on the left side from equation $ax + by + cz + d = 0$
6. The same procedure is done with point number 3 (p3) and point number 4 (p4) to find the right side plane equation

3.3.3 Error Measures of Point Cloud Compared With True Plane

When describing the accuracy of the position of the LiDAR points in the point cloud, the perpendicular distance to the true plane is calculated. Each point in the point cloud divided into left and right sections for calculation of the left and right plane equation. The points are further divided in points above with a positive distance and below the plane with a negative distance. The formula for calculating the perpendicular distance is given by the equation $D = \frac{|ax_0 + by_0 + cz_0 + d|}{\sqrt{a^2 + b^2 + c^2}}$, where Q is a point (x_0, y_0, x_0) and the plane P is given on the form of a plane equation $ax + by + cz + d = 0$ that Q is not on [51]. The following error measures are calculated from the perpendicular distances:

- The minimum distance given by the greatest perpendicular distance to a point below the true plane
- The maximum distance given by the greatest perpendicular distance to a point above the true plane
- The median of the distances above and below the true plane
- The MAD of the distances above and below the true plane
- Arithmetic mean of the absolute distances to the true plane
- Standard deviation of the absolute distances to the true plane
- RMSE of the absolute distances to the true plane

The minimum distance is found from the greatest distance measured below the plane and indicates how far the points are collected below the true plane. Further, the maximum distance, which is the greatest distance measured above the plane, is used to investigate how high above the LCP the points are collected. The median is found from the middle value of the distances in ascending or descending order and the MAD ($\tilde{x}$) is calculated from $\frac{\sum_{i=1}^{n} |x_i - \tilde{x}|}{n}$.

The results from the median calculations are used to determine where the overweight of points are located and the MAD is used to investigate how spread the points are from the median.

The arithmetic mean, standard deviation and the RMSE are calculated from the absolute perpendicular distances to the roof models. The results of the mean can be used to investigate the central tendency from the average of the distances of the points. The standard deviation is calculated to measure the dispersion of the distances of the points and show how distributed the values in relation to the mean value. The RMSE, which is the standard deviation of the residuals, is used to better understand how spread the residuals are.

3.3.4 RANSAC Algorithm on Point Cloud

The RANSAC algorithm is used to find inliers on each side of the LCPs. RANSAC inlier estimation enables the calculation of errors not just by using points, but also using an estimated plane equation based on the inliers to compare with the true plane. The total amount of inliers from point clouds on each LCP for each session are evaluated for further use in error measurements. The distribution of the chosen inliers above and below each plane is found. A new plane equation based on the inliers is constructed. The equation gives the coefficients a, b, c and the constant d. They are compared with the true plane equation parameters. The plane's boundaries are calculated from the minimal BBox of the inliers and the projection of the points on the plane. The planes together with the inliers are visualised in a plot.

3.3.5 Error Measures Inliers & RANSAC Plane

The last part of the error calculations is with the RANSAC plane and inliers in the following order:

1. The minimum and maximum perpendicular distances below and above the planes
2. The mean and MAD of the perpendicular distances
3. Calculations of arithmetic mean, standard deviation and RMSE of the absolute perpendicular distance to the RANSAC planes
4. The angle between the RANSAC plane equations and the difference between the true plane angle
5. The mid-point of the inliers are found and compared to the true plane middle points (p7 and p8)
6. The volume of the RANSAC roof models are found and compared with the true volume of the roof models

The inliers found by the RANSAC algorithm are used for the same calculation as the original point cloud done in subsection 3.3.3 for the first three given in the list above. The results are compared with each other to prove insight on accuracy. Further, angle between the RANSAC planes are compared with the true plane angle. Next, the mid-point of the inliers is calculated. This is found from the boundaries of the minimum BBox. The mid-points are then compared with the mid-points of the true plane, point number 7 (p7) and point number 8 (p8). The last part of the calculations for the analysis involves calculation and comparison of the volume of the LCPs with the volume of the RANSAC planes. The volume is found by using the boundaries of the minimal BBox and their respective projected points in the plane. The points from the upper boundaries with the same height at the lower boundaries are used to create a oblique triangular frustum, which is an irregular representation of the regular triangular prism shapes of the LCPs. The volume is calculated from the convex hull of the shape formed by the boundaries.

Chapter 4

Experimental Results & Analysis

In this chapter the results from the experimental analysis are presented. The chapter is divided in three sections presenting the experimental parameters and results of the true point calculation, the point cloud data analysis and the results of RANSAC estimations on the point cloud data, respectively.

4.1 Experimental Parameters & True Points Results

On the 24th of May, the experiments took place at Dragvoll Idretssenter in Trondheim Norway. The conditions of the experiments during this day are presented in this section. Further, the results from the snow depth measurement and positions from the Leica GS16 rover resulting in a true plane equation are presented.

4.1.1 Equipment & Experimental Conditions

The equipment being used for the experiment is a DJI Matrice 300 UAV with RTK receiver. The RTK is connected to CPOS provided by NMA. The chosen laser scanner is a Zenmuse L1 with the respective specifications in Table 4.1 [24]. The Leica GS16 RTK rover is being used to collect known points from tripods on the field for the comparison. The rover's specifications are listed in Table 4.2 [52].

Table 4.1: Manufacture-declared specifications of DJI Zenmuse L1

Dimensions	$152 \times 110 \times 169mm$
Weight	$930 \pm 10g$
Supported Aircraft	Matrice 300 RTK
Operating Temperature	$-20°$ to $50°C$
Point Rate	Single return: max. $240,000pts/s$ Multiple return: max. $480,000pts/s$
System Accuracy ($RMS1\sigma$)	Horizontal: $10cm@50m$ Vertical: $5cm@50m$
Real-time Point Cloud colouring Modes	Reflectivity, Height, Distance, RGB
Ranging Accuracy ($RMS1\sigma$)	$3cm@100m$
Maximum Returns Supported	3
Supported Software	DJI Terra
Data Format	PNTS/LAS/PLY/PCD/S3MB

Table 4.2: Manufacture-declared specifications of Leica Viva GS16 GNSS rover

Dimensions	$190mm \times 90mm$
Weight	$0.93kg$
Operating Temperature	$-40°$ to $65°C$
Accuracy on Single Baseline RTK	Horizontal: $8mm + 1ppm$ Vertical: $15mm + 1ppm$
Accuracy Post Processing Static long	Horizontal: $3mm + 0.1ppm$ Vertical: $3.5mm + 0.4ppm$
Accuracy Post Processing Static rapid	Horizontal: $3mm + 0.5ppm$ Vertical: $5mm + 0.5ppm$
Supported Software	Lieca Captivate
Supported GNSS Systems	GPS, GLONASS, Galileo, BeiDou, QZSS

The flight sessions and position measuring process are carried out during daylight in one day to ensure the same condition for all sessions. The chosen area for the experiment was covered with snow.

4.1.2 LiDAR Control Planes

Each roof side has the dimensions of 40 cm and 80 cm and the angle between them is 90°. This gives them a slope of 45°, base area of 0.45 m^2 and volume of 0.06 m^3. In Figure 4.1 the dimensions of the roof model are illustrated.

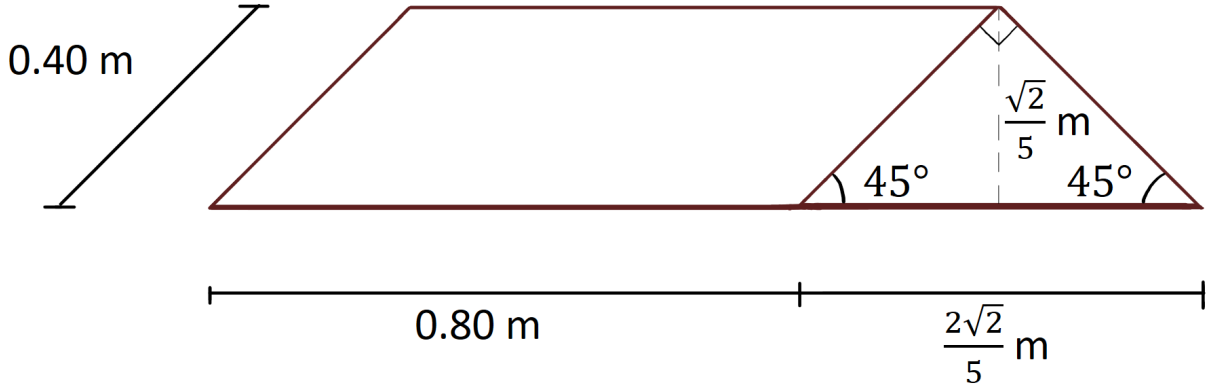

Figure 4.1: Dimensions of the five roof models used in the experiment

The material used for the LCPs are wood and aluminum. Water resistant wood sheets are on the surface for detection and general pieces of lumber for stability underneath. With this construction, the risk of structural damage to the roof models due to moisture or transport is significantly decreased. The roof models are attached to the tripods with a screw to ensure the same position for each of them throughout all of the sessions. In Figure 4.2 the aluminum attachment for the screw is shown.

Figure 4.2: Roof model construction used as signals for point cloud collection with an aluminum screw attachment for stability during flight

4.1.3 Flight Execution

The area chosen for the experiments is behind NTNU Dragvoll Idrettssenter shown in Figure 4.3. A suitable area of around 10 000 m^2, indicated by the black perimeter, is where the UAV flight is planned. The red area is the base for all equipment with easy access to the parking lot with the coordinates in European Terrestrial Reference System 1989 (Euref89) UTM32 7031707N 573696E.

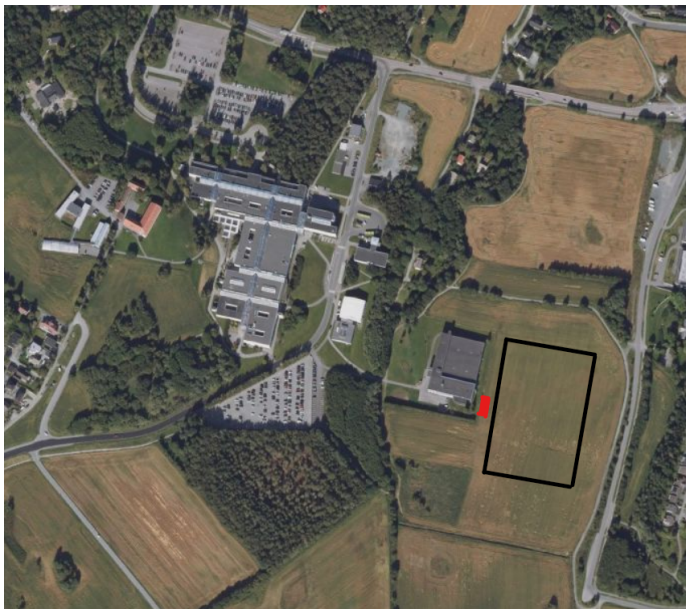

Figure 4.3: Field chosen for experimental testing with an area of around 10 000m^2 given in black and base station for equipment in red

The experimental UAV that can be seen in Figure 4.4. The results are seen in the data processing computer in the DJI Terra data program. The program provides feedback for possible errors that might have occurred during the calibration or flight session.

Figure 4.4: The UAV DJI Matrice 300 before first flight

The expected point densities of the sessions are given in the DJI Terra program and are listed in Table 4.3. The second session has the highest amount of expected points with a value of

531 per LCP. S6 and S8 expect the same amount of point. S5 is expecting 100 points per LCP and is the lowest amount of all sessions.

Table 4.3: Expected collected point density in each session of flight with the UAV

Session	S1	S2	S3	S4	S5	S6	S7	S8	S9
Speed $[m/s]$	5	3	8	3	8	5	10	10	5
Altitude $[m]$	40	40	40	80	80	80	80	40	40
Expected Point Density $[pts/m^2]$	707	1179	442	589	221	354	177	354	707
Expected Points (LCP) $[pts/LCP]$	318	531	199	265	100	159	80	159	318

4.1.4 Irregular behaviour of UAV

The UAV is observed to shift towards north after each session. The landing spot is listed with the same coordinates each flight, but tracks in the snow shows the UAV changing landing spot in Figure 4.5.

Figure 4.5: The UAV DJI Matrice 300 leaving marks in the snow showing indicating change of landing position between each session

4.1.5 Measured Height of Tripods & Snow Depth

The results of measured height of tripods and snow depth is shown in Table 4.4. The snow depth measured is calculated from the lowest surface point near the tripod. The measured height of the tripod is calculated from the snow surface (solid and wet). The greatest snow height is measured in LCP 4 and the lowest in LCP 2 varying from 30 cm to 25 cm. The

greatest height of tripod until snow surface is 97.2 cm in LCP 3 and the lowest in LCP 4 of 82.0 cm. The height of the tripod until through wet snow is increasing the height of tripod between 8.9 cm and 0.7 cm.

Table 4.4: Measured heights in [cm] of each tripod before flight

Number	LCP 1	LCP 2	LCP 3	LCP 4	LCP 5
Snow height [cm]	28	25	27	30	29
Height of tripod until snow [cm]	93.2	83.3	97.2	82.0	93.4
Height of tripod until through wet snow [cm]	97.1	91.2	97.9	87.3	98.1

4.1.6 Positions of True Points

The height of the RTK antenna on the Leica GS16 RTK rover is 19.3 cm. The length between the instrument and the tripod is measured as shown in Figure 4.6. This difference is adjusted for in the results of the positions of the tripods with respective standard deviation given in Table 4.5. The results from each epoch are given in the Appendix A. The positions are given in EUREF89 UTM Zone 32 with heights in Normal Null 2000 (NN2000) . The known point measured at last, for investigation of the accuracy of the RTK instrument, is Moholt shown in Figure 4.7. The highest standard deviation is in LCP 3 with a vertical standard deviation of 0.010 m. All other vertical standard deviations are 0.009 m.

(a) The positioning measurement of tripods With RTK rover

(b) Height measured from RTK to tripod

Figure 4.6: Leica Vivas GS16 GNSS rover used in experiment

Figure 4.7: The known point Moholt measured for accuracy investigation of the RTK GNSS equipment

Table 4.5: Measured position of the tripods in [m]

Point	N [m]	E [m]	NN2000 [m]	sN [m]	sE [m]	sH [m]
1	7031705.418	573721.796	157.806	0.004	0.003	0.009
2	7031731.113	573725.855	158.223	0.005	0.003	0.009
3	7031733.718	573712.890	158.240	0.005	0.003	0.010
4	7031708.915	573709.078	157.682	0.004	0.003	0.009
5	7031720.160	573717.143	158.028	0.004	0.003	0.009

The software GISLINE Land is used to make sure the baseline calculations of the true points are correctly derived. The distance between the attachment of the screw and the top of the roof model is 0.262 m. The LCP 1 and LCP 4 are pointed in the same direction and from a baseline through the ridge of the roofs. LCP 2 and LCP 3 are also in the same direction with a baseline through the roof ridge. LCP 5 is directed towards to the middle of LCP 3 at an angle of 45°. The alignment of the roof ridges where the LCP is placed on a tripod can be seen in Figure 4.8. The results of the calculation of the true points giving eight point illustrated on Figure 3.4 for each LCP are given in the Appendix B.

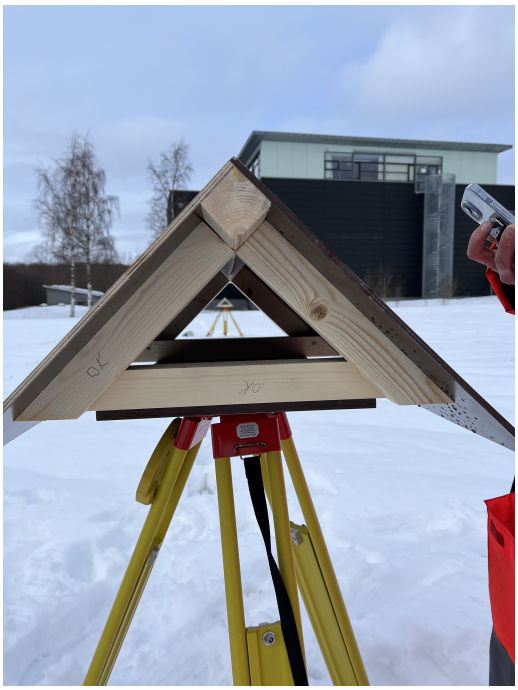

Figure 4.8: Roof model on tripod with directed roof ridge

4.1.7 True Plane Equation

The results of the calculated equation of the planes are given in Table 4.6. Each roof model has two planes (left and right). These are identified as shown in the illustration in Figure 4.9. The coefficients are negative for all coefficients in the left plane equation and negative for the c coefficient in the right plane equation. The coefficient a is derived as 0.218 in LCP 1 and LCP 4 and 0.221 in LCP 2 and LCP 3. The coefficient a in LCP 5 is given as 0.067. The coefficient b for LCP 1 and LCP 4 are 0.059 and 0.044 for LCP 2 and LCP 3. For LCP 5 the coefficient b is 0.215. The coefficient c is 0.225 to 0.226 for all LCPs. The constant d have similar values for corresponding baseline pair of LCP and side of plane,

Table 4.6: Equations of planes of each side on the roof models

LCP	Plane Equation
1L	-0.218x + -0.059y + -0.226z = -1570715.712
1R	0.218x + 0.059y + -0.226z = 1570644.058
2L	-0.221x + -0.044y + -0.225z = -1585671.270
2R	0.221x + 0.044y + -0.226z = 1585599.523
3L	-0.221x + -0.044y + -0.226z = -1585671.400
3R	0.221x + 0.044y + -0.225z = 1585599.645
4L	-0.218x + -0.059y + -0.226z = -1570715.685
4R	0.218x + 0.059y + -0.226z = 1570644.087
5L	-0.067x + -0.215y + -0.226z = -601512.4029
5R	0.067x + 0.215y + -0.226z = 601440.7638

4.2 Point Cloud Data Results

Each session performed results in a LAS file containing point cloud data. The results and visualisation and error measures from this data are presented in this section.

4.2.1 Point Cloud Extraction

The result file from the UAV experiment is in the LAS file format. The point cloud consists of point from the entire field and the points collected on each roof need to be extracted and separated for further calculations and comparison with the true planes. The software *CloudCompare* is used for the purpose of this separation. The tool *Segment* collects points of interest. Two separate files are stored for each roof model, one for left side of the roof model and one for right side of the roof model. The investigation can reveal the distribution of points on each side and if the point cloud has been edited correctly. The name convention of left and right side of the roof model is given by the point of view from the base of equipment to the area of flight seen on Figure 4.3 in red. The given left and right order of the LCPs are illustrated in Figure 4.9 where the base of equipment are on the right side of the LCPs. The files are saved as LAS and XYZ files for further calculations of point clouds in Python programming language.

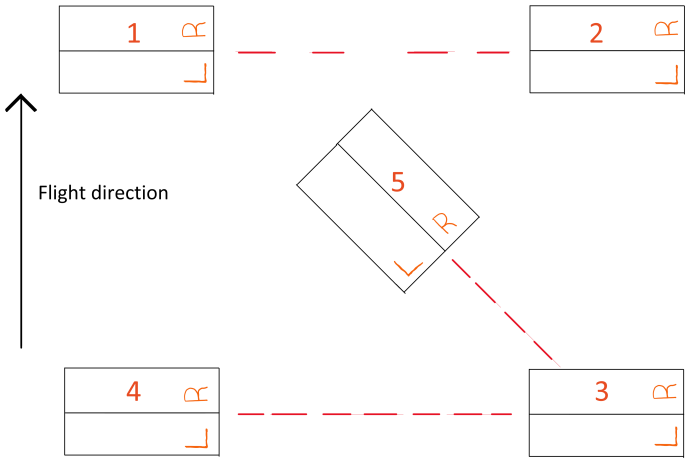

Figure 4.9: Left and right side of each LCP in the planned arrangement of the roof models

Further, the point clouds are studied and visually checked for any immediate errors. The point values are checked to be expected according to the EUREF89 UTM 32 reference frame with the height in NN2000. The files are also compared to each other and gross errors are investigated. The points are not GPS corrected and are not pre-processed point clouds. The reason for not correcting them is to facilitate evaluation of the points as-is and investigate the accuracy of the points in real-time.

4.2.2 Visualisations of the Point Cloud Data

An overview of the point cloud from S3 is shown in Figure 4.10. The LCPs can be seen in the colours red and orange. The snow surface is shown in the colours blue to green. The colours refer to the height of the points in this sub-point cloud where trees and buildings have been removed to better visualise the LCPs. The directions of the roof ridges is consistent with the planned placement from Figure 3.2 with the flight direction on Figure 4.10 from the left side.

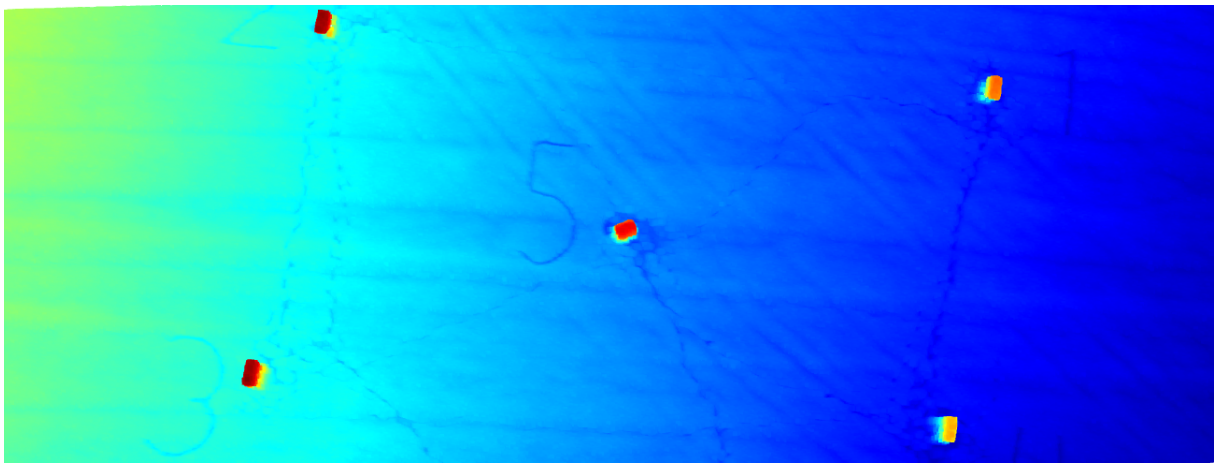

Figure 4.10: An overview of the point cloud data from session number 3, where the colours are given according to the height difference of the points in the point cloud

The sessions S2 and S7 are visually compared to each other in the software *CloudCompare*. The difference in amount of points detected can be investigated. The same point size have been used in both cases for the visualisation. The difference can be visualised from Figure 4.11 and Figure 4.12.

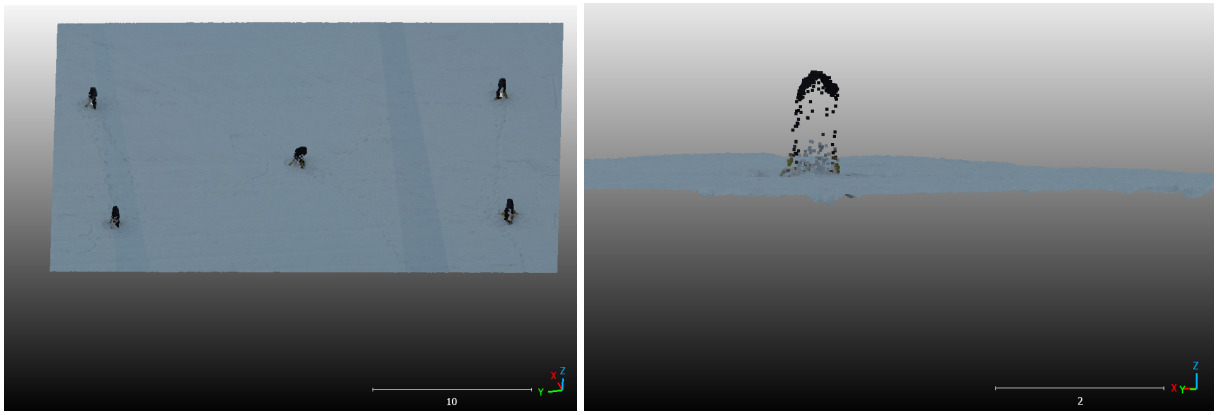

(a) An overview of the detected LCPs from S2

(b) Points detected on LCP number 5 in S2

Figure 4.11: Point cloud from session 2 with the flight speed 3 m/s and altitude 40 m above ground

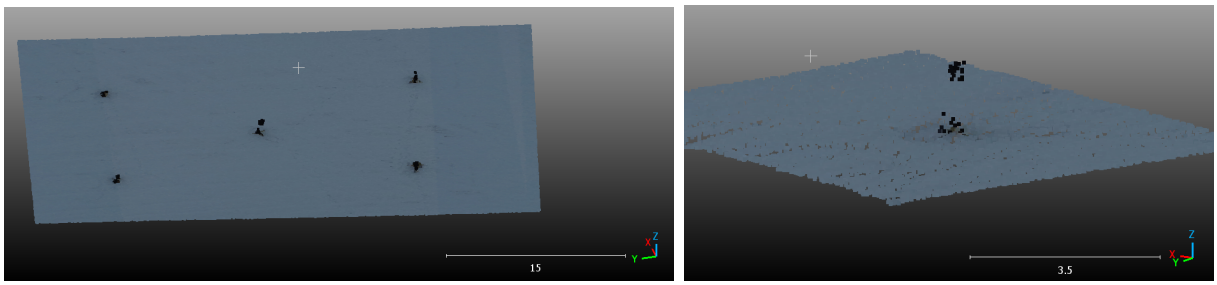

(a) An overview of the detected LCPs from S7 *(b) Points detected on LCP number 5 in S2*

Figure 4.12: Point cloud from session 7 with the flight speed 10 m/s and altitude 80 m above ground

Actual Detected Points of Each LCP

The points extracted with the software *CloudCompare* give the results of actual detected points on each LCP on each session as shown in Table 4.7. The number of points on the left (L) side, right (R) side and the total (T) amount of points are given. Regarding the sessions S4, S5, S6 and S7, the points could not be identified or did not have a clear structure to divide them in left and right. S2 is the session with the largest amount of points collected. LCP 5 is the roof model with the largest amount of points collected out of all roof models. S8 is the session with the least amount of collected points per LCP with the altitude of 40 m above ground level.

Table 4.7: Points detected on each LCP in each session

LCP / Session	S1	S2	S3	S4	S5	S6	S7	S8	S9
1 L	82	132	49	-	-	-	-	40	84
1 R	91	135	41	-	-	-	-	45	78
1 T	173	267	90	-	-	-	-	85	162
2 L	79	119	42	-	-	-	-	34	81
2 R	90	148	48	-	-	-	-	38	78
2 T	169	267	90	-	-	-	-	72	159
3 L	76	132	55	-	-	-	-	37	73
3 R	82	144	39	-	-	-	-	39	79
3 T	158	276	94	-	-	-	-	76	152
4 L	74	109	45	-	-	-	-	41	70
4 R	65	123	50	-	-	-	-	31	81
4 T	139	232	95	-	-	-	-	72	151
5 L	82	147	55	38	-	-	-	50	83
5 R	90	155	54	31	-	-	-	42	77
5 T	172	302	109	69	17	39	19	92	160

The actual detected number of point from each session on the planes are given in Table 4.8. The point density is the arithmetic mean of the five LCPs from each respective session. The

lack of detected roof points is the reason for no valid values for all sessions with a flying altitude of 80 m above ground level.

Table 4.8: Actual amount of points compared to the expected points per LCP in each session of flight

Session	S1	S2	S3	S4	S5	S6	S7	S8	S9
Speed $[m/s]$	5	3	8	3	8	5	10	10	5
Altitude $[m]$	40	40	40	80	80	80	80	40	40
Expected Points (LCP) $[pts/LCP]$	318	531	199	265	100	159	80	159	318
Actual Points (LCP) $[pts/LCP]$	162	269	96	-	-	-	-	79	157

Visualisation of First and Last Session

The first (S1) and last (S9) session are conducted at the same flight speed and altitude above ground (5 m/s, 40 m altitude). The visualisation of their point cloud data can be seen in Figure 4.13.

(a) An overview of the detected LCPs from S1 and S9

(b) Points detected on LCP number 5 in S1 and S9

Figure 4.13: Point cloud from session 1 and session 9 with the flight speed 5 m/s and altitude 40 m above ground

Point Cloud Data of LCPs on True Plane

The extraction of points on each LCP are visualised together with the true planes constructed from the equations of planes with true points as boundaries. The visualisations from LCP 1 and LCP 5 from S2 is given in Figure 4.14 and Figure 4.15. The axes are not orthonormal. Visualisation of the LCPs from all sessions are given in Appendix C.

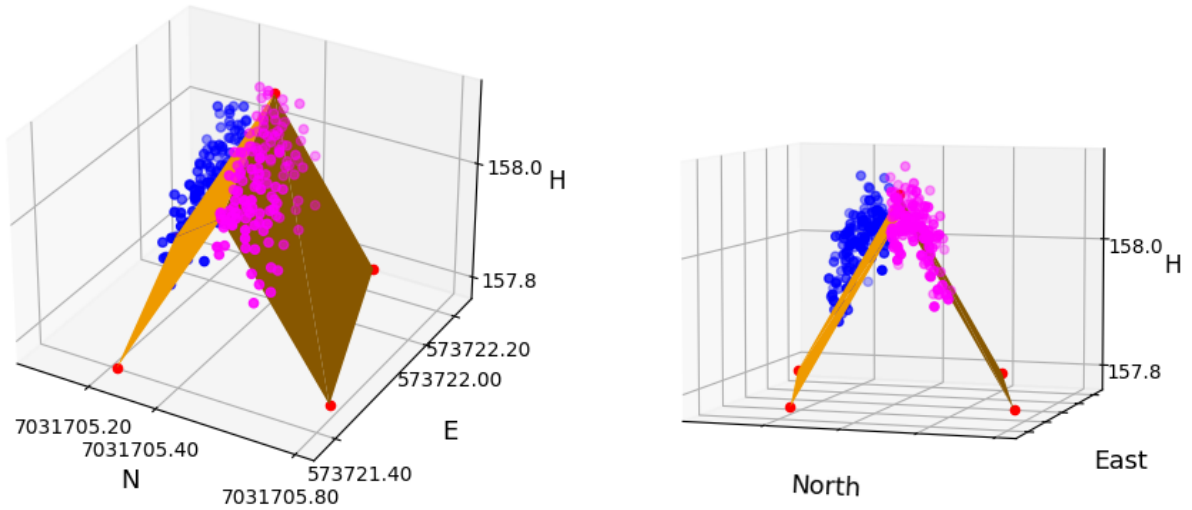

Figure 4.14: Extracted point cloud from LCP 1 in S2 from two different angles divided in blue and magenta colour for each side of the true plane. The red points are the true points on the true plane

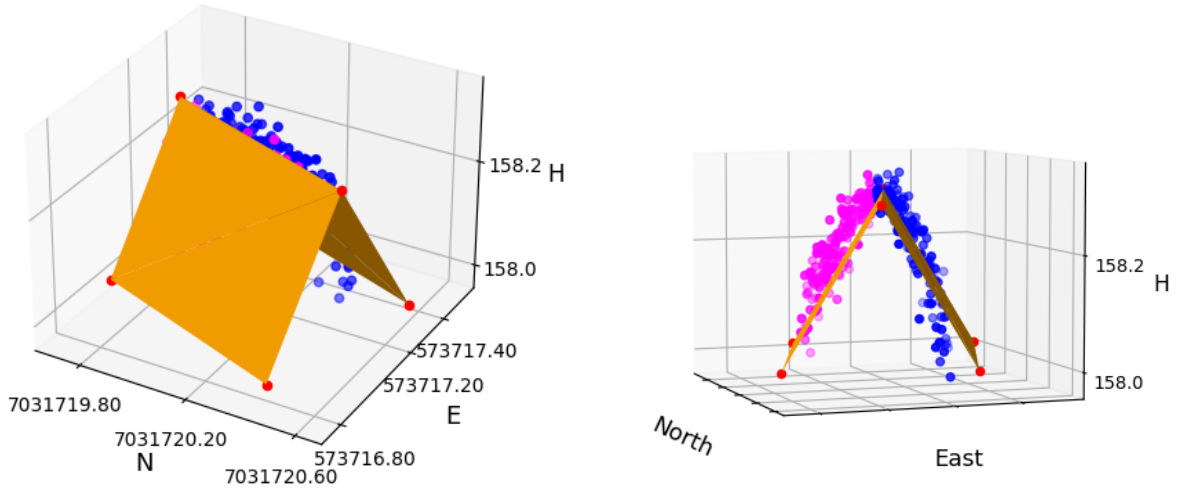

Figure 4.15: Extracted point cloud from LCP 5 in S2 from two different angles divided in blue and magenta colour for each side of the true plane. The red points are the true points on the true plane

4.2.3 Error Measures of Initial Point Cloud Data

Height of Snow Surface Points

In Table 4.4 the snow depth and height of snow surface are presented. In Table 4.9 the expected height values in NN2000 [m] are presented and in Table 4.10 the height of snow surface from a point in the point cloud next to close measured spot of tripod is collected. The highest value is measured in LCP 3 for both expected and actual height. The lowest value is measured in LCP 4 for the expected and actual height collected from point cloud.

Table 4.9: Expected height in NN2000 [m] of the surface

Number	LCP 1	LCP 2	LCP 3	LCP 4	LCP 5
Expected height of surface [m]	157.136	157.652	157.530	157.124	157.356

Table 4.10: Height check of tripods in first and last session given in NN2000 [m]

Session / Number	LCP 1	LCP 2	LCP 3	LCP 4	LCP 5
S1 Height [m]	156.995	157.415	157.483	156.835	157.239
S9 Height [m]	157.010	157.460	157.482	156.937	157.195

Distribution of Points Above and Below True Plane

The distribution of the points from the point cloud above and below each true plane for each session is shown in Table 4.11. The LCP 5 shows the largest number of points above compared to the points below the true plane. In most cases, more points are detected above the LCPs than below them. The only times more points from the point cloud have been detected below the true plane are at S2 on LCP 3, S3 on LCP 3 and LCP 4 and S8 on LCP 4.

Table 4.11: Number of points from point cloud above (A) and below (B) the true plane at each session

LCP / Session	S1	S2	S3	S8	S9
1 A	154	188	62	69	142
1 B	19	79	28	16	20
2 A	148	142	55	53	129
2 B	21	125	35	19	30
3 A	109	107	46	45	122
3 B	49	169	48	31	30
4 A	87	118	41	34	113
4 B	52	114	54	38	38
5 A	168	226	98	75	156
5 B	4	76	11	17	4

The Median & MAD of Distances to the True Plane

The results of points above and below true plane from Table 4.11 are used to calculate the perpendicular distance to the true plane. The maximum above point is given as max distance in Table 4.12. The maximum value below given as min distance in the same table. The median and MAD of the distances are presented for each distance calculated in each session. The maximum value of all sessions is 0.139 m in S1 at LCP 3. The minimum value of all sessions is -0.157 m in S2 at LCP 3. The highest median value is 0.054 m at S1 on LCP 5 and

the lowest is -0.001 m from S3 on LCP 3. the highest MAD is 0.038 m in S1 on LCP 4 and the lowest is 0.014 m in S3 and S9 at LCP 5.

Table 4.12: The minimum and maximum value of the perpendicular distance above and below the true plane. The median and MAD of the perpendicular distances

LCP / Session	S1	S2	S3	S8	S9
1 Min [m]	-0.056	-0.081	-0.043	-0.060	-0.035
1 Max [m]	0.138	0.101	0.079	0.081	0.107
1 Med [m]	0.043	0.017	0.018	0.020	0.034
1 MAD [m]	0.022	0.021	0.022	0.020	0.017
2 Min [m]	-0.077	-0.090	-0.064	-0.046	-0.066
2 Max [m]	0.109	0.106	0.071	0.086	0.121
2 Med [m]	0.037	0.002	0.009	0.018	0.027
2 MAD [m]	0.017	0.022	0.020	0.022	0.019
3 Min [m]	-0.057	-0.157	-0.070	-0.065	-0.041
3 Max [m]	0.139	0.078	0.058	0.060	0.070
3 Med [m]	0.022	-0.013	-0.001	0.010	0.020
3 MAD [m]	0.031	0.027	0.019	0.017	0.015
4 Min [m]	-0.073	-0.095	-0.060	-0.099	-0.064
4 Max [m]	0.106	0.107	0.065	0.074	0.092
4 Med [m]	0.023	0.003	-0.004	-0.004	0.021
4 MAD [m]	0.038	0.032	0.020	0.028	0.021
5 Min [m]	-0.0141	-0.081	-0.049	-0.041	-0.017
5 Max [m]	0.115	0.086	0.089	0.093	0.103
5 Med [m]	0.054	0.018	0.030	0.032	0.046
5 MAD [m]	0.018	0.018	0.014	0.017	0.014

Arithmetic Mean of the Absolute Distances

The arithmetic mean of the absolute values of the perpendicular distances are calculated for each roof model and session. These results are given in Figure 4.16. The highest mean values are calculated for S1. The LCP 5 in S1 have the highest mean value of above 0.054 m. LCP 3 have the lowest value during each session (minimum 0.021 m) except from S2, where LCP 2 has the lowest value of 0.026 m. The first and last sessions (S1 and S9) have the highest mean values.

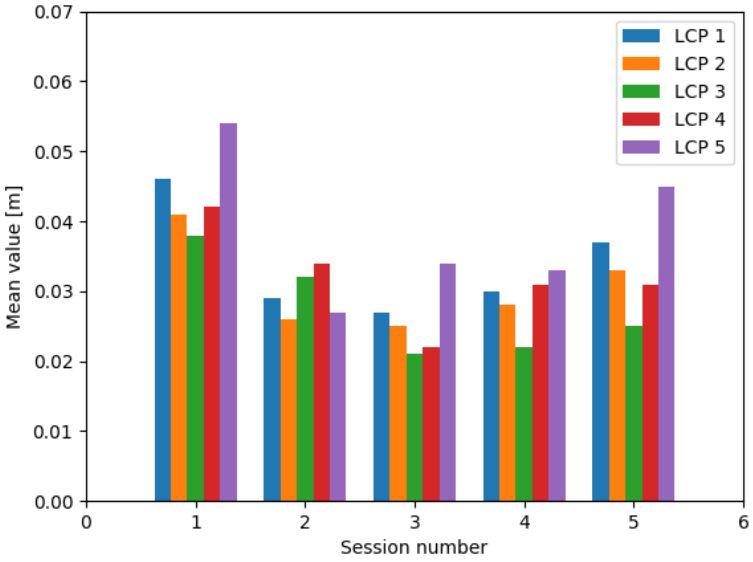

Figure 4.16: Mean values [m] of absolute perpendicular distance to the true plane of S1, S2, S3, S8 and S9

Standard Deviation of the Absolute Distances

The standard deviation calculated with the data of absolute perpendicular distances is given in Figure 4.17. The highest value of the standard deviations is 0.028 m for LCP 4 in S1. The lowest value is in S3 for LCP 4 of 0.014 m.

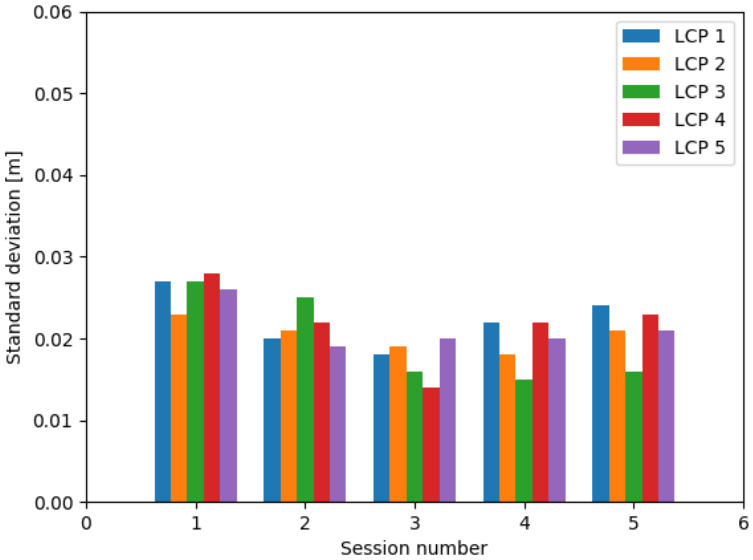

Figure 4.17: Standard deviation [m] of absolute perpendicular distance to the true plane of S1, S2, S3, S8 and S9

RMSE Error Measured of the Absolute Distances

The results for the RMSE of the absolute perpendicular distances from each LCP for each session are given in Figure 4.18. The highest RMSE are given in S1 where LCP 1 is 0.054 m and LCP 5 is 0.060 m. The LCP 5 at S9 have RMSE of 0.05 m, but all other RMSE shows results below 0.05 m. The lowest value is 0.027 m for LCP 3 and LCP 4 in S3 and LCP 3 in S8.

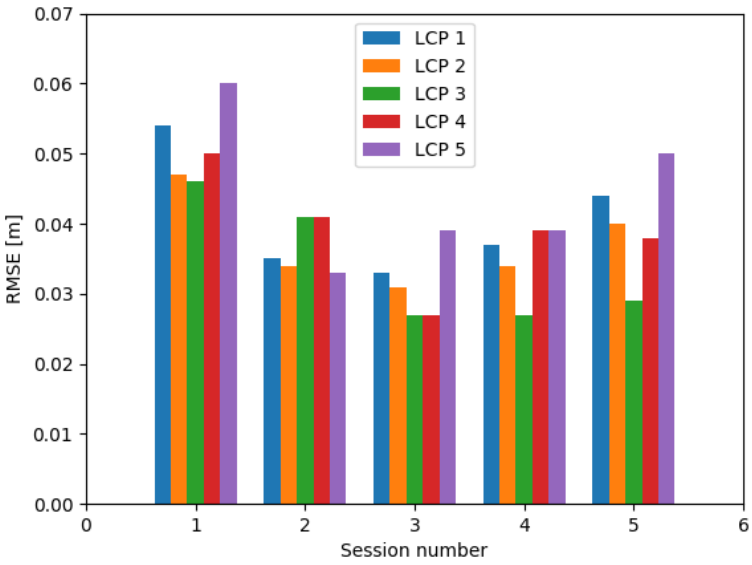

Figure 4.18: RMSE [m] of absolute perpendicular distance to the true plane of S1, S2, S3, S8 and S9

4.3 RANSAC Estimations of Point Cloud

In this section the results of RANSAC estimated point cloud is presented. Inliers and the plane equation constructed from the inliers of the planes are calculated with the RANSAC algorithm. Further the results of error measures, angle, mid-point and volume calculations are presented. The RANSAC algorithm with the residual threshold of 0.02.

4.3.1 RANSAC Inliers

The number of inliers extracted by the RANSAC algorithm at each LCP from each session are given in Table 4.13. The greatest amount of inliers extracted is 196 points at LCP 5 in S2. The LCP 5 have the highest amount of inliers at each session compared to the other LCPs. The session with the lowest amount of inliers is S8. In S8 the LCP 2 extracted 40 points. This is the lowest amount of points extracted.

Table 4.13: Amount of inliers estimated with the RANSAC algorithm

LCP / Session	S1	S2	S3	S8	S9
1	103	150	56	53	99
2	107	149	56	40	94
3	97	170	70	52	103
4	93	151	63	48	85
5	122	196	80	57	115

Distribution of RANSAC Inliers Above and Below True Plane

The distribution of the inlier points above and below each true plane for each session is given in Table 4.14. During S1 zero points are detected below the true plane at LCP 1, LCP 2 and LCP 5. In S9 this only occurs at LCP 5. Both S1 and S9 show a low amount of points detected below the true planes. In each session except for S2, a low amount of points are collected for LCP 5, with the maximum of 6. The LCP 3 in S2 is the only occurrence where there are more points collected below the true plane than above.

Table 4.14: Number of RANSAC inlier points per LCP above (A) and below (B) the true plane at each session

LCP / Session	S1	S2	S3	S8	S9
1 A	103	128	43	46	98
1 B	0	22	13	7	1
2 A	107	88	35	38	92
2 B	0	61	21	2	2
3 A	70	82	38	34	100
3 B	27	88	32	18	3
4 A	55	83	34	26	71
4 B	38	68	29	22	14
5 A	122	159	74	55	115
5 B	0	37	6	2	0

4.3.2 RANSAC Plane Equation

The results for the calculated equations of the planes from RANSAC are shown in Table 4.15, Table 4.16 Table 4.17, Table 4.18 and Table 4.19. Each roof model has two planes (left and right). These are identified as per the illustration in Figure 4.9. All c coefficients of the plane equation have a negative value and all coefficients on left plane are negative.

Table 4.15: Equations of planes on each side of the roof models from RANSAC inliers in S1

LCP	Plane Equation S1
1L	-0.138x + -0.489y + -0.861z = -3520552.639
1R	0.147x + 0.520y + -0.842z = 3737653.570
2L	-0.083x + -0.527y + -0.846z = -3753830.246
2R	0.172x + 0.638y + -0.750z = 4586633.650
3L	-0.138x + -0.688y + -0.712z = -4919549.409
3R	0.130x + 0.706y + -0.696z = 5039542.531
4L	-0.241x + -0.741y + -0.627z = -5348634.783
4R	0.108x + 0.512y + -0.852z = 3659465.943
5L	-0.717x + -0.265y + -0.645z = -2272331.485
5R	0.743x + 0.220y + -0.632z = 1973952.822

Table 4.16: Equations of planes on each side of the roof models from RANSAC inliers in S2

LCP	Plane Equation S2
1L	-0.154x + -0.609y + -0.778z = -4369382.618
1R	0.201x + 0.808y + -0.554z = 5795772.108
2L	-0.149x + -0.627y + -0.765z = -4492296.277
2R	0.129x + 0.750y + -0.649z = 5348115.409
3L	-0.114x + -0.656y + -0.746z = -4676613.726
3R	0.124x + 0.726y + -0.677z = 5175428.358
4L	-0.228x + -0.793y + -0.564z = -5709319.701
4R	0.161x + 0.618y + -0.769z = 4439791.119
5L	-0.689x + -0.219y + -0.691z = -1936513.306
5R	0.691x + 0.229y + -0.685z = 2007675.423

Table 4.17: Equations of planes on each side of the roof models from RANSAC inliers in S3

LCP	Plane Equation S3
1L	-0.173x + -0.855y + -0.489z = -6110668.867
1R	0.217x + 0.474y + -0.853z = 3460665.666
2L	-0.248x + -0.861y + -0.444z = -6195505.918
2R	0.053x + 0.342y + -0.938z = 2432699.938
3L	-0.103x + -0.468y + -0.878z = -3347386.474
3R	0.148x + 0.710y + -0.688z = 5078960.231
4L	-0.187x + -0.670y + -0.719z = -4817877.826
4R	0.143x + 0.569y + -0.810z = 4083119.894
5L	-0.766x + -0.175y + -0.619z = -1670003.133
5R	0.747x + 0.148y + -0.648z = 1470234.191

Table 4.18: Equations of planes on each side of the roof models from RANSAC inliers in S8

LCP	Plane Equation S8
1L	-0.126x + -0.529y + -0.839z = -3791052.209
1R	0.163x + 0.387y + -0.907z = 2814891.866
2L	-0.186x + -0.654y + -0.733z = -4705448.065
2R	-0.140x + -0.768y + 0.625z = -5480137.077
3L	-0.084x + -0.625y + -0.776z = -4445892.445
3R	0.085x + 0.668y + -0.739z = 4746241.435
4L	-0.044x + -0.127y + -0.991z = -871325.140
4R	0.187x + 0.653y + -0.734z = 4697299.327
5L	-0.649x + -0.245y + -0.720z = -2091796.454
5R	0.748x + 0.240y + -0.619z = 2113144.938

Table 4.19: Equations of planes on each side of the roof models from RANSAC inliers in S9

LCP	Plane Equation S9
1L	-0.181x + -0.667y + -0.722z = -4795293.682
1R	0.229x + 0.693y + -0.683z = 5007075.865
2L	-0.063x + -0.714y + -0.697z = -5058366.217
2R	0.131x + 0.680y + -0.721z = 4858161.402
3L	-0.163x + -0.726y + -0.668z = -5201253.775
3R	0.149x + 0.693y + -0.705z = 4958385.389
4L	-0.221x + -0.916y + -0.335z = -6567834.403
4R	0.267x + 0.807y + -0.527z = 5827953.472
5R	-0.747x + -0.260y + -0.611z = -2254792.640
5L	0.757x + 0.222y + -0.614z = 1993792.953

The planes with the boundaries given by the minimal BBox of the inliers are given for each session in Figure 4.19, Figure 4.20, Figure 4.21, Figure 4.22 and Figure 4.23. The inliers extracted on each side are given in magenta and blue colour. The RANSAC created planes are given in orange with the bounding points in red. The figures do not have orthonormal axes, but illustrate the distribution of inliers on the planes. Some of the constructed planes do not have the same size on the left and right side. The planes are also, in many cases, not having the same highest boundary points and some of the planes are overlapping each other.

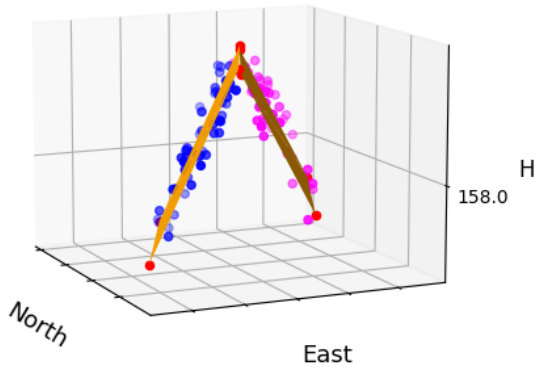

(a) Session 1 nr1

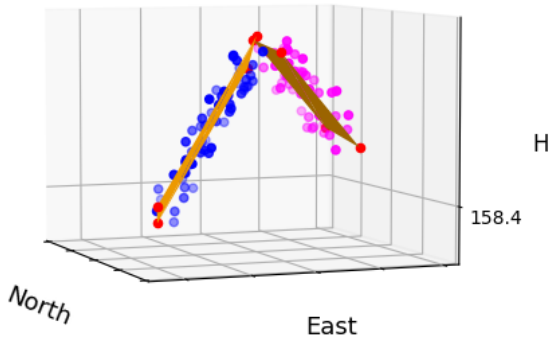

(b) Session 1 nr2

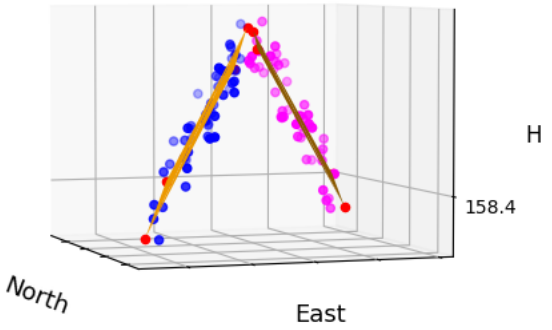

(c) Session 1 nr3

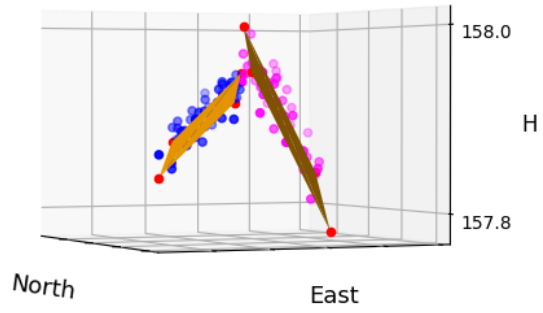

(d) Session 1 nr4

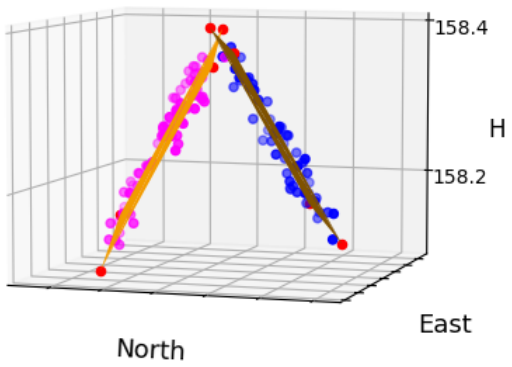

(e) Session 1 nr5

Figure 4.19: RANSAC planes constructed from inliers from session 1, where the orange planes are the RANSAC estimated planes with the boundaries given as red points. The blue and magenta points are the inliers given on each side of the plane

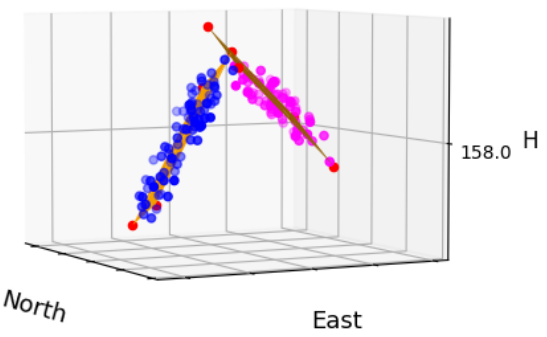

(a) Session 2 nr1

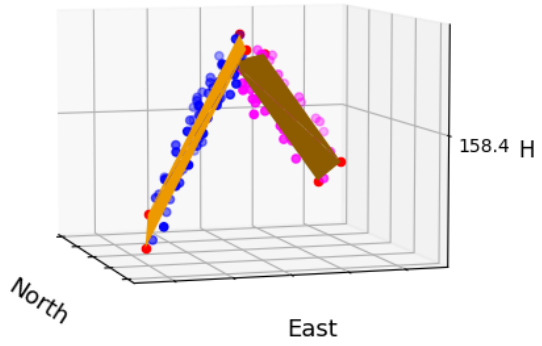

(b) Session 2 nr2

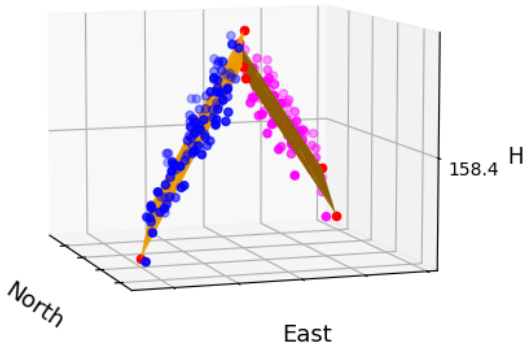

(c) Session 2 nr3

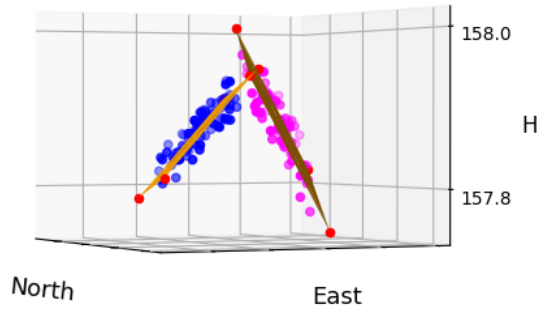

(d) Session 2 nr4

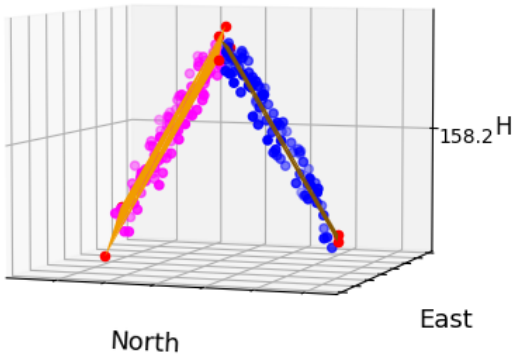

(e) Session 2 nr5

Figure 4.20: RANSAC planes constructed from inliers from session 2, where the orange planes are the RANSAC estimated planes with the boundaries given as red points. The blue and magenta points are the inliers given on each side of the plane

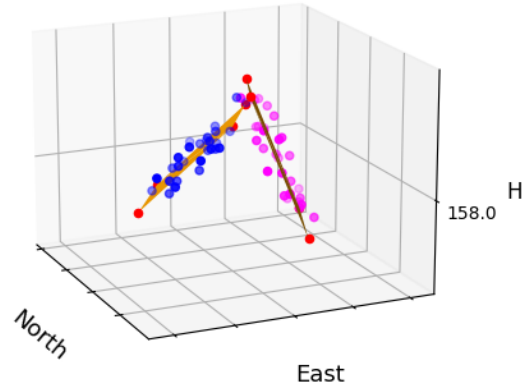

(a) Session 3 nr1

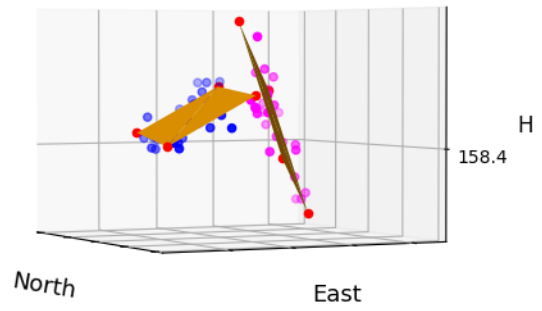

(b) Session 3 nr2

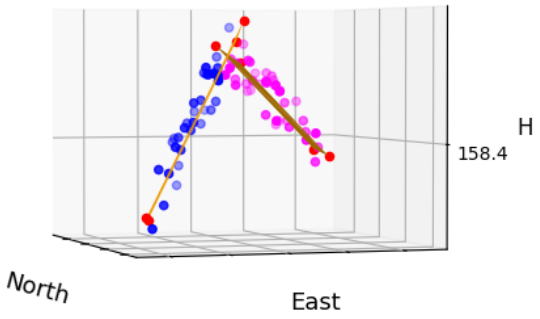

(c) Session 3 nr3

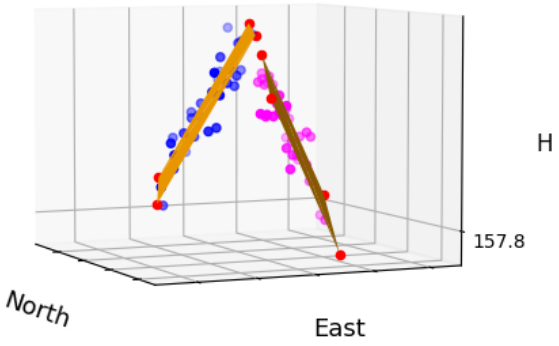

(d) Session 3 nr4

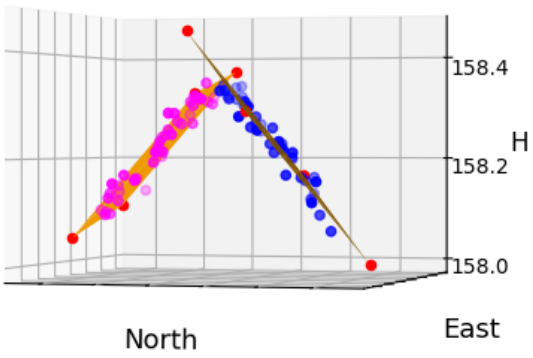

(e) Session 3 nr5

Figure 4.21: RANSAC planes constructed from inliers from session 3, where the orange planes are the RANSAC estimated planes with the boundaries given as red points. The blue and magenta points are the inliers given on each side of the plane

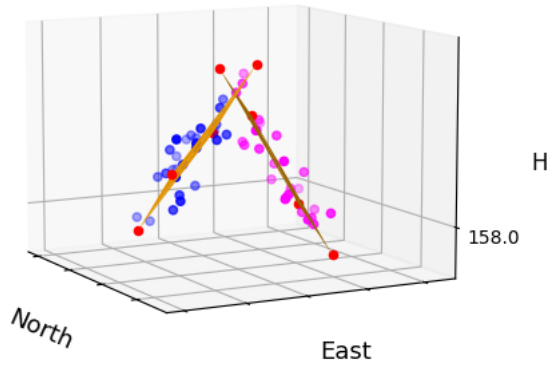

(a) Session 8 nr1

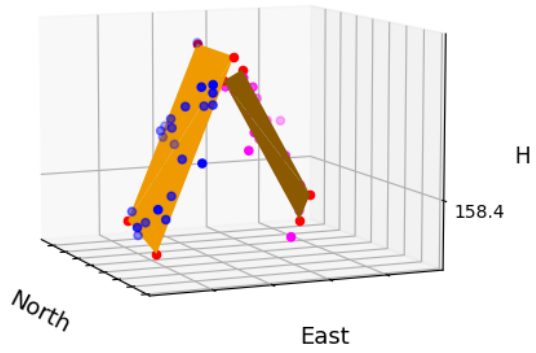

(b) Session 8 nr2

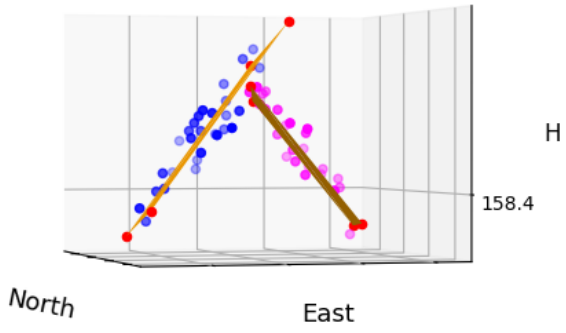

(c) Session 8 nr3

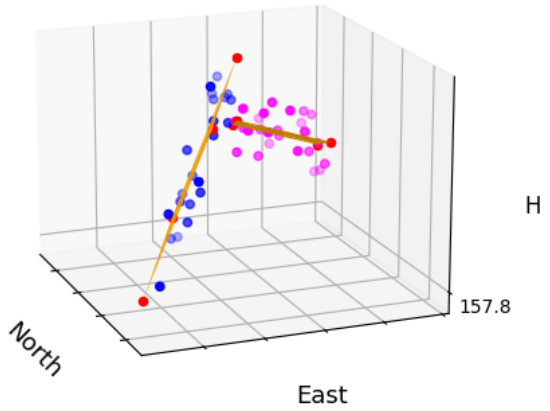

(d) Session 8 nr4

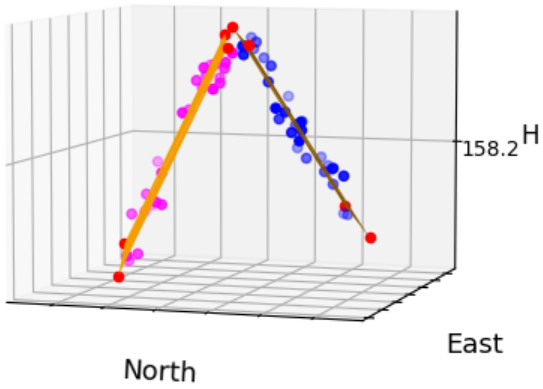

(e) Session 8 nr5

Figure 4.22: RANSAC planes constructed from inliers from session 8, where the orange planes are the RANSAC estimated planes with the boundaries given as red points. The blue and magenta points are the inliers given on each side of the plane

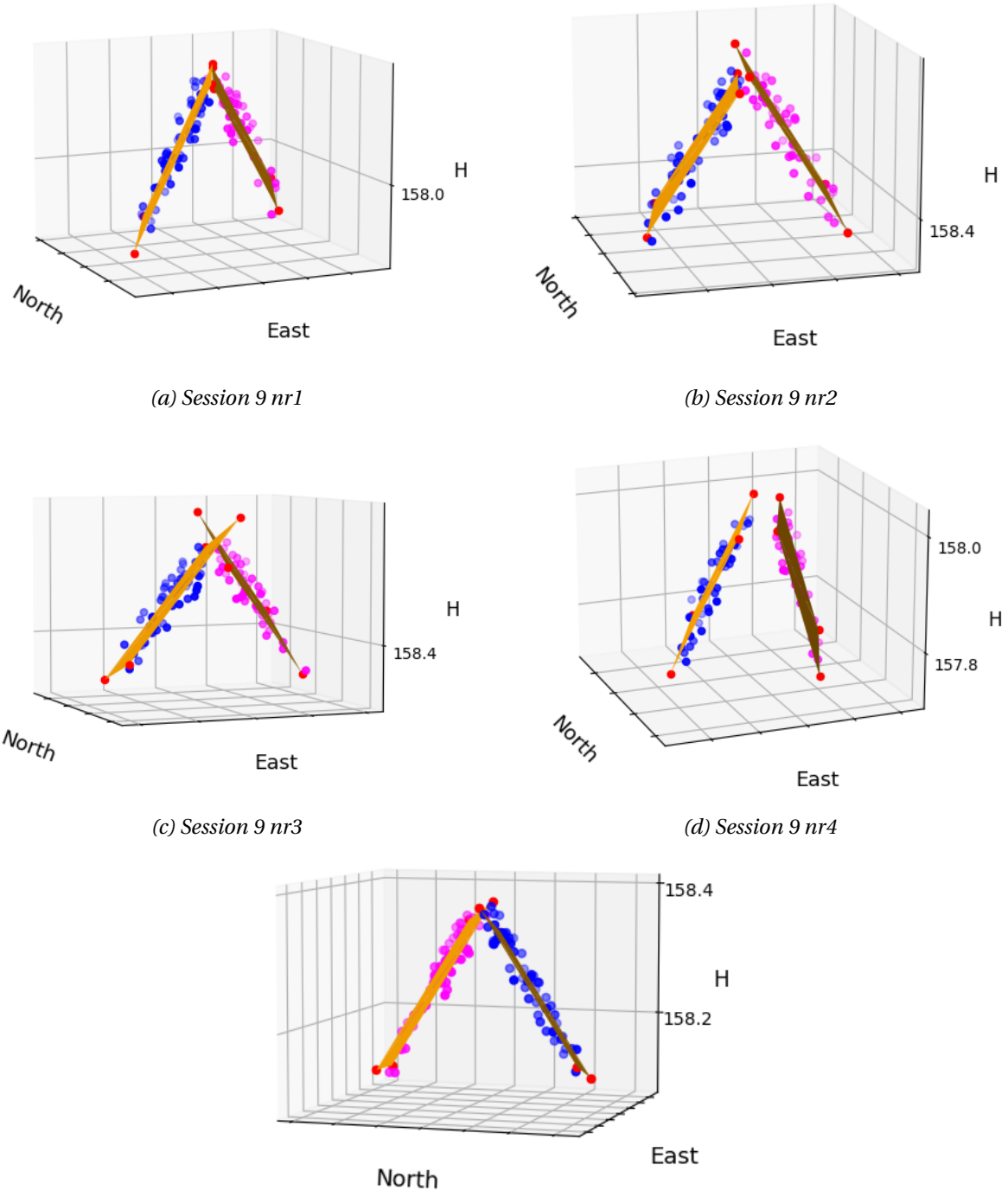

(a) Session 9 nr1

(b) Session 9 nr2

(c) Session 9 nr3

(d) Session 9 nr4

(e) Session 9 nr5

Figure 4.23: RANSAC planes constructed from inliers from session 9, where the orange planes are the RANSAC estimated planes with the boundaries given as red points. The blue and magenta points are the inliers given on each side of the plane

4.3.3 Error Measures of RANSAC Inliers

The Median & MAD of Inliers on RANSAC Planes

The results of the RANSAC inliers above and below the true planes are given in Table 4.20. The maximum point above is given as max distance in Table 4.20. The maximum value below given as min distance in the same table. The median and MAD of the distances are presented for each distance calculated in each session. The maximum value for all sessions is 0.095 m in S1 at LCP 5. The minimum value of all sessions is -0.079 m in S8 at LCP 4. The highest median value is 0.056 m at S1 on LCP 5 and the lowest is -0.002 m from S3 on LCP 3. The highest MAD is 0.035 m in S1 on LCP 4 and the lowest is 0.009 m in S8 at LCP 5.

Table 4.20: The minimum, maximum value and median and MAD of distance from inliers above and below the true plane

LCP / Session	S1	S2	S3	S8	S9
1 Min [m]	0.002	-0.014	-0.043	-0.023	-0.006
1 Max [m]	0.091	0.065	0.078	0.080	0.054
1 Med [m]	0.043	0.023	0.018	0.024	0.030
1 MAD [m]	0.015	0.014	0.013	0.020	0.010
2 Min [m]	0.006	-0.042	-0.033	-0.010	-0.011
2 Max [m]	0.075	0.036	0.058	0.059	0.064
2 Med [m]	0.042	0.003	0.009	0.024	0.031
2 MAD [m]	0.011	0.011	0.016	0.013	0.012
3 Min [m]	-0.020	-0.061	-0.059	-0.027	-0.004
3 Max [m]	0.075	0.040	0.030	0.050	0.044
3 Med [m]	0.031	-0.005	-0.002	0.012	0.021
3 MAD [m]	0.026	0.024	0.018	0.015	0.010
4 Min [m]	-0.046	-0.070	-0.035	-0.079	-0.064
4 Max [m]	0.088	0.058	0.045	0.052	0.082
4 Med [m]	0.017	0.013	-0.002	0.005	0.028
4 MAD [m]	0.035	0.028	0.021	0.026	0.017
5 Min [m]	0.004	-0.021	-0.022	-0.003	0.008
5 Max [m]	0.095	0.054	0.074	0.062	0.081
5 Med [m]	0.056	0.018	0.030	0.034	0.044
5 MAD [m]	0.017	0.014	0.011	0.009	0.011

The Arithmetic Mean of the Inliers Distance to the RANSAC Planes

The arithmetic mean of the absolute values of the perpendicular distances to the true plane of the RANSAC inliers are calculated. These results are given in Figure 4.24. The highest mean values are derived for S1. The LCP 5 in S1 have the highest mean value of 0.055 m. LCP 3 have the lowest value at S1, S3, S8 and S9, but the lowest value among all sessions is in S3 where LCP 2 has the mean value of 0.014 m. The first and last sessions (S1 and S9) have the highest mean values of LCP 5.

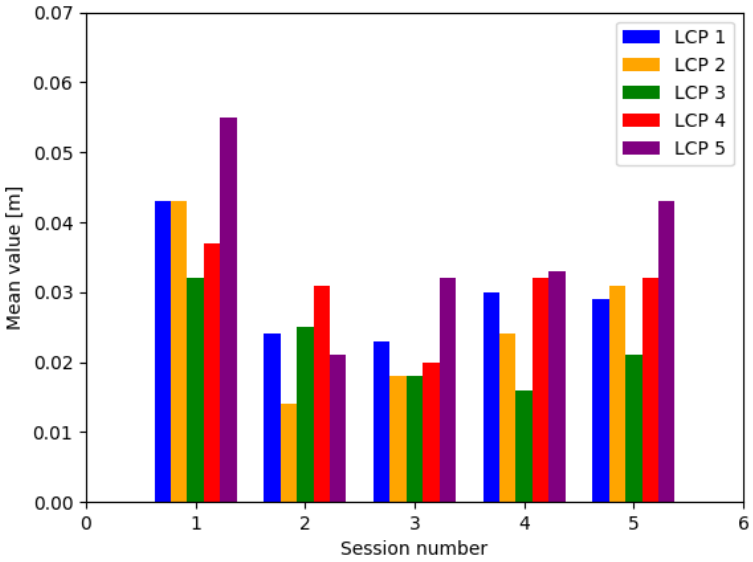

Figure 4.24: Mean values [m] of absolute perpendicular distance of RANSAC inliers to the true plane of S1, S2, S3, S8 and S9

The Standard Deviation of the Inliers Distance to the RANSAC Planes

The standard deviation calculated with the data of absolute perpendicular distances from the RANSAC inliers to the true planes are shown in Figure 4.25. The highest standard deviations of all LCPs is 0.023 m of LCP 4 and LCP 5 in S1. The lowest value is given in S2 of LCP 2.

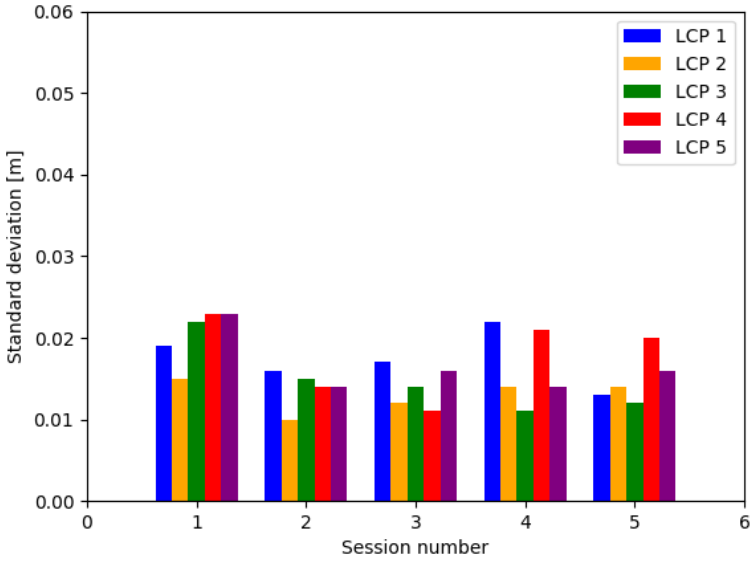

Figure 4.25: Standard deviation [m] of absolute perpendicular distance of RANSAC inliers to the true plane of S1, S2, S3, S8 and S9

The RMSE of the Inliers Distance to the RANSAC Planes

The results of the RMSE of the absolute perpendicular distances from RANSAC inliers to each LCP at each session are given in Figure 4.26. The highest RMSE is given in S1 where LCP 5 is 0.060 m. At S2, S3 and S8 all RMSE values are below 0.040 m. The lowest value is for LCP 2 in S2 at 0.017 m.

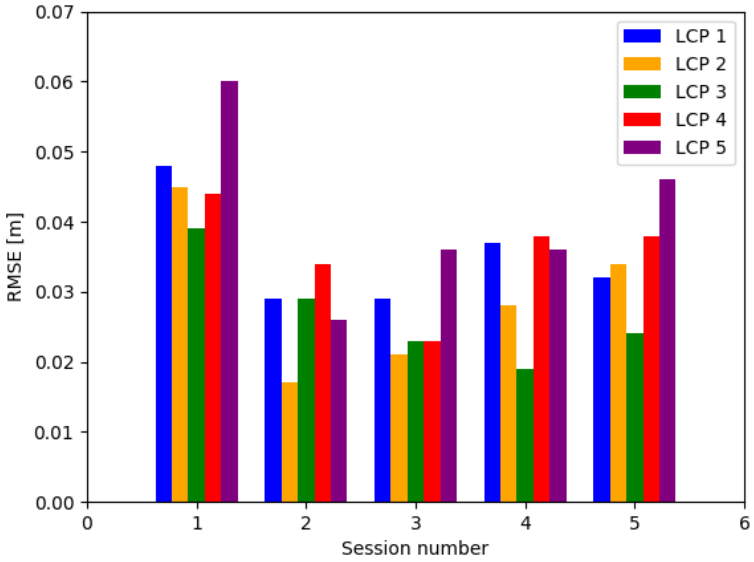

Figure 4.26: RMSE [m] of absolute perpendicular distance of RANSAC inliers to the true plane of S1, S2, S3, S8 and S9

4.3.4 Angle Comparison Between Planes

The angle between each RANSAC plane in each session is given in Table 4.21. Three of the RANSAC planes have an angle of 90°. At S1 for RANSAC roof model 3, S2 for RANSAC roof model 2 and S9 for RANSAC roof model 2 this occurs. The highest angle value is 131° at roof model 4 in S8. There is no angle detected lower than 90 degrees.

Table 4.21: Angle difference between planes constructed with the RANSAC algorithm

Plane Angle [°]/ Session	S1	S2	S3	S8	S9
1	117	95	91	122	91
2	106	90	96	94	90
3	90	91	105	99	93
4	97	94	100	131	128
5	101	93	101	96	104

4.3.5 Mid-point Difference of Inliers & True Plane

The mid-points of each set of RANSAC inliers are illustrated in Figure 4.27, Figure 4.28, Figure 4.29, Figure 4.30 and Figure 4.31. The mid-point are illustrated with the magenta colour and the mid-point of the true plane with the green colour. The true planes are given in the colour orange and with red points indicating the true points of the true plane. The plots do not have orthonormal axes. For all mid-points, the difference between the mid-point of the inliers and the mid-point of the true plane is that the points have a lot higher position on the true plane. For some of the RANSAC mid-points, the points are shifted left (North).

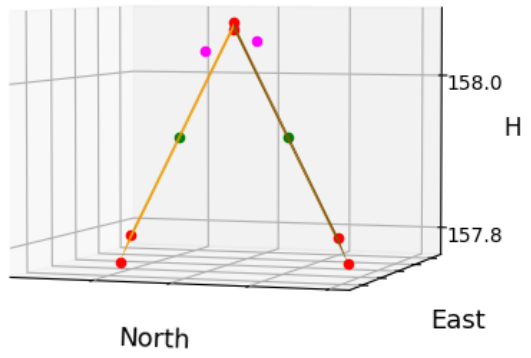

(a) Session 1 LCP 1

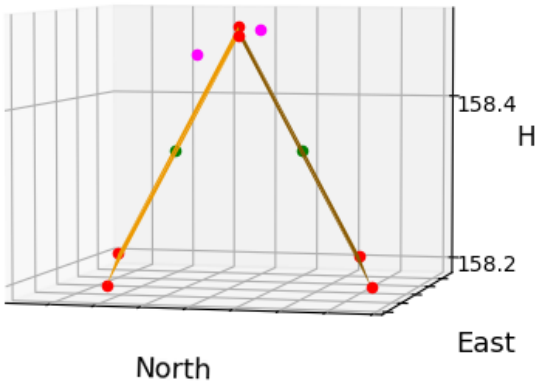

(b) Session 1 LCP 2

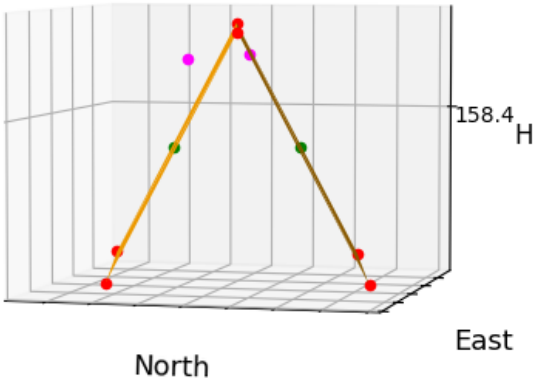

(c) Session 1 LCP 3

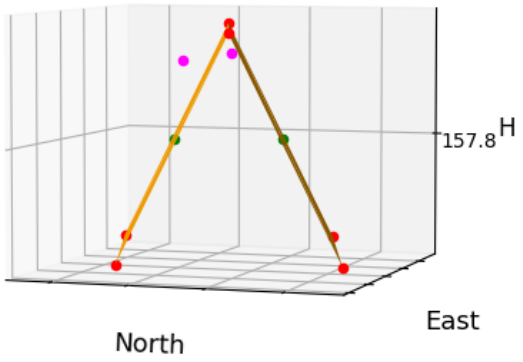

(d) Session 1 LCP 4

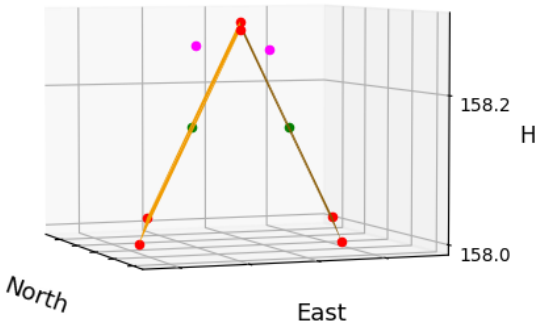

(e) Session 1 LCP 5

Figure 4.27: RANSAC mid-point given in magenta colour and true plane mid-point given in green colour on true plane session 1, where orange planes are the true planes, red points are the known points as boundaries for the true plane

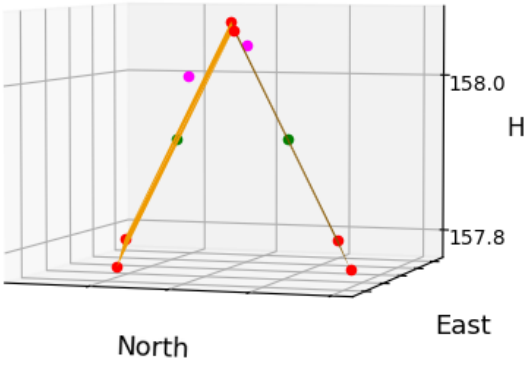

(a) Session 2 LCP 1

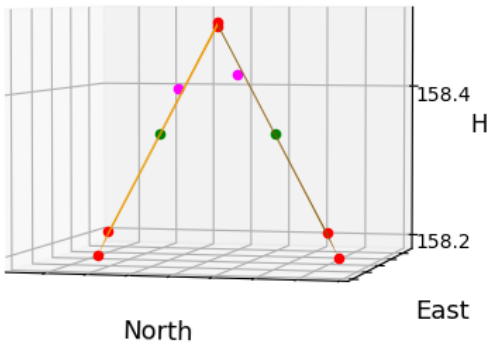

(b) Session 2 LCP 2

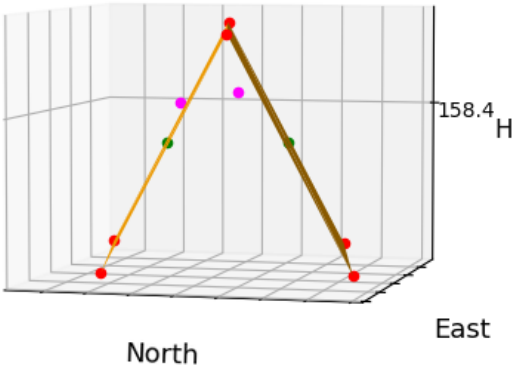

(c) Session 2 LCP 3

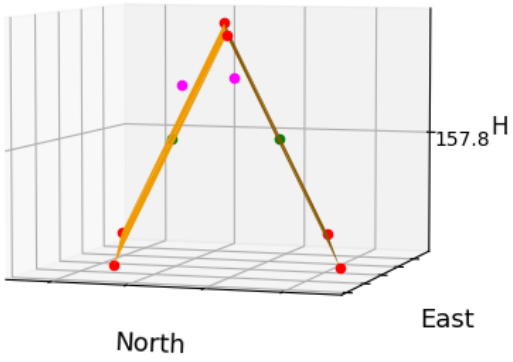

(d) Session 2 LCP 4

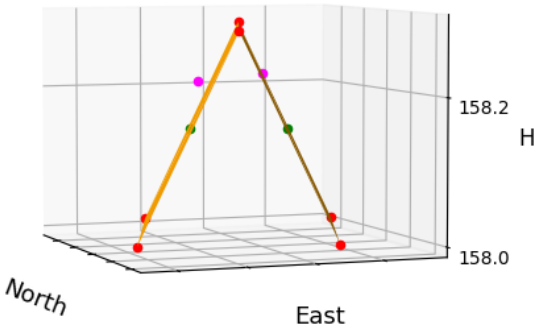

(e) Session 2 LCP 5

Figure 4.28: RANSAC mid-point and true plane mid-point on true plane session 2, where orange planes are the true planes, red points are the known points as boundaries for the true plane

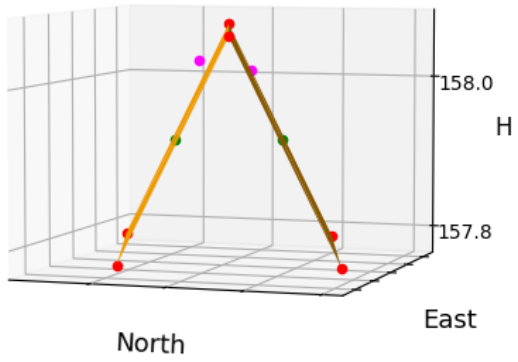

(a) Session 3 LCP 1

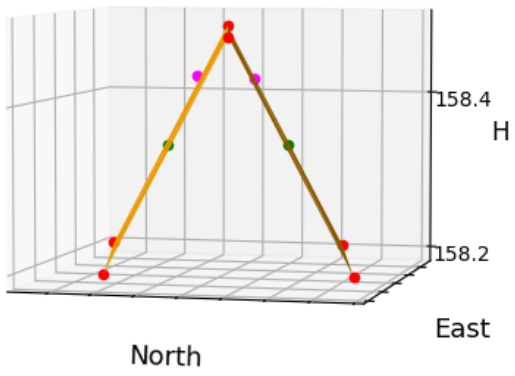

(b) Session 3 LCP 2

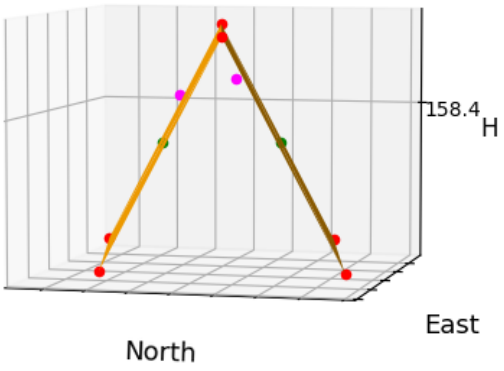

(c) Session 3 LCP 3

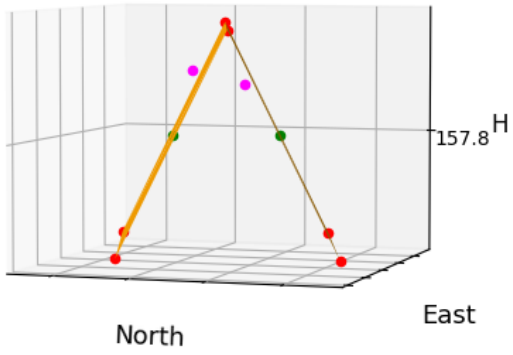

(d) Session 3 LCP 4

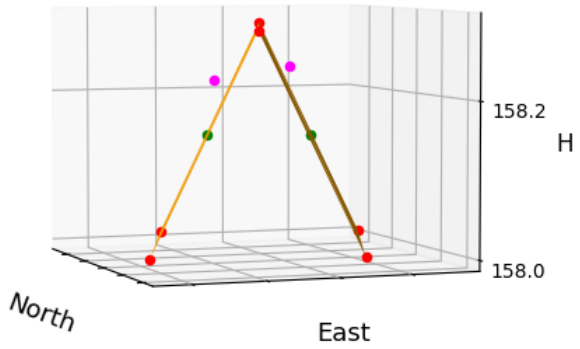

(e) Session 3 LCP 5

Figure 4.29: RANSAC mid-point and true plane mid-point on true plane session 3, where orange planes are the true planes, red points are the known points as boundaries for the true plane

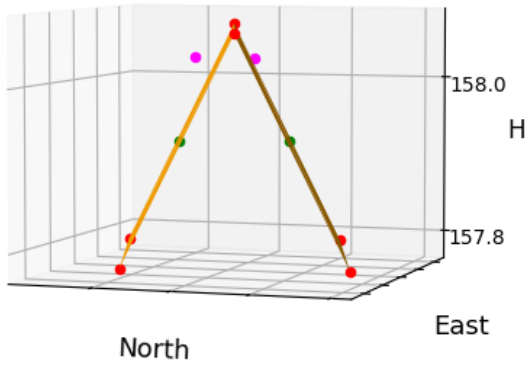

(a) Session 8 LCP 1

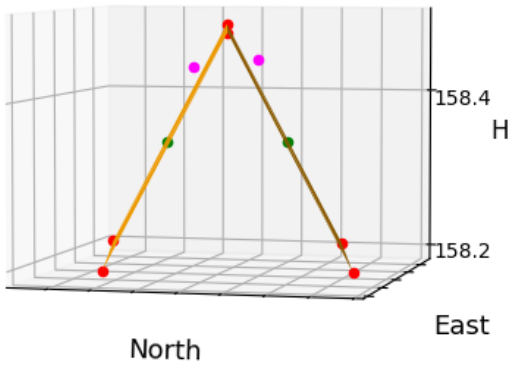

(b) Session 8 LCP 2

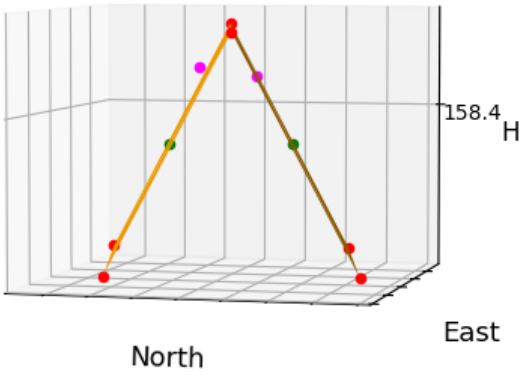

(c) Session 8 LCP 3

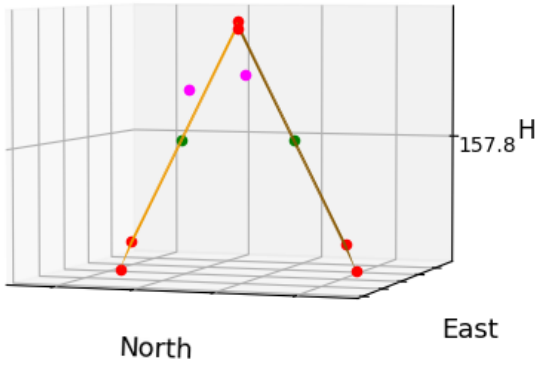

(d) Session 8 LCP 4

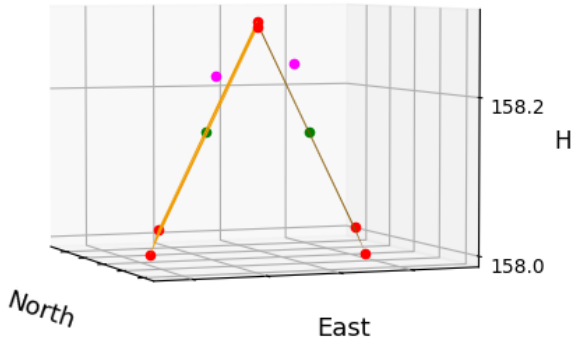

(e) Session 8 LCP 5

Figure 4.30: RANSAC mid-point and true plane mid-point on true plane session 8, where orange planes are the true planes, red points are the known points as boundaries for the true plane

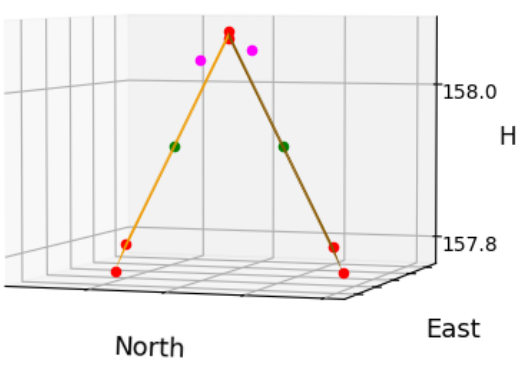

(a) Session 9 LCP 1

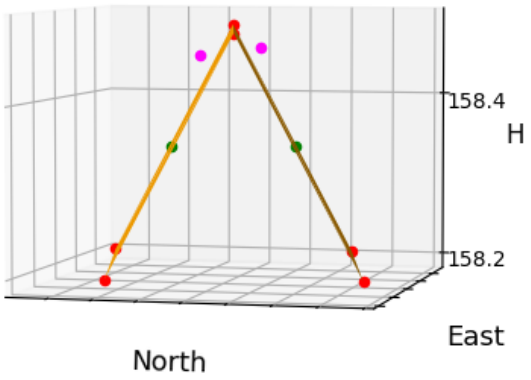

(b) Session 9 LCP 1

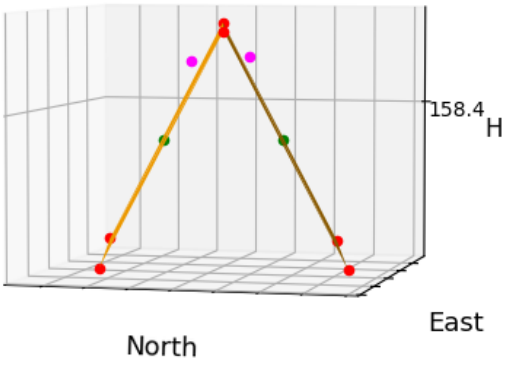

(c) Session 9 LCP 3

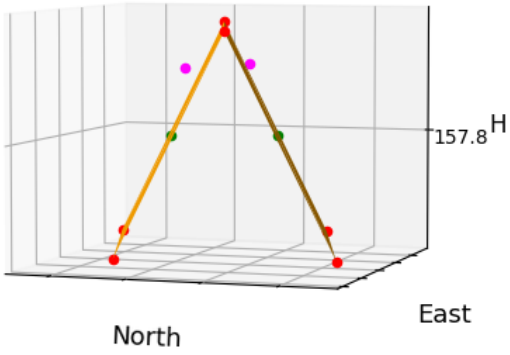

(d) Session 9 LCP 4

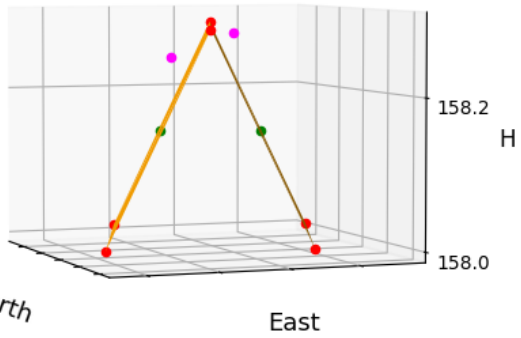

(e) Session 9 LCP 5

Figure 4.31: RANSAC mid-point and true plane mid-point on true plane session 9, where orange planes are the true planes, red points are the known points as boundaries for the true plane

The difference of each mid-point of each session is given in Figure 4.32, Figure 4.33, Figure 4.34, Figure 4.35 and Figure 4.36. The red colour illustrates the difference in N-direction, The green in E-direction and the blue in height (NN2000). Each of the differences is given in metres. For all differences, the height value is negative, indicating its above the mid-point of the true plane. The highest difference in N-direction in S1, S2, S8 and S9 is from LCP 1 and LCP 2. For S3 the highest difference in N-direction is in LCP 1.

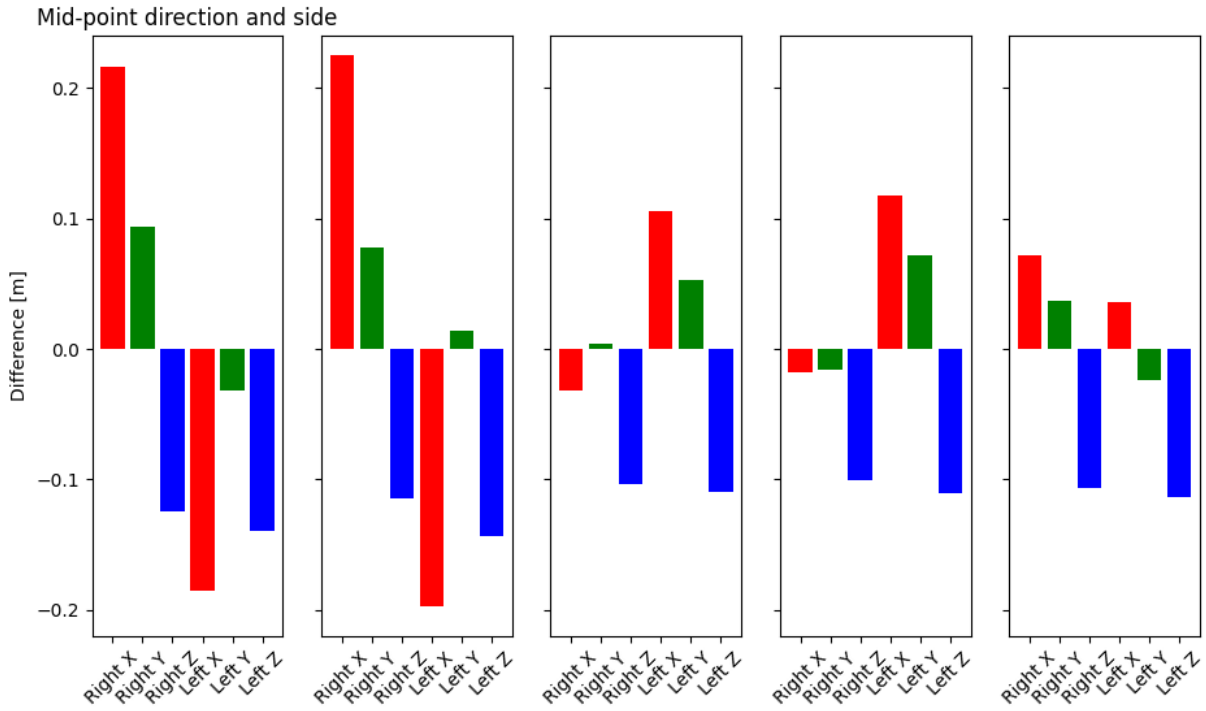

Figure 4.32: RANSAC mid-point and true plane mid-point on true plane session 1, where north-difference is given in red, east-difference in green and height difference in blue

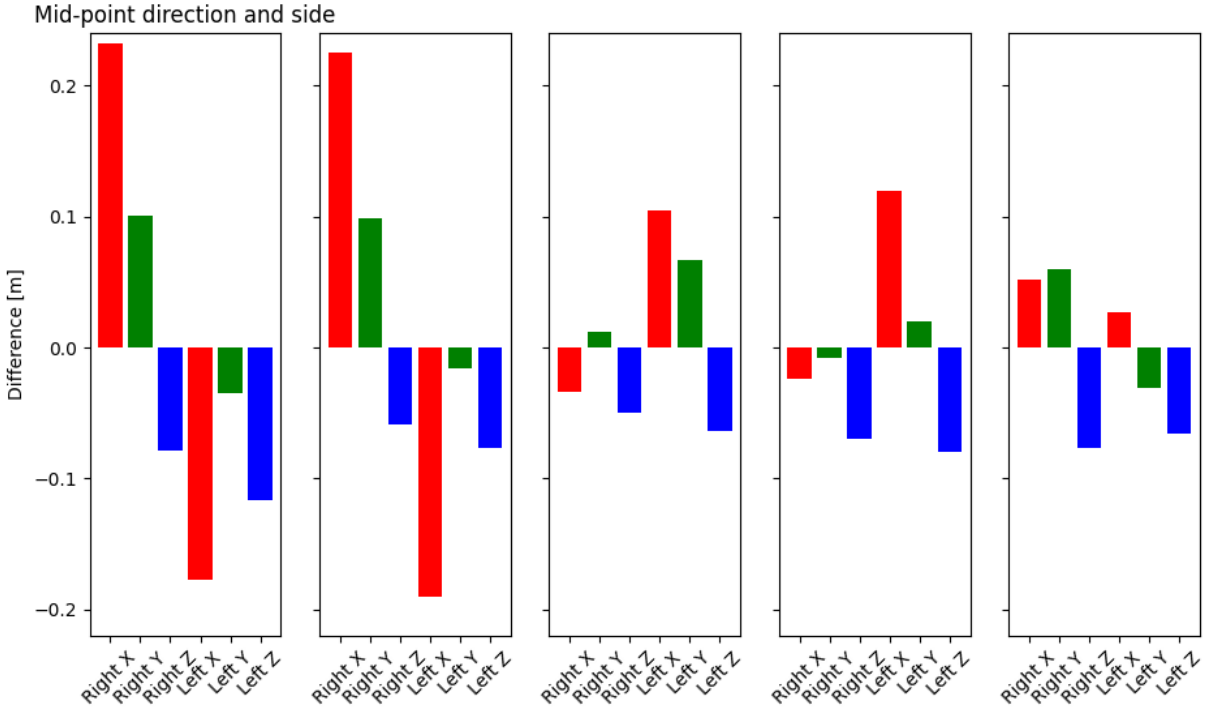

Figure 4.33: RANSAC mid-point and true plane mid-point on true plane session 2, where north-difference is given in red, east-difference in green and height difference in blue

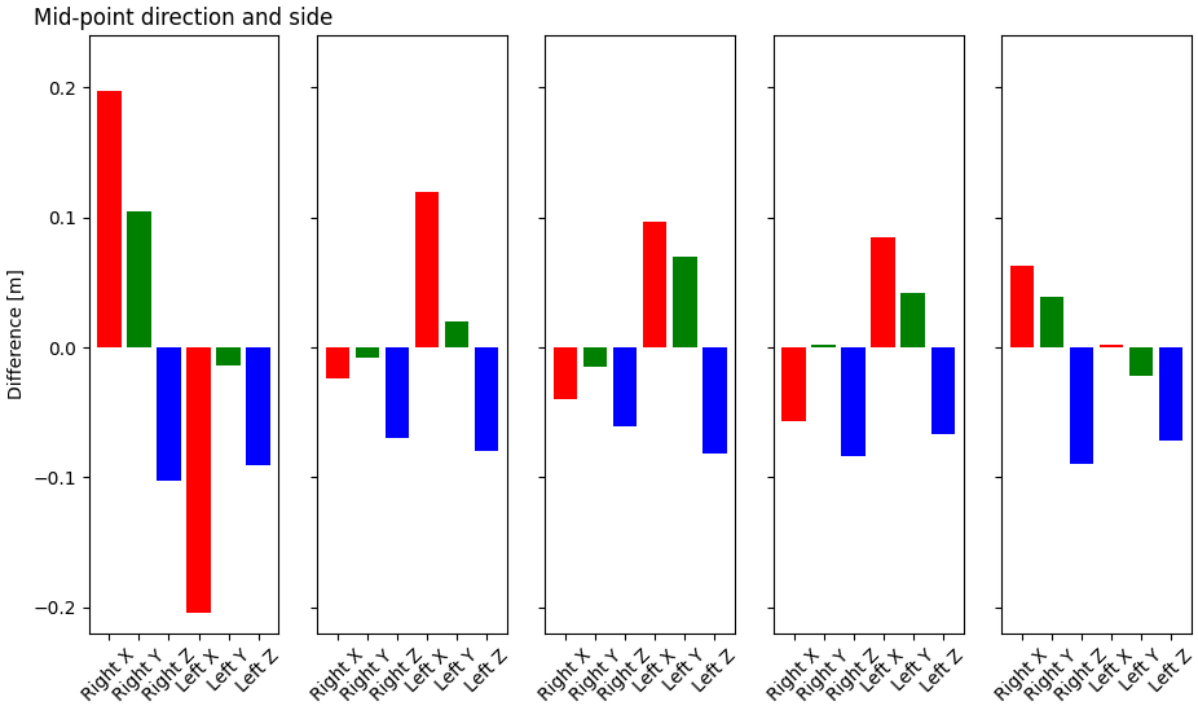

Figure 4.34: RANSAC mid-point and true plane mid-point on true plane session 3, where north-difference is given in red, east-difference in green and height difference in blue

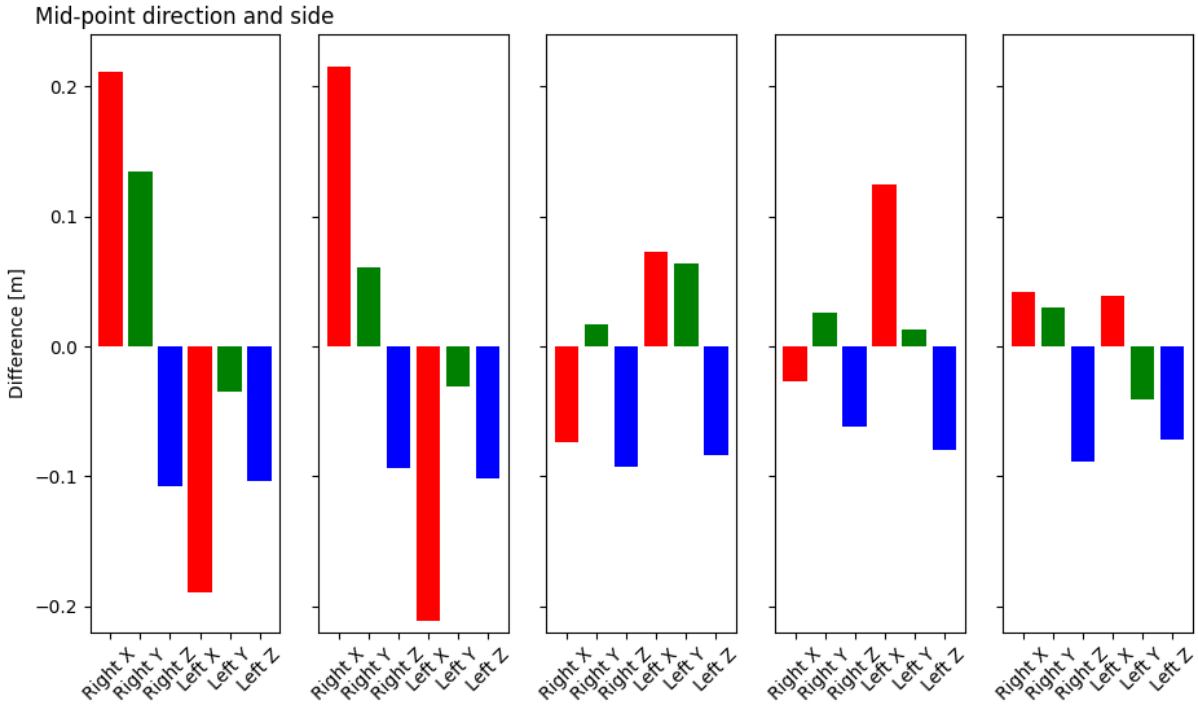

Figure 4.35: RANSAC mid-point and true plane mid-point on true plane session 8, where north-difference is given in red, east-difference in green and height difference in blue

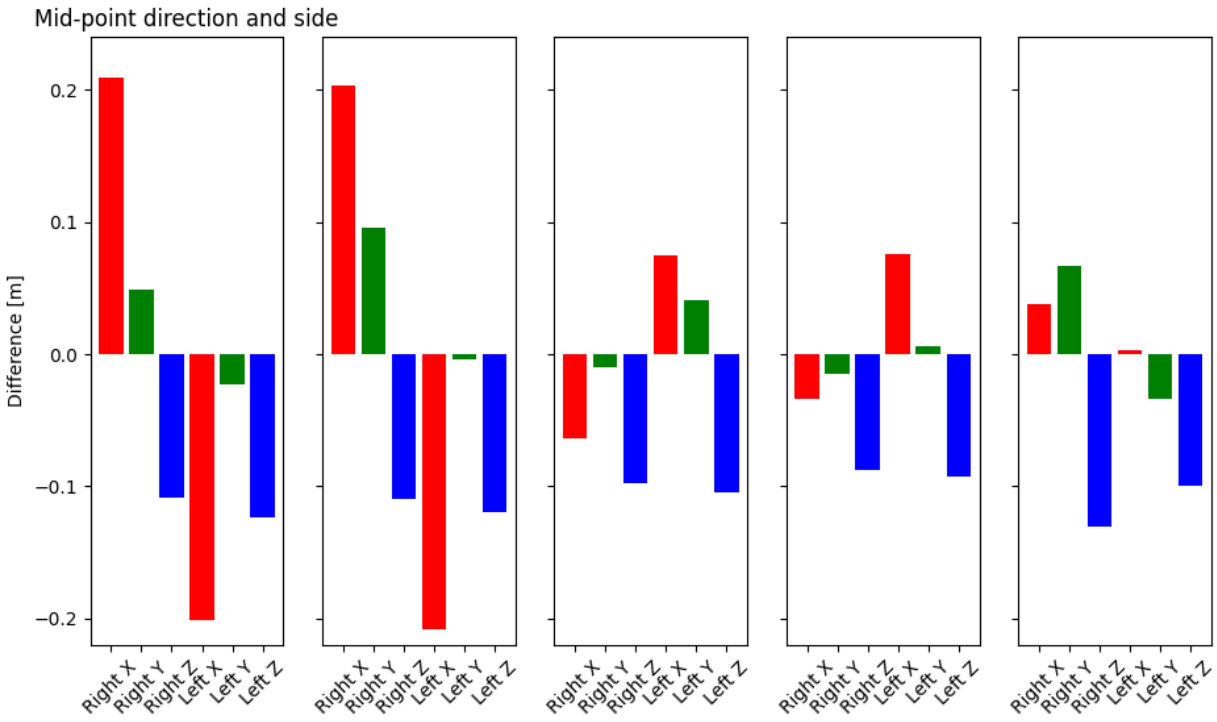

Figure 4.36: RANSAC mid-point and true plane mid-point on true plane session 9, where north-difference is given in red, east-difference in green and height difference in blue

4.3.6 Volume Comparison of Planes

The volume calculated from the boundaries of the RANSAC planes are presented in Table 4.22. The highest volume is given by the RANSAC planes is from S2 for roof model 5. The lowest volume calculated is from S8 for roof model 4. The RANSAC roof model 5 have the highest average volume of all roof models.

Table 4.22: Volume [m^3] below each roof model constructed by RANSAC inliers and the BBox boundaries at each session

Roof Model Volume [m^3] / Session	S1	S2	S3	S8	S9
1	0.012	0.014	0.010	0.007	0.016
2	0.010	0.020	0.006	0.012	0.015
3	0.013	0.017	0.015	0.017	0.020
4	0.011	0.014	0.011	0.005	0.018
5	0.026	0.030	0.022	0.025	0.022

Chapter 5

Discussion

5.1 Control Planes & Flight Conditions

The flight and true points measurement are acquired during the same day with cloudy weather conditions. These conditions are not likely to have a notable impact on the results. The temperature is within the accepted temperature of flight and RTK measurements stated by DJI and Leica in Table 4.1 and Table 4.2 [24, 52]. With over 30 satellites present, good geometry is to be expected. Conducting the experiment on a field allows for exclusion of any possibility of reflection of signals. On the other hand, the ionospheric activity during the night and early morning is measured at very high levels, and can affect the results. They are measured as moderate or low levels during daytime, but increase again after noon. The true point measurement results in 1 cm standard deviation in vertical direction, where ionospheric activity can be a contributing factor as stated by NMA [35]. The tripods are placed deep into the snow, but movement is still possible during measurements and may influence a higher standard deviation measurement after the flights. The results are given within the expected accuracy of measurement with RTK GNSS CPOS and are collected within the requirements of measuring of the Norwegian standards described by NMA [35]. They can therefore be used as true points and to construct a true plane to compare with the point cloud.

The accuracy of the roof models built is between 1-2 mm and could make a minor impact on the baseline calculation and constructed plane equations. However, the results of the true plane equations given in Table 4.6 are as expected. The coefficients a, b and c are the same for each left and right plane with a notation change. The d is expected to be close to each other, but as they refer to the origin, they will change because of the arrangement and dimensions of the roof models.

5.2 Initial Point Cloud

5.2.1 Discovered Errors in Visualisations

When the point cloud is visualised in the software *CloudCompare*, the points collected on the roof models are easy to find and observe, which is a significant benefit of using roof models as signals. When investigating the points collected on the roof models closer, the points appear as to have detected the roof, but it also seems to have collected some points right below and vertically down to the surface or tripod. This can be seen in Figure 4.11 and Figure 4.12. The colour is also misleading as it detects black or brown colours (roof model colour) further down to the snow surface. Some places the orange colour of the tripod can be seen, but very clearly blended into each other. For the extraction of the points on the collected LCP this can be a concern. If there are points that are collected on the LCP but not extracted out for further studies, it can be causing an inaccuracy to the further calculations. It is not clear how the values are referred to the true plane in *CloudCompare* and assumptions need to be confirmed by studying the point cloud and true plane together.

The point clouds collected from S4, S5, S6 and S7 with an altitude of 80 m above ground level, do not get expected points or shape of a roof model. The points look rather blended into two separate objects as seen in Figure 4.12b. The only LCP with readable points is LCP 5 for these sessions.

The amount of detected points can be seen in Table 4.8. The actual detected points on each LCP compared to expected is just over half for S1 and S2. For S3, S8 and S9 its right below half. For the sessions with and altitude of 80 m above ground level, no points are detected as roof models. These numbers confirm parts of our assumptions and hypothesis of the parameters, speed and altitude above ground level, having an impact on the results. Since the expected points are given by the DJI Terra program itself, they can be used to compare the actual amount of points. The point clouds that are collected from all sessions with an altitude of 80 m above ground level (S4, S5, S6 and S7), are not being used in further error measures. It is interesting to see that the expected amount of points are the same for S6 and S8 with two different parameters, but the actual results are very different from each other. Additionally, the amount of points on LCP 5 is a lot higher for all sessions than the other LCPs. The reasons for this could be that the LCP 5 is directly under the flown UAV-borne LiDAR and that the direction of LCP 5 has an angle and is therefore have a higher possibility of collecting the points. Compared to the other LCPs, the detection of the slope is from bottom to top according to the flight path.

The results of the amount of points collected in the point clouds aligns with the study on LiDAR workflow for detection of snow depth in the Swiss alps. The point density in steep areas is lower than what is expected [47]. The amount of points is concerning because it is

important for the level of details captured on roof model. If the roof model had more details, such as a pipe, patterns on roof, the amount of points would not be enough. However, in this project the roof models are simple and the point clouds that had enough points to detect all roof models in the same session are used in further studies.

All point clouds are divided in left and right by using the *CloudCompare* tools for extraction. Even though the tools are helping with a correct division, the method of dividing them is manual and therefore can be a cause of inaccuracies. As seen in the Figure 4.14 and Figure 4.15 the colour indicate the different sides of the extracted point clouds that are used for further error measures of the point cloud. In Figure 4.14 the blue part of the points seems to be further to the right and the magenta coloured points to the right as well. This can be an error of the described reason for inaccuracy. Another reason can be that the point cloud have an offset and do not have the same position as true plane. The separation of left and right may therefore look wrong in the visualisations. When looking in Table 4.7 the actual point on each side have a similar distribution of points. The point with the highest difference in point on each side is 29 points in S2 for LCP 2. The other point differences are more close to 10 points in difference which can be expected. Additionally, the UAV is observed to move towards north between each landing in Figure 4.5 and seen in Figure 4.13 the point cloud is clearly not in the same position. Because the points are not GPS corrected, this could be the reason for the described error. This shift is also discovered as an error for the Zenmuse L1 LiDAR scanner by [10] and by [50]. This strengthens the possibility of an offset.

5.2.2 Error Measures of Initial Point Clouds

The results from the measured height of snow surface compared to the measured height from the point cloud shows a maximum value in difference 0.289 m. All of the points given by the check are below the expected value of the surface height. Before measuring, the expected results was that the points in the point cloud were measured above the expected surface. The expected surface is measured with a metrestick with the given results in Table 4.4. The result do therefore have some inaccuracies. The snow surface changes a lot in the area and therefore makes it difficult to find the correct surface height in the point cloud. The results still give an indication of the differences between the heights of the surface that can apply to the rest of the point cloud heights.

The distribution of the points above and below each LCP for each session is given in Table 4.11. When looking at the results, most of the points are detected above the LCP. For LCP 5 most of the points where detected above, but for LCP 3 and LCP 4 more points are detected below for at least one session. As described, this can be a result of a offset of the points, since the points are not GPS corrected.

The distance of the points to the plane are being used to describe the lowest and highest

points above the true plane. This is shown in Table 4.12. The minimum and maximum values are higher than the values from the accuracy investigation in section 2.3.1 with results derived by [44]. Their values are collected from a strip and are adjusted collectively with camera images. This makes their point cloud achieve a lower error. The high median in these results is expected from the results of distribution of points above and below the true planes. More points above the plane contributes to a more positive median value and the max value is in most cases higher than the min value. However, the highest MAD value of 0.038 m which gives an indication of the variability of the points that can be compared to the MAD of the inliers for a chosen plane.

The arithmetic mean show slightly greater values in the first and last session, but none of the values show a significant difference between the sessions The LCP 5 has some higher values for three of the sessions which can be a result of it being the LCP with the most points collected. The arithmetic mean results can be compared to the result of the arithmetic mean of 0.034 m by [44] in section 2.3.1. In the first and last session with the speed 5 m/s and altitude of 40 m above ground level, the values are above, but the other values are below 0.034 m seen in Figure 4.16.

The standard deviation from the distances to the true plane is below 0.0300 m given in Figure 4.17. These values compared to 0.0342 m [44] indicate the points in the point cloud to have an higher accuracy of the distances to the true plane than originally expected. However, there is no significant difference between the sessions.

For the results of the RMSE given in Figure 4.18, the values of the first and last session have higher values. For LCP 5 the RMSE value at S1 is at 0.06 m, but the lowest values are below 0.03 m. These values compared to the 0.0356 m value given by [44], shows a bad fit. However, some of the values given are below this as well. The investigation on the accuracy of Zenmuse L1 conducted by [10] shows an accuracy value of 0.036 m in all directions with the altitude of 50 m before transformations. This is also lower than the largest value of accuracy derived from this project. There is no significant difference between the sessions.

The point cloud error measure of the initial point cloud shows no sign of significant difference when comparing the sessions with different speed parameters. These results aligns well with the study on speed parameters for UAV, but with a RGB camera instead of a LiDAR sensor [45]. Even though there is no significance, the amount of points can still give an indication on how much details it is possible to detect during each flight.

5.3 RANSAC Inlier Estimation

The amount of inliers are given in Table 4.13. Of each session, the inliers of the point cloud on LCP 5 have the most amount of points. This is expected, because the point cloud on the

LCP 5 has the most amount of points in the original point clouds. The other inlier sets are also as expected. For the distribution of the inliers above and below the true plane given in Table 4.14, there is mostly points above the plane, except from LCP 3 in S2. For this LCP in this specific session, the result seems to be having an offset and the distribution above and below the original point cloud in Table 4.11 describes the majority of points below as well. From the visualisations of the points on the true planes and Table 4.11, the number of points above and below the true planes are as expected.

The RANSAC estimated plane equations of the inliers compared to the true plane equations given in Table 4.6 differ a lot from each other. The expected values of the coefficient a is 0.218 for all of the LCPs except from LCP 5 at 0.067 which is oriented differently. The RANSAC calculated coefficient a varies from 0.053-0.267 for the first four LCPs. For LCP 5 it varies from 0.649 to 0.766. This is a large variety of a values compared to the true plane coefficients. The same tendency is seen in the other coefficient where b is expected to be 0.059 for LCP 1 and LCP 4, 0.044 for LCP 2 and LCP 3, and 0.215 for LCP 5. The coefficient b of the RANSAC equation is varying between 0.807 and 0.127 for the four first LCPs, and 0.265 and 0.148. The coefficient c is resulting in higher values of the RANSAC equation compared to the true equation of 0.266. The last constant d of the equation is expected to be between 1570664.1 and 1585671.4 for the first four equations and, 601512.4 and 601440.8 for the last equation of LCP 5. All of the results of the constant d shows a higher value. Because of the low collected amount of points lower on the plane and visualised in Figure 4.13 and Figure 4.11, the coefficients can be behaving differently than the true equation coefficients.

For better understanding the distributing of inliers on the plane equations the visualisations in Figure 4.19, Figure 4.20, Figure 4.21, Figure 4.22, and Figure 4.23 are presented. In these plots, the RANSAC planes are visualised and the inliers can be seen along the planes. For the LCP 5 the inliers seems to be more more precise of the planes recreating the roof model in each session. For session 8 with the highest speed, the lower point density is clear, but show no signs of having an impact on the ability to create the RANSAC planes. As such, the chosen threshold of 0.2 seems to be a good value for the estimations.

5.3.1 Error Measures of RANSAC Inliers

The results of the minimum and maximum values on the inliers on the true plane in Table 4.20 show a higher tendency of choosing points laying higher above the planes. This is expected according to the number of inliers found above and below the true planes in Table 4.14. The minimum value here are lower which also causes the median to be higher. For some cases there is no point below the plane and the lowest positive distance is displayed instead. Although, the fact that there are more inliers above the measures shows a closer result compared to the result from section 2.3.1. The estimations give a lower MAD value compared to the results of the initial point cloud.

The arithmetic mean of the absolute distance of the inliers to the true plane are showing similar results to the mean of the initial point clouds. There are some noticeable differences of lower values obtained for LCP 1 in each session. For S2, S3 and S9, lower or close to same values are derived in each LCP. These results can be expected because of the inliers collecting points from the point cloud closer to the true plane. For the standard deviation of the inliers, the values compared to the initial point cloud are lower or close to the same value. This is also expected because the RANSAC selects points closer to each other with a lower variability and the standard deviations are then lower. For the RMSE values of the RANSAC inliers, all values are lower or close to same. For S2 and S9 the values have noticeably improved at each LCP, but still not better than the accuracy reported by the [44] or [50]. The reason for this could be that they did not do the experiments in a steep area. The RMSE from [10] shows an accuracy of 0.040 m and 0.160 m derived in steep areas. Therefore, the results of the RMSE is expected for the case of steep areas. The GEOSFAIR project conducted by NRPA shows an accuracy of 0.052 m and 0.155 m [49]. The conclusion of the GEOSFAIR project is therefore that the values are within an acceptance of quality for further use.

With the RANSAC planes constructed from the inliers, a comparison of the angle between the true plane and the RANSAC plane is possible. The expected angle of the planes is 90°. The LCP 5, with the most points collected do not have the best achieved angle, but have a more stable angle among the different sessions than the others. The largest value is 131°. When comparing these, some of the planes do not attach to each other and the calculations of the angle are only calculated where they intersect. Therefore, the angles can give wrong results for comparison. It is interesting that the angles are varying a lot. A reason for this happening could be that the point coverage is concentrated at the top of the LCPs and therefore they do not have points long enough down on the LCP to detect a more accurate angle.

The mid-point of the inliers compared with the mid-point on the true plane describes what is seen in the Figure 4.14 and Figure 4.15, where more points are collected at the top of the true planes. This results in a reconstruction of a smaller sized plane with a higher mid-point than the mid-point on the true plane. This can be seen in Figure 4.27, Figure 4.28, Figure 4.29, Figure 4.30 and Figure 4.31. It can also be seen that for some LCPs the mid-points are moved further in north direction. The plots of the point differences in each direction are given in Figure 4.32, Figure 4.33, Figure 4.34, Figure 4.35 and Figure 4.36. The differences are as expected from the initial point cloud visualisations.

When the bounding points of each RANSAC plane is found, the points of the top boundaries with the same vertical value as the lower boundaries is used to find the volume of the RANSAC roof models. The expected volume of the roof model is 0.06 m^3, but because of the points collected only on the top of the LCP and the mid-point for all of the LCPs being very high on the LCPs, the expected volume is below half of the true plane volume. The volume of LCP 5 in S2 of 0.03 m^3 with the most collected point is the volume closest to the expected

volume. The LCP 5 has the highest volumes for each session. This can be understood as the LCP that collected the most points are able to achieve a higher volume and more collected point on the lower part of the LCP.

To find the position accuracy and ranging accuracy is difficult with the designed method and separating the measured errors is difficult. The errors seems to be caused by both factors. The movement of the point cloud is possibly cause by a systematic shift and shows position inaccuracies. The height of the points detected above the LCP can be position accuracy, but also caused by ranging error. The roughness of the points shows the ranging accuracy.

Chapter 6

Conclusions & Future Work Recommendations

This chapter summarises the thesis project based on the objectives formulated in the introduction. Additionally, future work for the project is suggested.

6.1 Summary & Conclusion

The main goal of this project is to investigate the accuracy and reliability of UAV-borne LiDAR technology in steep and snow-covered areas with the complementary hypothesis that it can effectively be used for this purpose. The objectives defined for this project in section 1.2 cover the development of a reliable protocol for assessing the quality of UAV-borne LiDAR monitoring of steep areas, to quantify the impact of the speed and altitude on the accuracy and determine the feasibility of using the designed protocol for measuring steep and snow-covered areas.

In chapter 2, a fundamental understanding of the four technologies combined in this project, UAV, UAV-borne LiDAR, point cloud data and RTK GNSS, to collect data that can be used for monitoring steep and snow-covered areas is described. After these fundamentals are presented, the SOTA RANSAC algorithm for plane fitting and related work for necessary knowledge for designing the experiment and determining the feasibility of the protocol is presented.

The designed experiment of assessing the quality of point cloud data is presented in chapter 3. The suggested roof models for emulating steep areas are used as control planes. Further, various speed and altitude parameters are assigned to the nine flight sessions for point data acquisition. Additional to the design of experiment, the principals of arrangement of roof models are constructed. Lastly, the data analysis of the quality of the point cloud data is

investigated and RANSAC fitted planes are compared to control planes.

The experiment is conducted at NTNU Dragvoll with five LCPs arranged on a field with snow surface. True points of the LCPs and point clouds from the flight sessions are collected and the quality analysed. In chapter 4 the results from the experiment and point cloud analysis are presented. Calculations of median and MAD of the distances above and below the constructed true plane are highlighted as well as the mean, standard deviation and RMSE of the absolute distances. These calculations are given for the initial point cloud and the RANSAC inliers of the point cloud. Further, the angle, mid-point and volume of the RANSAC fitted planes of the inliers are presented.

To determine the feasibility of the designed protocol, the experimental results are discussed in chapter 5. The assessment of steep areas by using LCPs enables an analysis of the accuracy, but lack of points makes it difficult to give a full investigation. The LCPs not being covered completely raises concerns on the arrangement of the roof models according to the flight path of the UAV.

The speed parameter of the UAV shows no significance in the error measures, but the amount of points actually detected indicates the level of details achievable from the flight. The altitude of 80 m above ground level has a surprisingly low possibility of detecting objects compared to the expected amount of points detected. The amount of points are almost not existent on the LCPs and are not usable for further studies because the roof sides could not be recognised. The amount of points detected is highly affected by both parameters and higher speed or altitude decrease the level of detection.

The hypothesis is confirmed and a protocol for assessing quality of UAV-borne laser scanning for steep and snow-covered areas is achieved. Given the values of related project within the research of GEOSFAIR, the error is right below the accepted RMSE for all sessions. Therefore, the protocol may be suitable for the purpose of avalanche monitoring. Even though the values can be accepted, it is also important to consider the exact use of the data. If a higher accuracy is required, the UAV-borne LiDAR cannot meet the requirements with the designed approach for this thesis.

6.2 Recommendations for Future Work

In this final section, four recommendations for future work are presented.

Various Principals of Arrangement of Roof Models

After comparing the amount of points collected on LCP 5 compared to the other LCPs, where more points are collected on LCP 5, the designed arrangement of LCPs should be tested for more than one approach. The collected point difference could be caused by the directed

angle of roof ridges, where LCP 5 has a 45° angle and is directly placed below the flight path. This could have enabled more points to be collected on LCP 5 than the others. By changing the direction of the flight path and approaching the LCPs from different directions, this assumption can be assessed.

In [44] the roof models collected more points from flights with more stripes and overlaps between the stripes. This increases the amount of points collected on the roof models and enables error measures on a greater scale.

Improving Extraction of Point Cloud Data for Plane Fitting

The extraction of the collected point on the roof models and the divided points in left and right side of the roof model, is done manually in CloudCompare. This may cause inaccuracies in further calculations of inliers and construction of planes. Therefore, using an automatic approach or algorithm with a higher probability of consistent separation for this extraction would be beneficial.

Various Altitude and Steep Angle of Flight

Since the parameter, altitude of 80 m above ground level, does not result in enough point collection for investigation of quality further in the data analysis, the data acquisition should be tested for various height parameters below 80 m. Alternatively, the LCPs can have a greater area than the one chosen for this experiment. Although, the area of the LCP will be less portable with greater dimensions, therefore limiting the flexibility of the experiment.

Additionally, the slope of the LCP is 45°, but the slope could have been tested with a lower value, such as one of the experiments done by GEOSFAIR at 20° to 22°, to find out if the angle is the reason for the low collection of points [49].

Snow Effect on Quality of Point Cloud Data

When designing the experiment, test with snow on top of the roof models have been considered. However, predicting weather is difficult and the importance of doing the same measurement with and without snow, is difficult to achieve during one experimental day. Although, for further studies, this is highly recommended. Comparing the error measures with roof models with a snow layer on top would enable a full investigation on the snow effect on the quality of the point cloud data.

Bibliography

[1] Nathan L. Schomer and Julie A. Adams. 'Unmanned Aerial Vehicle Usage and Affordability Among Mountain Search and Rescue Teams'. In: *2022 IEEE International Symposium on Safety, Security, and Rescue Robotics (SSRR)* (2022), pp. 61–66.

[2] G. Pradeep Kumar and B. Sridevi. 'Chapter 6 - Development of Efficient Swarm Intelligence Algorithm for Simulating Two-Dimensional Orthomosaic for Terrain Mapping Using Cooperative Unmanned Aerial Vehicles'. In: *The Cognitive Approach in Cloud Computing and Internet of Things Technologies for Surveillance Tracking Systems*. Ed. by Dinesh Peter et al. Intelligent Data-Centric Systems. Academic Press, 2020, pp. 75–93. ISBN: 978-0-12-816385-6. DOI: https://doi.org/10.1016/B978-0-12-816385-6.00006-4. URL: https://www.sciencedirect.com/science/article/pii/B9780128163856000064.

[3] Mithra Sivakumar and Naga Malleswari Tyj. 'A Literature Survey of Unmanned Aerial Vehicle Usage for Civil Applications'. In: *Journal of Aerospace Technology and Management* (2021).

[4] Daniele Giordan et al. 'The use of unmanned aerial vehicles (UAVs) for engineering geology applications'. In: *Bulletin of Engineering Geology and the Environment* 79.7 (Sept. 2020), pp. 3437–3481. ISSN: 1435-9537. DOI: 10.1007/s10064-020-01766-2. URL: https://doi.org/10.1007/s10064-020-01766-2.

[5] Luísa Gomes Pereira et al. 'Quality Control of Outsourced LiDAR Data Acquired with a UAV: A Case Study'. In: *Remote Sensing* 13.3 (2021). ISSN: 2072-4292. DOI: 10.3390/rs13030419. URL: https://www.mdpi.com/2072-4292/13/3/419.

[6] Nader Mohamed et al. 'Unmanned aerial vehicles applications in future smart cities'. In: *Technological Forecasting and Social Change* 153 (2020), p. 119293. ISSN: 0040-1625. DOI: https://doi.org/10.1016/j.techfore.2018.05.004. URL: https://www.sciencedirect.com/science/article/pii/S0040162517314968.

[7] MA Xin et al. 'A Design Method of UAV Flight Protection Area Based on the Statistical Analysis of Flight Path Deviation'. In: *IOP Conference Series: Materials Science and Engineering* 1043.4 (Jan. 2021), p. 042039. DOI: 10.1088/1757-899X/1043/4/042039. URL: https://dx.doi.org/10.1088/1757-899X/1043/4/042039.

[8] Baochang Zhang et al. 'Geometric Reinforcement Learning for Path Planning of UAVs'. In: *Journal of Intelligent & Robotic Systems* 77.2 (Feb. 2015), pp. 391–409. ISSN: 1573-0409. DOI: 10.1007/s10846-013-9901-z. URL: https://doi.org/10.1007/s10846-013-9901-z.

[9] Juha Hyyppä; et al. *The SAGE Handbook of Remote Sensing*. The SAGE Handbook of Remote Sensing. 55 City Road, May 2009. DOI: 10.4135/9780857021052. URL: https://methods.sagepub.com/book/the-sage-handbook-of-remote-sensing.

[10] Martin Troner, Rudolf Urban and Lenka Linkova. 'A New Method for UAV Lidar Precision Testing Used for the Evaluation of an Affordable DJI ZENMUSE L1 Scanner'. In: *Remote. Sens.* 13 (2021), p. 4811.

[11] DJI Enterprise. *LiDAR Drone Systems: Using LiDAR Equipped UAVs*. [Accessed 16-May-2023]. 2022. URL: https://enterprise-insights.dji.com/blog/lidar-equipped-uavs.

[12] C-Cj Lyu, Norbert H. Maerz and Kenneth J. Boyko. 'Terrestrial LiDAR system accuracy investigation for slow-moving landslide deformation'. In: *Journal of Applied Remote Sensing* 15 (2021), pp. 044510 –044510.

[13] Tianyu Gao et al. 'Effects of temperature environment on ranging accuracy of lidar'. In: *International Conference on Digital Image Processing*. 2018.

[14] Reason Mlambo, Iain Hector Woodhouse and Karen Anderson. 'Structure from Motion (SfM) Photogrammetry with Drone Data: A Low Cost Method for Monitoring Greenhouse Gas Emissions from Forests in Developing Countries'. In: *Forests* 8 (2017), p. 68.

[15] Bikram Pratap Banerjee and Simitkumar Anuray Raval. 'Mapping Sensitive Vegetation Communities in Mining Eco-space using UAV-LiDAR'. In: *International Journal of Coal Science & Technology* 9 (2022).

[16] Ana Sánchez Rodríguez et al. '9 - Laser scanning and its applications to damage detection and monitoring in masonry structures'. In: *Long-term Performance and Durability of Masonry Structures*. Ed. by Bahman Ghiassi and Paulo B. Lourenço. Woodhead Publishing Series in Civil and Structural Engineering. Woodhead Publishing, 2019, pp. 265–285. ISBN: 978-0-08-102110-1. DOI: https://doi.org/10.1016/B978-0-08-102110-1.00009-1. URL: https://www.sciencedirect.com/science/article/pii/B9780081021101000091.

[17] Sarvesh Kumar Singh, Simit Raval and Bikram Banerjee. 'A robust approach to identify roof bolts in 3D point cloud data captured from a mobile laser scanner'. In: *International Journal of Mining Science and Technology* 31.2 (2021), pp. 303–312. ISSN: 2095-2686. DOI: https://doi.org/10.1016/j.ijmst.2021.01.001. URL: https://www.sciencedirect.com/science/article/pii/S2095268621000070.

[18] Giuseppe Valenzise et al. 'Chapter 13 - Point cloud compression'. In: *Immersive Video Technologies*. Ed. by Giuseppe Valenzise et al. Academic Press, 2023, pp. 357–385. ISBN: 978-0-323-91755-1. DOI: https://doi.org/10.1016/B978-0-32-391755-1.00019-5. URL: https://www.sciencedirect.com/science/article/pii/B9780323917551000195.

[19] Max Joseph and Leah Wasser. *Introduction to lidar point cloud data - active remote sensing*. Feb. 2017. URL: https://www.earthdatascience.org/courses/earth-analytics/lidar-raster-data-r/explore-lidar-point-clouds-plasio/.

[20] Xu Liu et al. 'Point Cloud Intensity Correction for 2D LiDAR Mobile Laser Scanning'. In: *Wireless Communications and Mobile Computing* 2022 (Jan. 2022), p. 3707985. ISSN: 1530-8669. DOI: 10.1155/2022/3707985. URL: https://doi.org/10.1155/2022/3707985.

[21] Rui Gao et al. 'Reflective Noise Filtering of Large-Scale Point Cloud Using Transformer'. In: *Remote Sensing* 14.3 (2022). ISSN: 2072-4292. DOI: 10.3390/rs14030577. URL: https://www.mdpi.com/2072-4292/14/3/577.

[22] Mihaela Triglav Cekada, Fabio Crosilla and Mojca Fras. 'Theoretical LiDAR point density for topographic mapping in the largest scales'. In: *Geodetski Vestnik* 54 (Jan. 2010), pp. 403–416. DOI: 10.15292/geodetski-vestnik.2010.03.389-402.

[23] Karel Kuželka, Martin Slavík and Peter Surový. 'Very High Density Point Clouds from UAV Laser Scanning for Automatic Tree Stem Detection and Direct Diameter Measurement'. In: *Remote Sensing* 12.8 (2020). ISSN: 2072-4292. DOI: 10.3390/rs12081236. URL: https://www.mdpi.com/2072-4292/12/8/1236.

[24] DJI Enterprise. *LiDAR Drone Systems: Using LiDAR Equipped UAVs*. [Accessed 18-May-2023]. 2022. URL: https://enterprise.dji.com/zenmuse-l1/specs.

[25] Ana Paula Dalla Corte et al. 'Applying High-Resolution UAV-LiDAR and Quantitative Structure Modelling for Estimating Tree Attributes in a Crop-Livestock-Forest System'. In: *Land* (2022).

[26] Levent Candan and Elif Kaçar. 'REAL-TIME 3D POINT CLOUD MAPPING WITH UAV LIDAR'. In: *International Symposium on Applied Geoinformatics 2021* (2023).

[27] Shiyu Xiang and Dawei Li. 'Research on Plant Growth Tracking Based on Point Cloud Segmentation and Registration'. In: *2022 International Conference on Image Processing, Computer Vision and Machine Learning (ICICML)* (2022), pp. 469–478.

[28] Iris de Gélis, Sébastien Lefèvre and Thomas Corpetti. '3D URBAN CHANGE DETECTION WITH POINT CLOUD SIAMESE NETWORKS'. In: 2021.

[29] Marco Fiorucci, Peter Naylor and Makoto Yamada. 'Optimal Transport for Change Detection on LiDAR Point Clouds'. In: *ArXiv* abs/2302.07025 (2023).

[30] Mesrop Andriasyan et al. 'From Point Cloud Data to Building Information Modelling: An Automatic Parametric Workflow for Heritage'. In: *Remote Sensing* 12.7 (2020). ISSN: 2072-4292. DOI: 10.3390/rs12071094. URL: https://www.mdpi.com/2072-4292/12/7/1094.

[31] Ahmed El-Rabbany. *Introduction to GPS*. 2nd ed. Norwood, MA: Artech House, Oct. 2006, pp. 77–78.

[32] Geonorge. *Standard for geografisk informasjon: Produksjon av basis geodata 2.0*. Apr. 2023. URL: https://sosi.geonorge.no/Standarder/Produksjon_av_Basis_geodata/2.0/#_kontroll_av_h\%C3\%B8yden\%C3\%B8yaktighet.

[33] Julián Tomaštík et al. 'UAV RTK/PPK Method—An Optimal Solution for Mapping Inaccessible Forested Areas?' In: *Remote Sensing* 11.6 (2019). ISSN: 2072-4292. DOI: 10.3390/rs11060721. URL: https://www.mdpi.com/2072-4292/11/6/721.

[34] Heinz-Jürgen Przybilla and Manfred Baeumker. 'RTK and PPK: GNSS-Technologies for direct georeferencing of UAV image flights'. In: May 2020.

[35] Kartverket. *Guide to CPOS*. July 2021. URL: https://www.kartverket.no/en/on-land/posisjon/guide-to-cpos.

[36] M. Hossein Pouraghdam et al. 'BUILDING FLOOR PLAN RECONSTRUCTION FROM SLAM-BASED POINT CLOUD USING RANSAC ALGORITHM'. In: *The International Archives of the Photogrammetry, Remote Sensing and Spatial Information Sciences* (2019).

[37] Yongbin Lim, T. Ogawa and Yoichiro Hori. 'DETECTION OF RESTORATION WORK BY APPLYING THE RANSAC ALGORITHM TO THE POINT CLOUD DATA FROM LASER SCANNING: CASE STUDY AT OSTIA'. In: *The International Archives of the Photogrammetry, Remote Sensing and Spatial Information Sciences* (2022).

[38] Chao-Chung Peng. 'K-means based RANSAC Algorithm for ICP Registration of 3D Point Cloud with Dense Outliers'. In: *2021 IEEE International Conference on Consumer Electronics-Taiwan (ICCE-TW)* (2021), pp. 1–2.

[39] Rahul Raguram, Jan-Michael Frahm and Marc Pollefeys. 'A Comparative Analysis of RANSAC Techniques Leading to Adaptive Real-Time Random Sample Consensus'. In: vol. 5303. Oct. 2008, pp. 500–513. ISBN: 978-3-540-88685-3. DOI: 10.1007/978-3-540-88688-4_37.

[40] AJith RaJ. *3D RANSAC algorithm for LIDAR PCD segmentation*. June 2020. URL: https://medium.com/@ajithraj_gangadharan/3d-ransac-algorithm-for-lidar-pcd-segmentation-315d2a51351.

[41] Jyoti Madake et al. 'Visualization of 3D Point Clouds for Vehicle Detection Based on LiDAR and Camera Fusion'. In: *2022 OITS International Conference on Information Technology (OCIT)* (2022), pp. 594–598.

[42] Ren yon Guo et al. 'Perception for Coupler Rod of Freight Train Based on Image and Point Clouds'. In: *2022 China Automation Congress (CAC)* (2022), pp. 3262–3267.

[43] Open3D. *Open3d.geometry.orientedboundingbox¶*. 2023. URL: http://www.open3d.org/docs/release/python_api/open3d.geometry.OrientedBoundingBox.html.

[44] Norbert Haala et al. 'Hybrid georeferencing of images and LiDAR data for UAV-based point cloud collection at millimetre accuracy'. In: *ISPRS Open Journal of Photogrammetry and Remote Sensing* (2022).

[45] Oktawia Lewicka, Mariusz Specht and Cezary Specht. 'Assessment of the Steering Precision of a UAV along the Flight Profiles Using a GNSS RTK Receiver'. In: *Remote Sensing* 14.23 (2022). ISSN: 2072-4292. DOI: 10.3390/rs14236127. URL: https://www.mdpi.com/2072-4292/14/23/6127.

[46] Roberta Pellicani et al. 'UAV and Airborne LiDAR Data for Interpreting Kinematic Evolution of Landslide Movements: The Case Study of the Montescaglioso Landslide (Southern Italy)'. In: *Geosciences* (2019).

[47] Kalliopi Koutantou, Giulia Mazzotti and Philip Brunner. 'UAV-BASED LIDAR HIGH-RESOLUTION SNOW DEPTH MAPPING IN THE SWISS ALPS: COMPARING FLAT AND STEEP FORESTS'. In: *The International Archives of the Photogrammetry, Remote Sensing and Spatial Information Sciences* (2021).

[48] Tore Humstad et al. 'Lidar on UAS to support avalanche monitoring'. In: (May 2022).

[49] Tore Humstad. 'Field test of UAS to support avalanche monitoring'. In: (Dec. 2022).

[50] Desta Ekaso, Francesco Nex and Norman Kerle. 'Accuracy assessment of real-time kinematics (RTK) measurements on unmanned aerial vehicles (UAV) for direct georeferencing'. In: *Geo-spatial Information Science* 23.2 (2020), pp. 165–181. DOI: 10.1080/10095020.2019.1710437. eprint: https://doi.org/10.1080/10095020.2019.1710437. URL: https://doi.org/10.1080/10095020.2019.1710437.

[51] Michael Corral. 2021. URL: https://open.umn.edu/opentextbooks/textbooks/91.

[52] Geosystems Leica. *Leica Viva GS16 - Leica Geosystems*. 2023. URL: https://leica-geosystems.com/-/media/files/leicageosystems/products/datasheets/leica_viva_gs16_ds.ashx?la=en&hash=EB1C7278B6E75F4ADDF9E80849879557.

Appendix A

Leica GS16 RTK GNSS Positions

05	**Poit code**	North	East	Orthometric height		
47	Vxx	Vyy	Vzz	Vxy	Vxz	Vyz
46	**Date**	**UTC time**	**GPS**	**PDOP**		
05	**1**	7031705.396	573721.812	157.786		
47	0.00002066	0.00001121	0.00012580	0.00000667	0.00002362	0.00001399
46	**24032023**	**10:06:37**	**0.000**	**96**		
05	**2**	7031731.112	573725.857	158.231		
47	0.00001447	0.00000600	0.00007578	0.00000402	0.00001470	0.00000497
46	**24032023**	**10:08:05**	**0.000**	**96**		
05	**3**	7031733.719	573712.887	158.231		
47	0.00002430	0.00001012	0.00012655	0.00000681	0.00002458	0.00000826
46	**24032023**	**10:09:16**	**0.000**	**96**		
05	**4**	7031708.915	573709.077	157.662		
47	0.00001422	0.00000564	0.00006885	0.00000392	0.00001408	0.00000479
46	**24032023**	**10:10:31**	**0.000**	**96**		
05	**5**	7031720.155	573717.140	157.998		
47	0.00002869	0.00001211	0.00014624	0.00000823	0.00002846	0.00000949
46	**24032023**	**10:12:24**	**0.000**	**96**		
05	**1**	7031705.418	573721.800	157.804		
47	0.00001984	0.00000930	0.00010732	0.00000484	0.00001875	0.00000836
46	**24032023**	**10:13:58**	**0.000**	**96**		
05	**2**	7031731.108	573725.855	158.221		
47	0.00002756	0.00001295	0.00014756	0.00000677	0.00002589	0.00001170
46	**24032023**	**10:14:57**	**0.000**	**96**		
05	**3**	7031733.715	573712.888	158.241		
47	0.00002124	0.00001000	0.00011253	0.00000524	0.00001982	0.00000907
46	**24032023**	**10:15:58**	**0.000**	**96**		
05	**4**	7031708.902	573709.076	157.663		
47	0.00002176	0.00000770	0.00005707	-0.00000090	0.00001131	0.00000627
46	**24032023**	**10:17:05**	**0.000**	**96**		

05	**5**	7031720.157	573717.148	158.019		
47	0.00001547	0.00000731	0.00008019	0.00000385	0.00001421	0.00000664
46	**24032023**	**10:18:04**	**0.000**	**96**		
05	**1**	7031705.416	573721.787	157.817		
47	0.00002176	0.00000770	0.00005707	-0.00000090	0.00001131	0.00000627
46	**24032023**	**12:41:22**	**0.000**	**96**		
05	**2**	7031731.118	573725.855	158.200		
47	0.00002416	0.00000980	0.00007173	-0.00000056	0.00001216	0.00000916
46	**24032023**	**12:42:31**	**0.000**	**96**		
05	**3**	7031733.724	573712.895	158.245		
47	0.00004733	0.00001528	0.00010192	-0.00000803	0.00001146	0.00001446
46	**24032023**	**12:43:13**	**0.000**	**96**		
05	**4**	7031708.929	573709.077	157.732		
47	0.00003874	0.00001399	0.00010772	-0.00000081	0.00001939	0.00001260
46	**24032023**	**12:44:07**	**0.000**	**96**		
05	**5**	7031720.157	573717.137	158.032		
47	0.00003210	0.00001088	0.00009045	-0.00000103	0.00001340	0.00001124
46	**24032023**	**12:44:50**	**0.000**	**96**		
05	**5**	7031720.160	573717.133	158.049		
47	0.00005579	0.00001794	0.00013504	-0.00000196	0.00002463	0.00001628
46	**24032023**	**12:45:46**	**0.000**	**96**		
05	**1**	7031705.423	573721.785	157.808		
47	0.00002648	0.00000857	0.00006490	-0.00000094	0.00001160	0.00000786
46	**24032023**	**12:46:35**	**0.000**	**96**		
05	**2**	7031731.109	573725.851	158.242		
47	0.00003932	0.00001353	0.00010278	-0.00000128	0.00001740	0.00001377
46	**24032023**	**12:47:39**	**0.000**	**96**		
05	**3**	7031733.724	573712.894	158.240		
47	0.00003231	0.00001180	0.00009752	-0.00000094	0.00001586	0.00001325
46	**24032023**	**12:48:34**	**0.000**	**96**		
05	**4**	7031708.916	573709.082	157.686		
47	0.00003513	0.00001343	0.00009741	0.00000120	0.00001789	0.00001627
46	**24032023**	**12:49:30**	**0.000**	**96**		
05	**5**	7031720.164	573717.148	158.043		
47	0.00003721	0.00001316	0.00010344	-0.00000112	0.00001754	0.00001347
46	**24032023**	**12:50:13**	**0.000**	**96**		
05	G24T0162	7031952.886	571469.029	131.390		
47	0.00003287	0.00001410	0.00012938	0.00000098	0.00002523	0.00001603
46	**24032023**	**13:17:52**	**0.000**	**96**		

Table A.0: Results from Leica GS16 RTK GNSS positions of tripods

Appendix B

Points on LCP

Point number	Coordinates		Height [NN2000]
	North	East	
1	7031705.418	573721.796	158.068
2	7031731.113	573725.855	158.485
3	7031733.718	573712.890	158.502
4	7031708.915	573709.078	157.944
5	7031720.160	573717.143	158.290
11	7031705.039	573722.107	157.785
12	7031705.251	573721.335	157.785
13	7031705.797	573721.485	157.785
14	7031705.585	573722.257	157.785
15	7031705.312	573722.182	158.068
16	7031705.524	573721.410	158.068
17	7031705.282	573721.758	157.927
18	7031705.554	573721.834	157.927
21	7031730.757	573726.191	158.202
22	7031730.914	573725.407	158.202
23	7031731.469	573725.519	158.202
24	7031731.312	573726.303	158.202
25	7031731.034	573726.247	158.485
26	7031731.192	573725.463	158.485
27	7031730.974	573725.827	158.344
28	7031731.252	573725.883	158.344

31	7031734.074	573712.554	158.219
32	7031733.917	573713.338	158.219
33	7031733.362	573713.226	158.219
34	7031733.519	573712.442	158.219
35	7031733.797	573712.498	158.502
36	7031733.639	573713.282	158.502
37	7031733.857	573712.918	158.361
38	7031733.579	573712.862	158.361
41	7031709.294	573708.767	157.661
42	7031709.082	573709.539	157.661
43	7031708.536	573709.389	157.661
44	7031708.748	573708.617	157.661
45	7031709.021	573708.692	157.944
46	7031708.809	573709.464	157.944
47	7031709.051	573709.116	157.803
48	7031708.779	573709.040	157.803
51	7031719.694	573716.993	158.007
52	7031720.457	573716.753	158.007
53	7031720.626	573717.293	158.007
54	7031719.863	573717.533	158.007
55	7031719.778	573717.263	158.290
56	7031720.542	573717.023	158.290
57	7031720.118	573717.008	158.149
58	7031720.202	573717.278	158.149

Table B.0: Result of true points in EUREF89 UTM32 NN2000 from baseline calculations

Appendix C

Visualisation of Point Cloud & True Planes

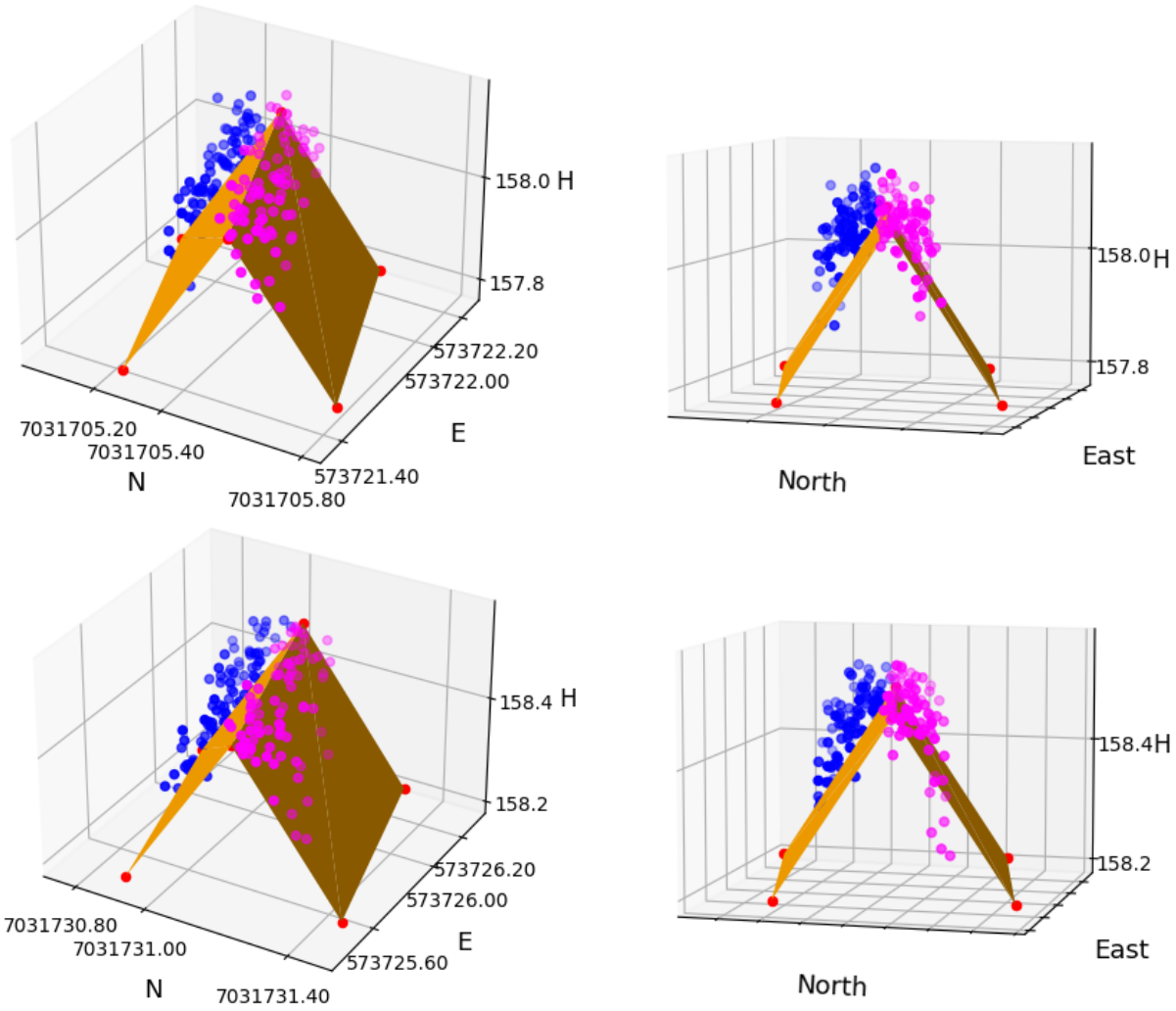

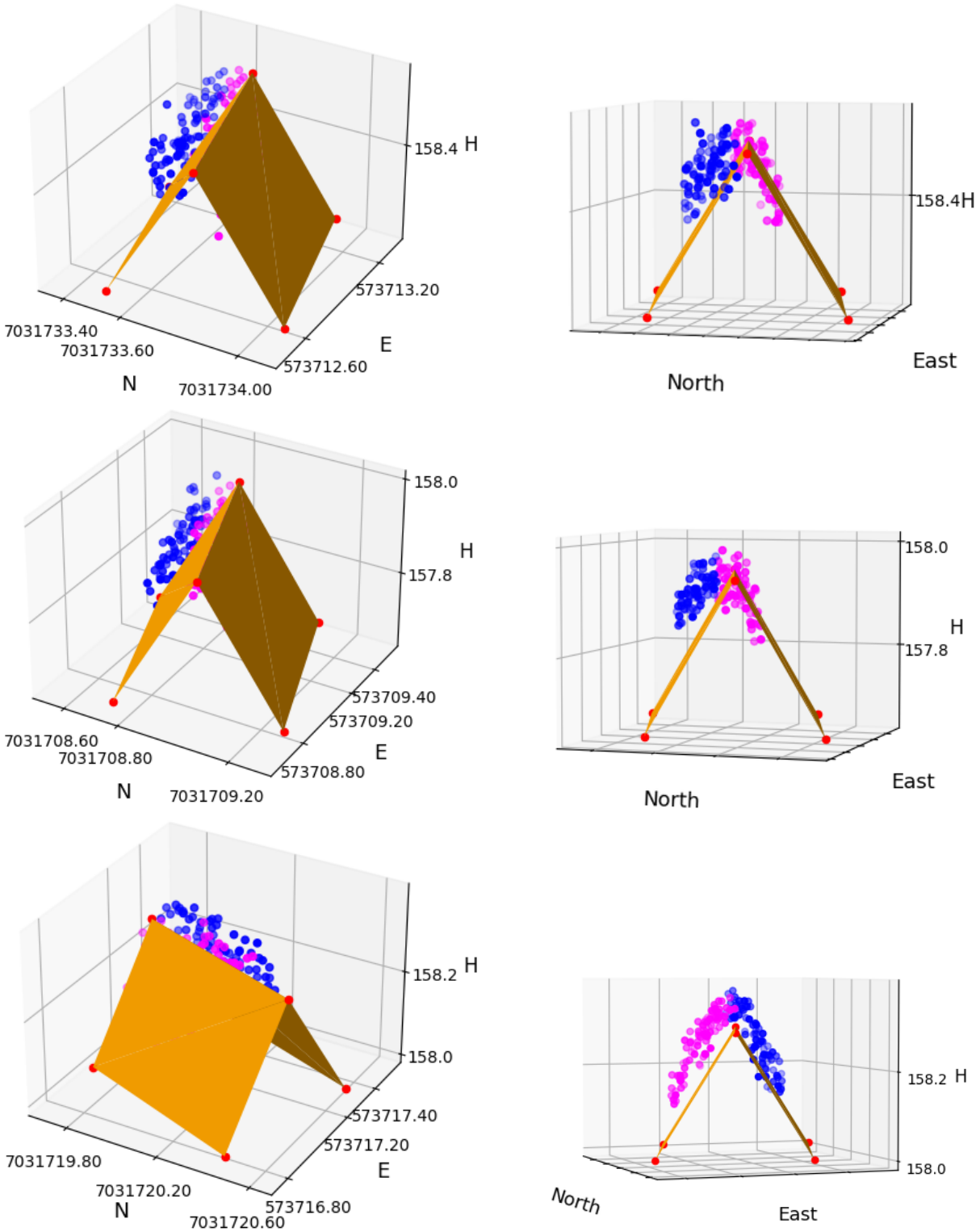

Figure C.1: Extracted point cloud from LCPs in the ascending order in S1 from two different angles divided in blue and magenta colour for each side of the true plane. The red points are the true points on the true plane

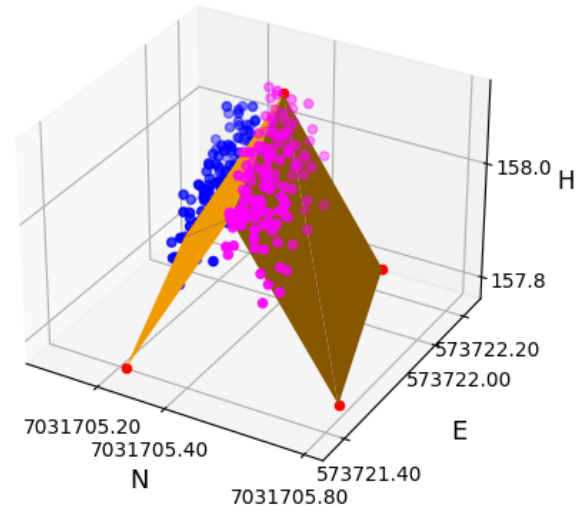
158.0
H
157.8
573722.20
573722.00
E
573721.40
7031705.20
7031705.40
N
7031705.80

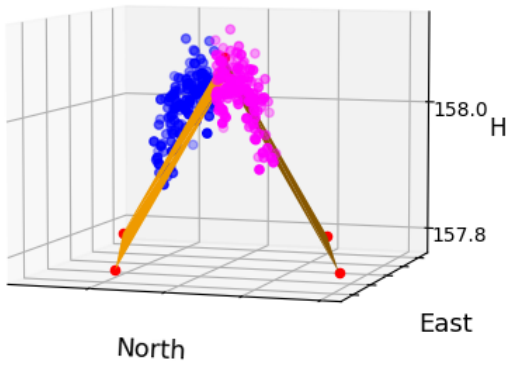
158.0
H
157.8
East
North

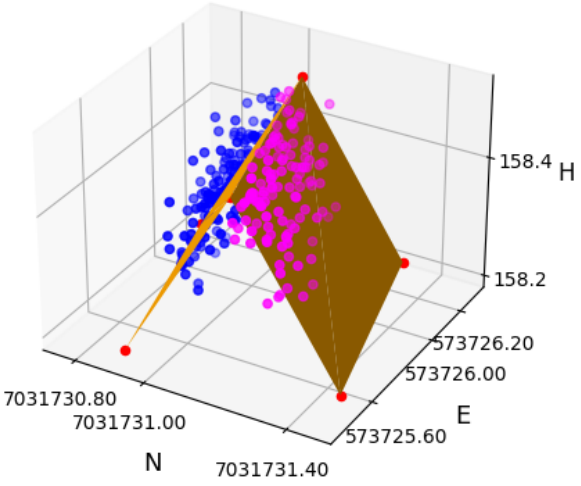
158.4
H
158.2
573726.20
573726.00
E
573725.60
7031730.80
7031731.00
N
7031731.40

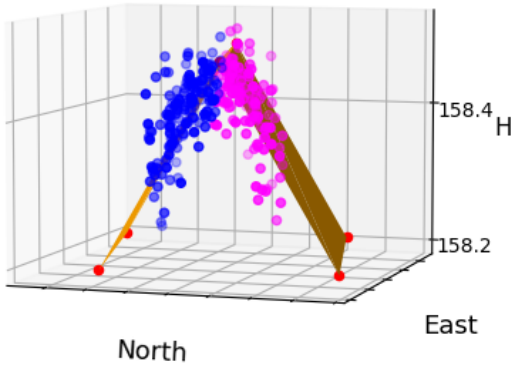
158.4
H
158.2
East
North

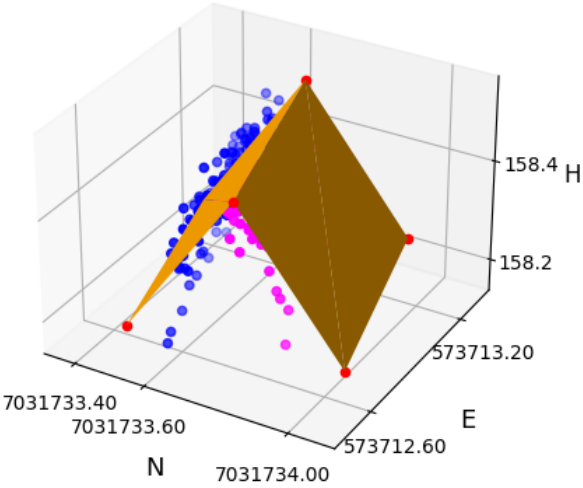
158.4
H
158.2
573713.20
E
573712.60
7031733.40
7031733.60
N
7031734.00

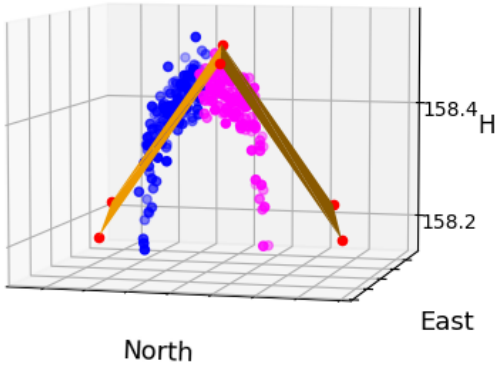
158.4
H
158.2
East
North

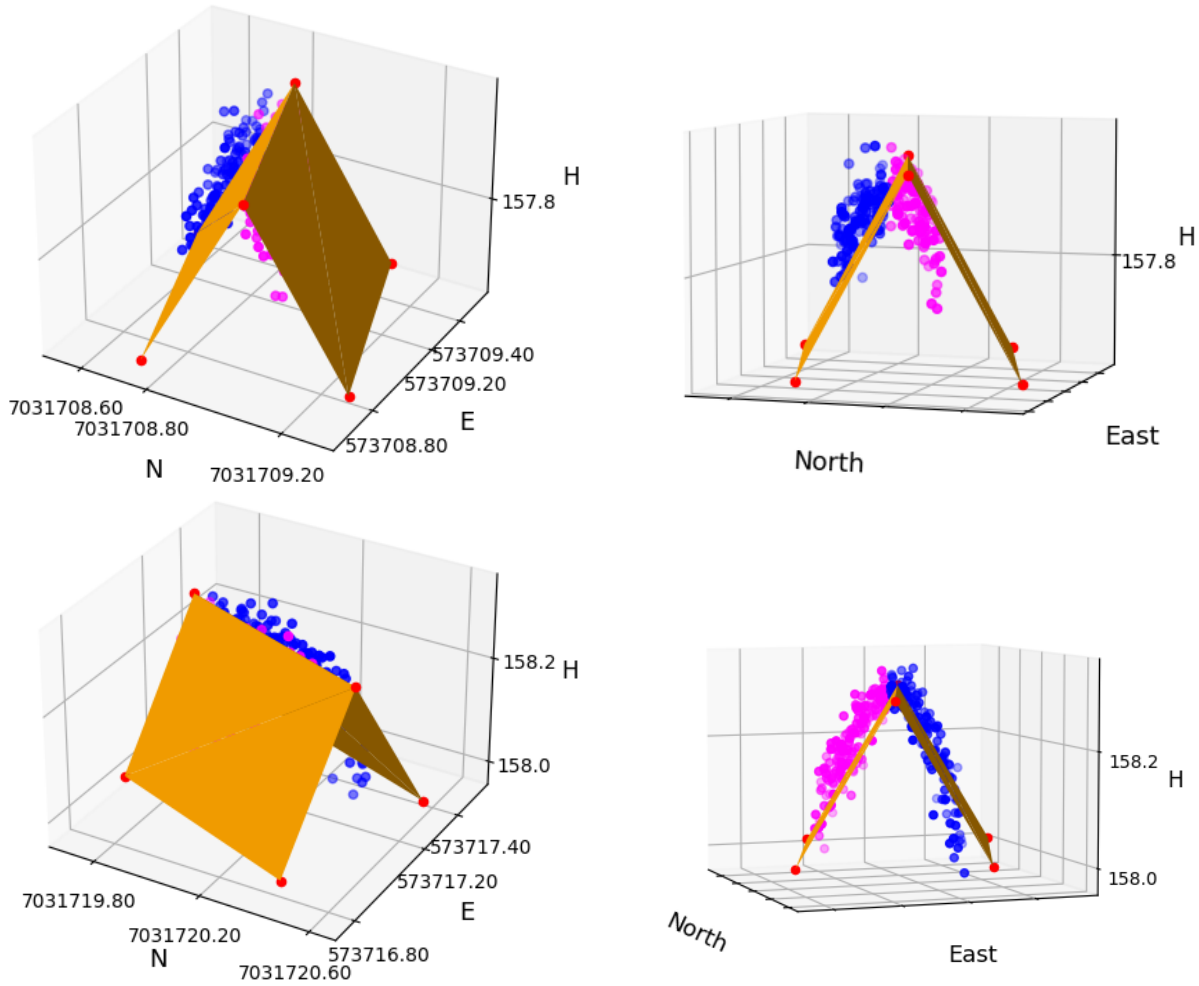

Figure C.2: Extracted point cloud from LCPs in the ascending order in S2 form two different angles divided in blue and magenta colour for each side of the true plane. The red points are the true points on the true plane

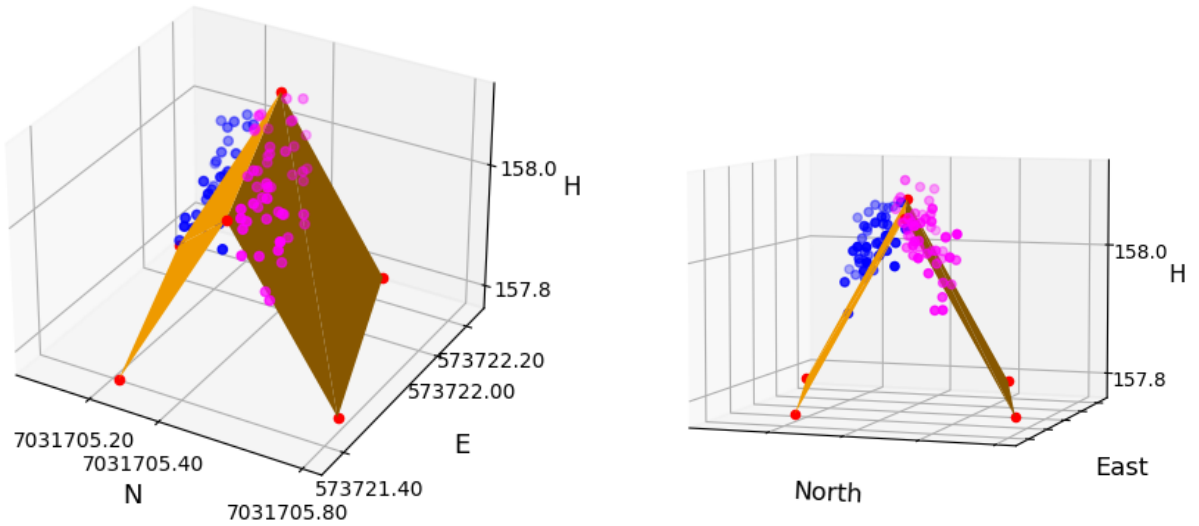

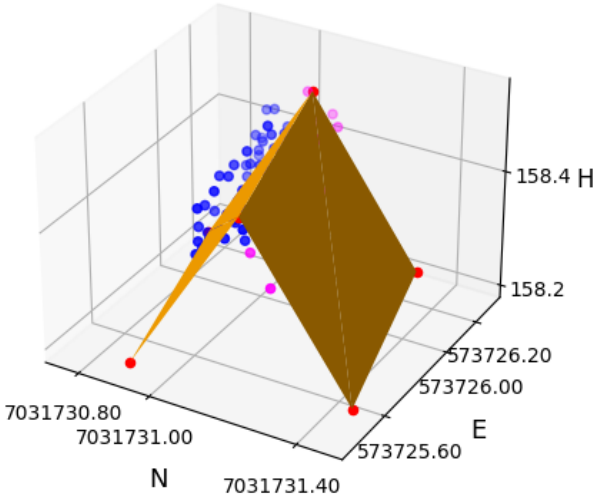
158.4
H
158.2
573726.20
573726.00
E
573725.60
7031730.80
7031731.00
N
7031731.40

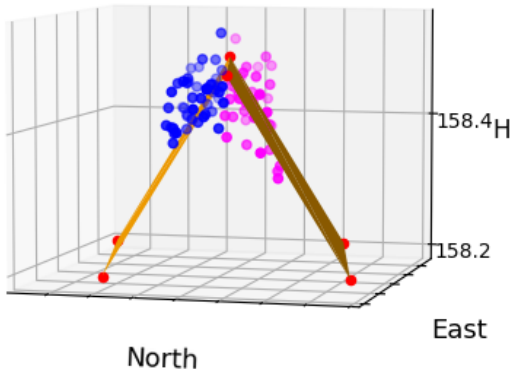
158.4
H
158.2
East
North

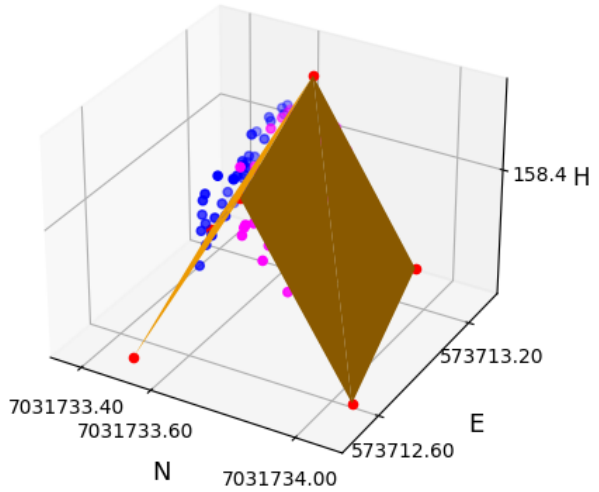
158.4
H
573713.20
E
573712.60
7031733.40
7031733.60
N
7031734.00

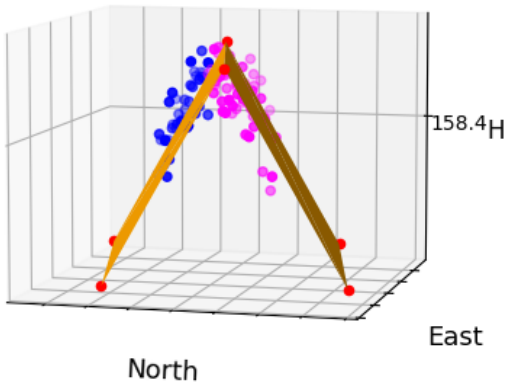
158.4
H
East
North

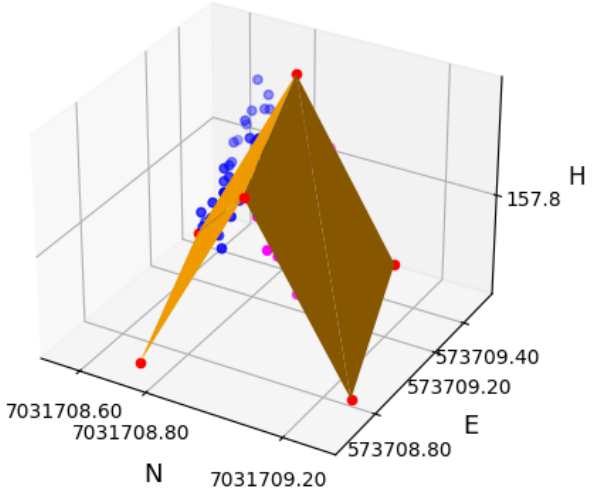
H
157.8
573709.40
573709.20
E
573708.80
7031708.60
7031708.80
N
7031709.20

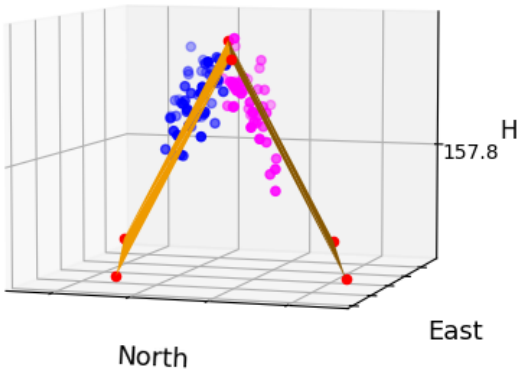
H
157.8
East
North

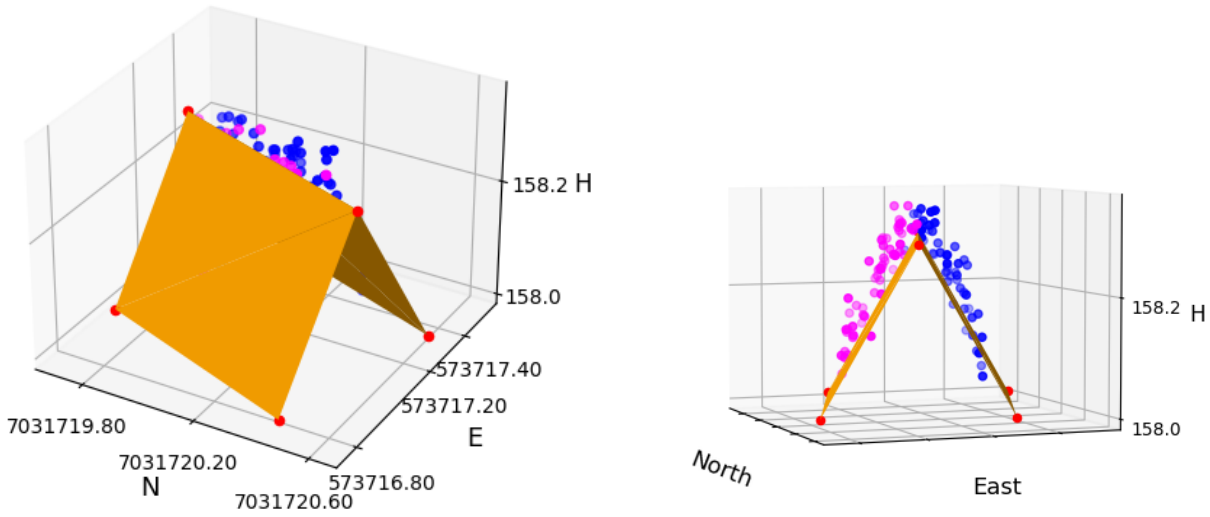

Figure C.3: Extracted point cloud from LCPs in the ascending order in S3 from two different angles divided in blue and magenta colour for each side of the true plane. The red points are the true points on the true plane

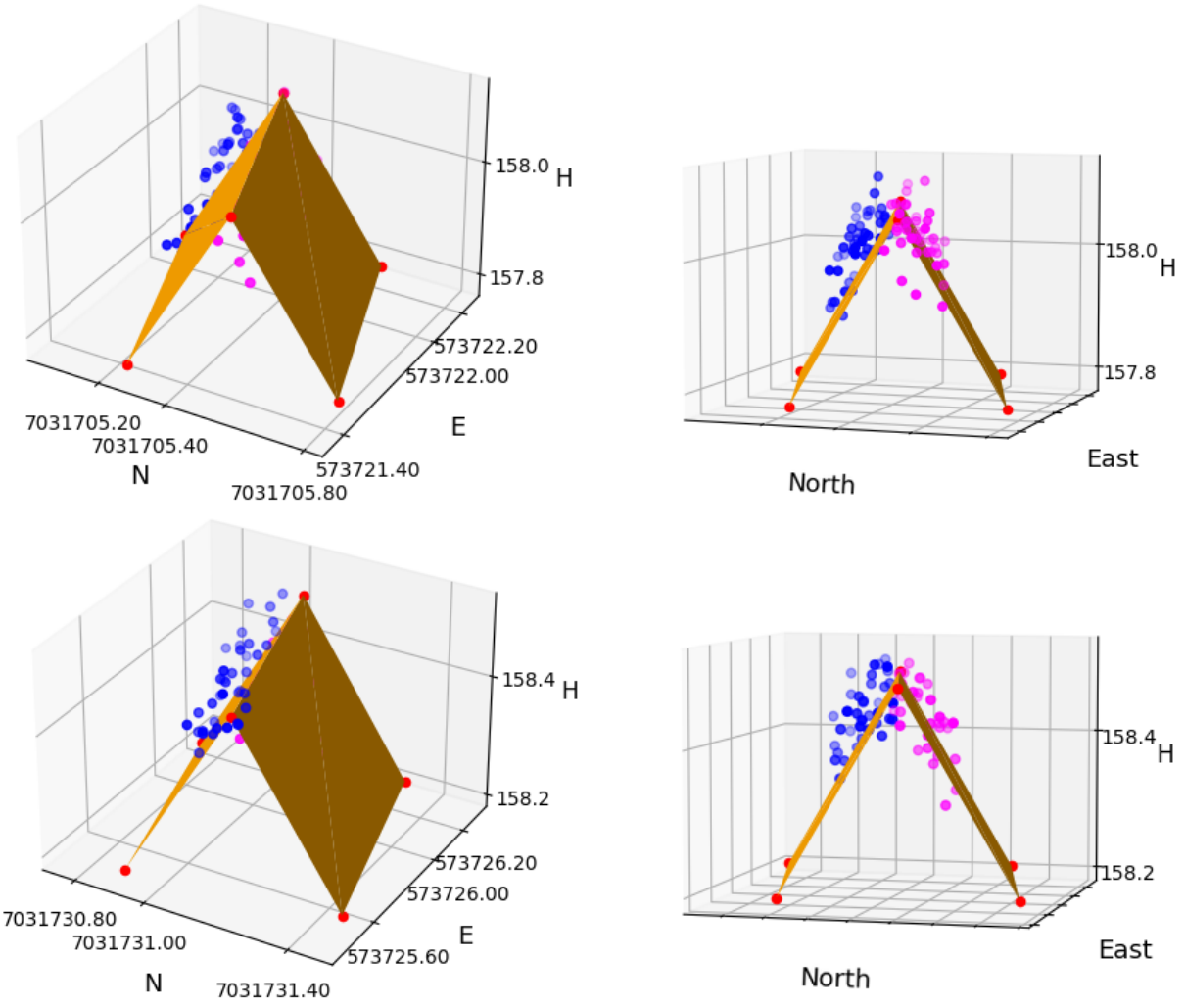

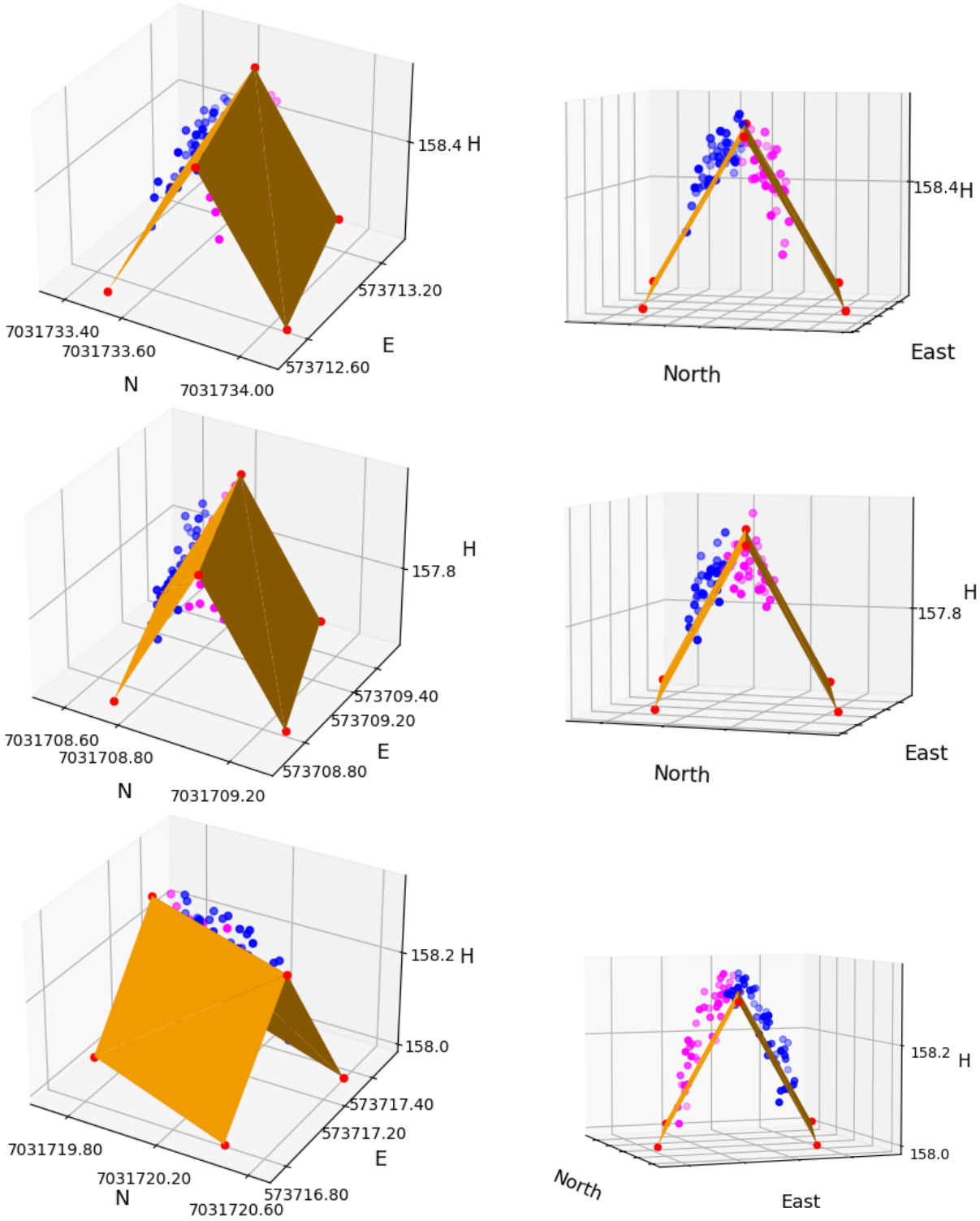

Figure C.4: Extracted point cloud from LCPs in the ascending order in S8 from two different angles divided in blue and magenta colour for each side of the true plane. The red points are the true points on the true plane

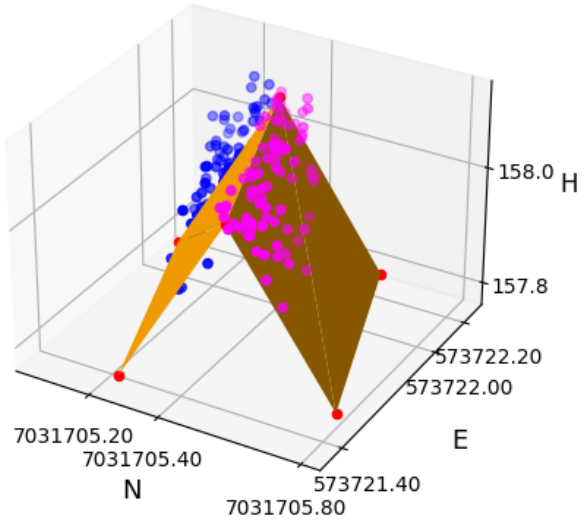
158.0
H
157.8
573722.20
573722.00
E
573721.40
7031705.20
7031705.40
N
7031705.80

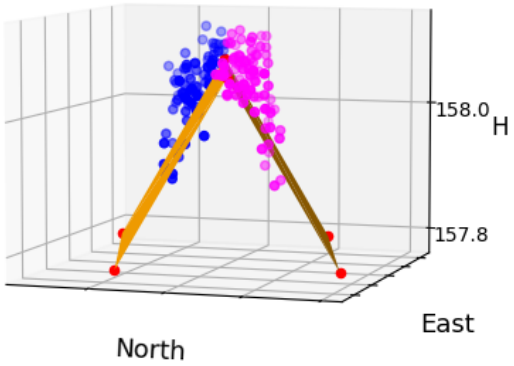
158.0
H
157.8
East
North

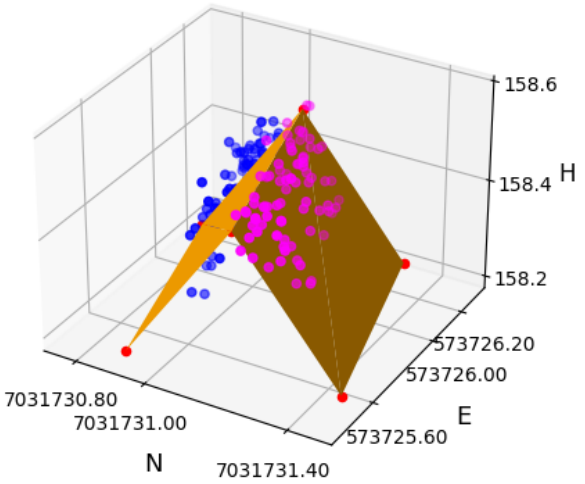
158.6
158.4
H
158.2
573726.20
573726.00
E
573725.60
7031730.80
7031731.00
N
7031731.40

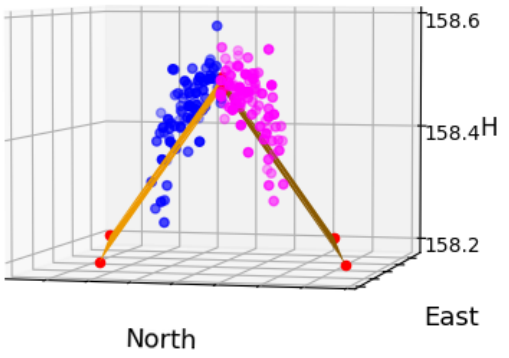
158.6
158.4
H
158.2
East
North

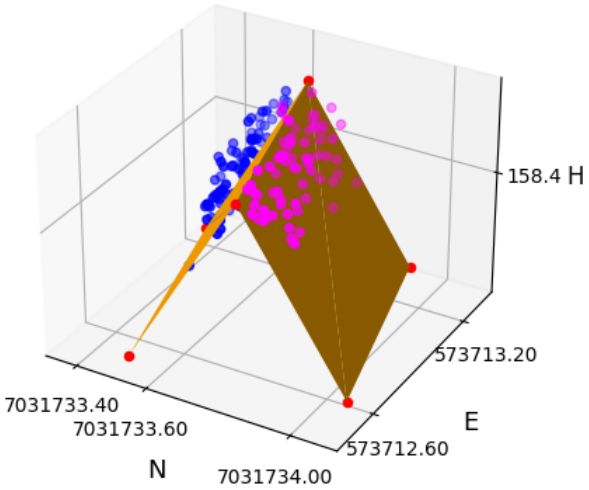
158.4
H
573713.20
E
573712.60
7031733.40
7031733.60
N
7031734.00

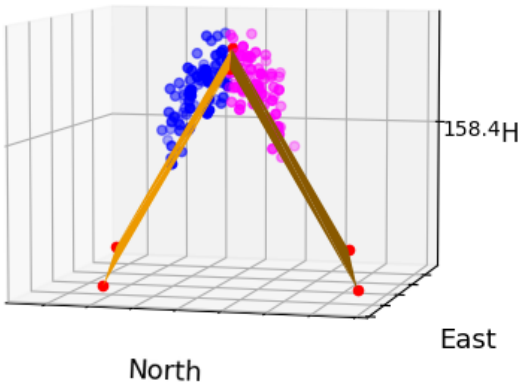
158.4
H
East
North

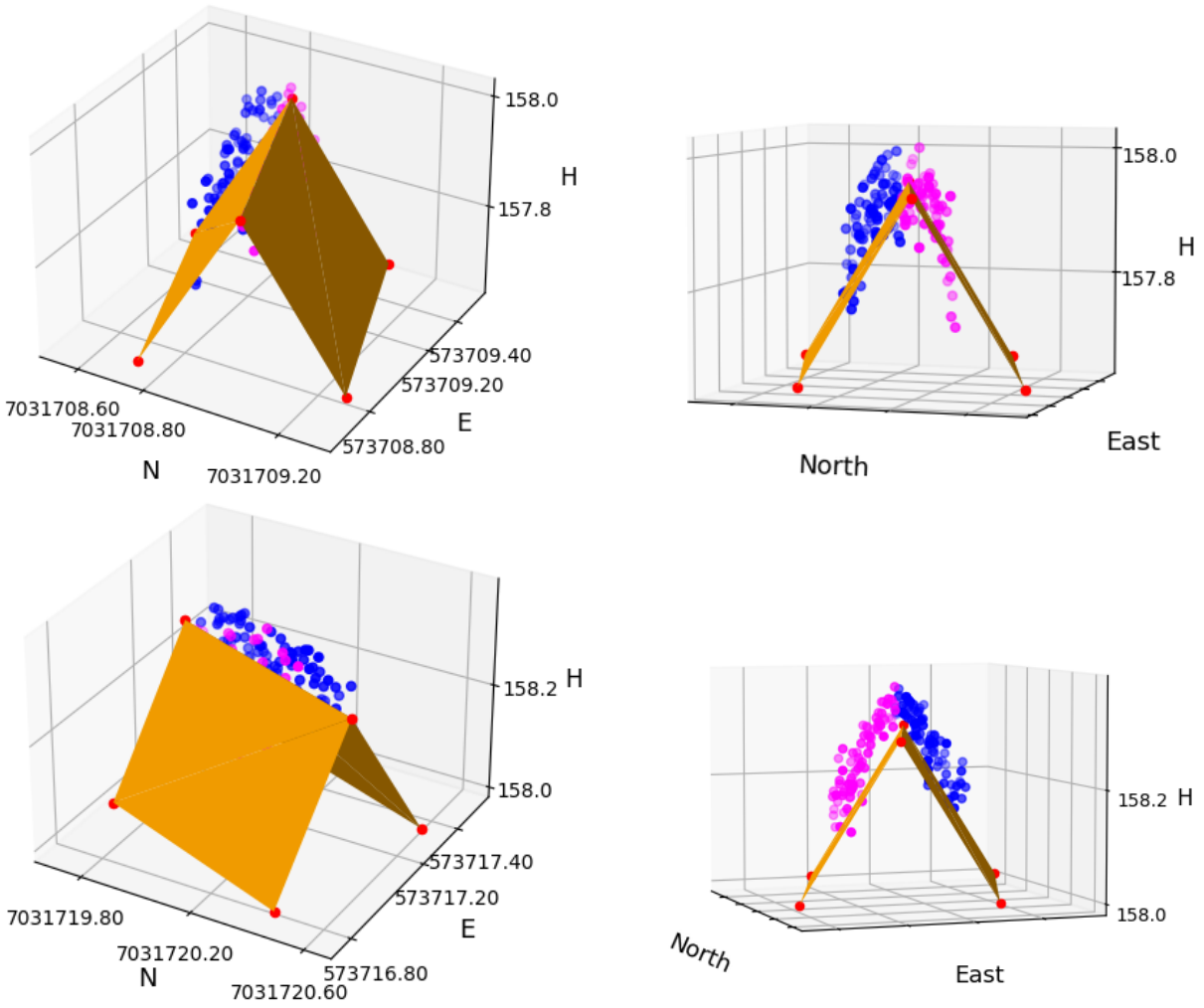

Figure C.5: Extracted point cloud from LCPs in the ascending order in S9 from two different angles divided in blue and magenta colour for each side of the true plane. The red points are the true points on the true plane.

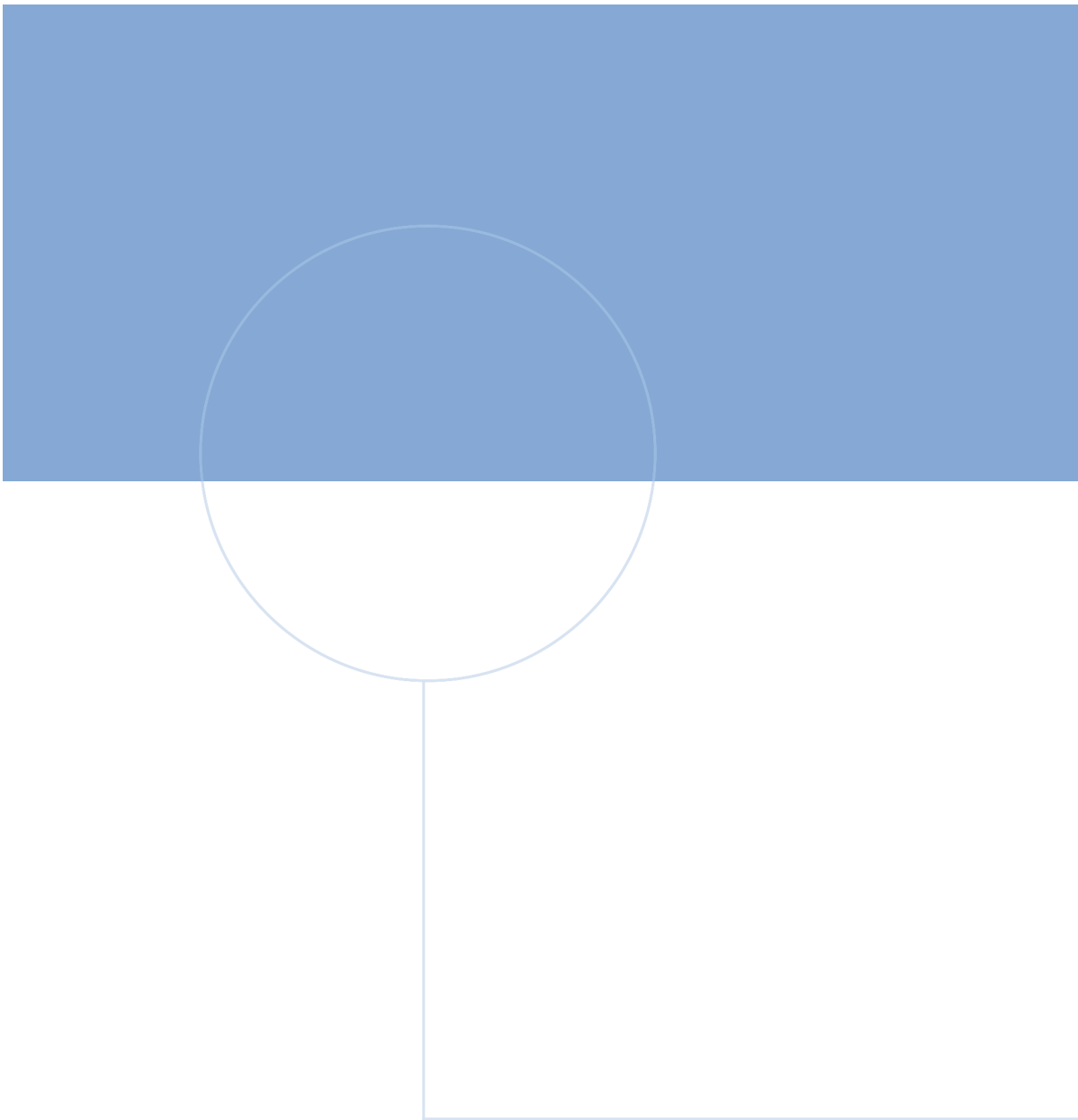

NTNU

Norwegian University of
Science and Technology